

AD-A047 980

AERONAUTICAL RESEARCH ASSOCIATES OF PRINCETON INC N J F/G 4/1
1977 STATUS REPORT ON LOW-LEVEL, ATMOSPHERIC TURBULENCE MODEL F--ETC(U)
NOV 77 W S LEWELLEN, D A OLIVER, M E TESKE N00019-77-C-0131
ARAP-320 NL

UNCLASSIFIED

2
OF
AD
A047980



2

80

AD A047980

Del 14/11/70

APPROVED FOR PUBLIC
DISTRIBUTION UNLIMITED

A. R. A.

CONSULTANTS TO INDUSTRY IN ADVANCE

AD No. _____
DDC FILE COPY

1977 STATUS REPORT ON
LOW-LEVEL, ATMOSPHERIC TURBULENCE
MODEL FOR MARINE ENVIRONMENTS

FINAL REPORT
(15 Nov 1976 - 15 Nov 1977)

NOVEMBER 1977

BY

W.S. LEWELLEN, D.A. OLIVER, M.E. TESKE,
H. SEGUR AND O. COTÉ

PREPARED UNDER CONTRACT N00019-77-C-0131

FOR

NAVAL AIR SYSTEMS COMMAND
DEPARTMENT OF THE NAVY
WASHINGTON, D.C. 20361

BY

AERONAUTICAL RESEARCH ASSOCIATES OF PRINCETON, INC.
50 WASHINGTON ROAD, P.O. Box 2229
PRINCETON, NEW JERSEY 08540

TABLE OF CONTENTS

	<u>Page</u>
1. INTRODUCTION	1
2. MODEL EXTENSIONS	3
2.1 Implementation of Atmospheric Radiation Transport in the Two-Dimensional Model	3
2.2 Two-Dimensional Computations with Terrain	4
2.3 Turbulent Transport of Aerosols	9
3. MODEL CALCULATIONS	20
3.1 Marine Boundary Layer Calculations	20
3.2 Gust Front Formed by Evaporative Cooling	22
4. CONCLUSIONS AND RECOMMENDATIONS	52
REFERENCES	54
APPENDIX A: "The Interaction Between Turbulent and Radiative Transport in the Development of Fog and Low-Level Stratus"	
APPENDIX B: "Comparison of the A.R.A.P. Second- Order Closure Model with Measurements in a Marine Boundary Layer"	
APPENDIX C: "Analysis of a Front Moving in the Planetary Boundary Layer"	

ACCESSION for	
NTIS	White Section <input checked="" type="checkbox"/>
DDC	Blue Section <input type="checkbox"/>
UNANNOUNCED	<input type="checkbox"/>
JUSTIFICATION	
BY	
DISTRIBUTION/AVAILABILITY CODES	
Dist	SPECIAL
A	

1. INTRODUCTION

Aeronautical Research Associates of Princeton, Inc. (A.R.A.P.) has been developing a program for computing the detailed low-level atmospheric distributions of velocity, temperature, moisture, refractive index, and the turbulent variances of these quantities for marine environments. Our approach to this problem has been to use the invariant second-order closure model of turbulence developed by Dr. Coleman duP. Donaldson and his associates at A.R.A.P. over the past few years. The fundamentals of this approach are given by Donaldson (1973). A review of the status of this model as applied to a wide variety of turbulent flow problems is given by Lewellen (1977). Particular applications of the model as applied to atmospheric problems, including comparisons with experimental data, are documented in Refs. 2-6.

Reference 7 is a technical report detailing the model development, sample calculations, and verification comparisons made under our initial NASC contract. It describes the addition of humidity and the second-order turbulent correlations involving humidity as variables to our dry atmospheric boundary layer program previously developed for the Environmental Protection Agency. Using the predicted distributions of temperature, humidity, and pressure, a calculation of the modified refractive index, M , has been incorporated in the program. Local minimums in the M distribution with respect to altitude directly indicate the presence of a radar duct. Since we are predicting the second-order correlations between the turbulent fluctuations in temperature and humidity as well as the average scale of the turbulence, we have available the information to also compute the structure of the fluctuations in refractivity.

The second year of the research called for two major modifications to the model described in Ref. 7. These were to (a) increase the dimensions of the program to a two-dimensional, unsteady calculation to permit the prediction of shoreline conditions developing in time, and (b) to incorporate the radiative flux divergence term into the one-dimensional system of equations in a coupled manner. These developments are detailed in Ref. 8.

The two-dimensional, unsteady version of the model has been used to calculate the typical variation in the coastal planetary boundary layer (Ref. 9). The resulting diurnal variation in the sea breeze induced by the strong stability differences in the boundary layer response over the land and that over the water produces a strong asymmetry between the sea-breeze and the land-breeze circulation patterns. In previous sea-breeze models, it was necessary to impose eddy viscosities which were a strong function of time and space to gain this asymmetry. In the present model, it is achieved without the need to introduce any new empirical information.

The last year's effort has been divided between exercising the model for verification purposes, and extending its capability.

Extensions to the model's capability include: (1) the removal of the hydrostatic approximation; (2) the incorporation of condensation and radiation into the two-dimensional, unsteady model; (3) the incorporation of terrain variation into the surface boundary conditions; and (4) the ability to determine the influence of particle size on the turbulent transport of aerosols. These developments are discussed in Chapter 2. Some of the sample calculations are detailed in Appendix A, a paper of our modeling results which has been accepted for publication in the Journal of the Atmospheric Sciences. These sample calculations demonstrated the strong dynamic interaction between turbulent transport and thermal radiation. Other sample calculations are discussed in Chapter 3 and Appendix B.

We have also investigated, analytically, some of the relationships between parameters governing distinct fronts in the planetary boundary layer, as an aid toward the detailed computation of the structure of such fronts. This analysis is discussed in Appendix C.

2. MODEL EXTENSIONS

Several important modifications to the model have been made during the last year. We began with the removal of the hydrostatic approximation from the two-dimensional program. This was accomplished by eliminating the pressure as a primary variable and formulating the equations in terms of streamfunction and vorticity. The numerical implementation of this modification is not described in the present report, but the results of a computation where the influence of nonhydrostatics is important is described in Section 3.2. The same two-dimensional calculation includes the effect of condensation and evaporation. This involved a straightforward carry-over of the same change of phase model as described in Appendix A. and applied to the one-dimensional code. Another modification to the numerics not described in detail herein was to provide a stronger coupling between the turbulent correlations. This permitted the simulated time step in our one-dimensional code to be increased by as much as a factor of 5. Model extensions which have been formulated but are not represented in any of the sample calculations are discussed in the following sections.

2.1 Implementation of Atmospheric Radiation Transport in the Two-Dimensional Model

The A.R.A.P. atmospheric radiation model described in Lewellen, et al., 1976 has been implemented with the two-dimensional turbulence models for the situations where vertical radiative transport is dominant. This includes most atmospheric boundary layer motions including those with clouds consisting of stratus decks, closely packed cumulus and fog layers. Typically we require (1) that cloud-cloud horizontal radiative transport be negligible compared to vertical radiative transport or horizontal advective and turbulent transport, and (2) that radiation from the sides of cumulus cells to the ground or to space be negligible compared to vertical radiative transport in the cumulus. If we denote the average depth of a cloud as δ and its characteristic breadth as L , then a condition for vertical dominance of radiative transport may be formulated by requiring that radiative cooling to space through the cloud top be much greater than that through the sides. In terms of the fractional cloudiness R , this condition is

$$\frac{(\delta/L) \frac{1}{2} \left(\frac{1}{\sqrt{R}} - 1 \right)}{(\delta/L)^2 + \frac{1}{4} \left(\frac{1}{\sqrt{R}} - 1 \right)^2} \ll 1 \quad (2.1)$$

When the clouds are widely spaced ($R \ll 1$) this condition just requires that the "isolated" cloud have a small aspect ratio

$$\delta/L \ll 1 \quad (2.2)$$

On the other hand, as the sky is more filled with clouds ($R \rightarrow 1$) the aspect ratio condition is relaxed due to the blocking of radiation to space by adjacent clouds.

Within this approximation the vertical radiation field at a local horizontal position is determined by the distribution of fluid properties in the vertical at that horizontal position. The horizontal variation of the radiation field thus is a function of the horizontal variation of fluid absorption, scattering and emission properties.

It is interesting to note that the condition (2.1) is essentially a requirement that radiative loss (or gain) in the horizontal direction be small compared to the vertical. As such it is also the appropriate condition for validity of the vertically structured direct solar radiation scattering and absorption model in which only vertical back-scattering of incident solar energy by water droplets and aerosols is included. The required condition for validity of the vertical radiation model in a two-dimensional calculation is then that scattering of solar radiation off the sides of clouds be negligible compared to cloud top scattering.

2.2 Two-Dimensional Computations with Terrain

We now describe the procedures for the treatment of non-uniform terrain in the A.R.A.P. two-dimensional atmospheric boundary layer calculations. We consider a rectangular y-z domain as shown in Fig. 2.1 in which a rectangular grid of $m \times n$ points exists. A nonuniform terrain boundary ∂T cuts through this grid which we shall, for simplicity, assume passes through existing grid points as shown in Fig. 2.1. (The extension to terrain which does not fall exactly on the existing grid points is straightforward and will not be discussed here.) We let $z = z_m$ be the coordinate of the terrain and we let z_0 be the roughness height measured from z_m . Let N be the total number of interior points of the domain which lie on the terrain boundary ∂T .

The fundamental mean variables in two-dimensional calculations consist of the vorticity η , potential temperature θ_v , and the streamfunction ψ describing the mean velocity field.^v These variables are supplemented with the turbulent correlations and their corresponding equations. The streamfunction and vorticity are defined on the full rectangular grid but all other variables are defined on only the grid points where fluid exists outside the terrain and on the boundary. Our purpose in defining the streamfunction ψ and vorticity η on the full grid stems from the need to rapidly solve the streamfunction equation

$$\Delta^2 \psi = -\eta \quad (2.3)$$

at each time step. For this purpose, we utilize a rapid direct cyclic reduction algorithm which requires a uniform boundary domain. Thus, we solve Eq. (2.3) on the full rectangle including the region lying "inside" the terrain. This procedure will not invalidate our solution for the flow outside the terrain because data inside the terrain will not be utilized and the solution will be constructed such that the correct terrain surface

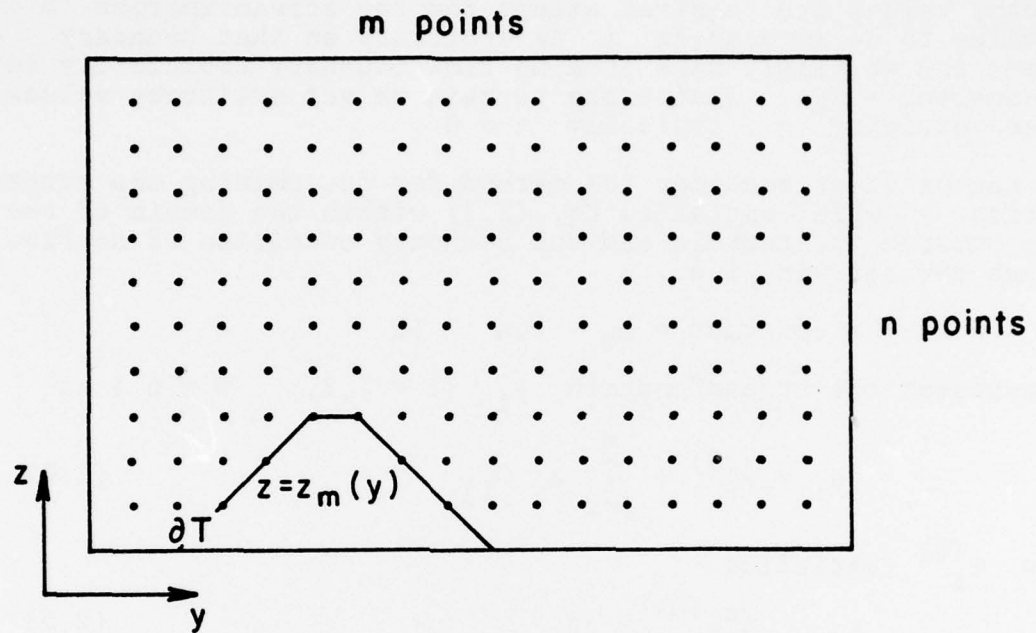


Figure 2.1 Nonrectangular computational domain.

conditions on ψ in particular and all other variables in general will be impressed on the embedded terrain points by the method we now describe (Roache, 1972).

The boundary conditions on the rectangle are specified in the usual fashion for all variables except on that portion of the rectangle lying within the terrain. On that portion, no boundary values are required except for the streamfunction ψ . The value to be imposed on ψ is arbitrary on that boundary segment and we simply make it a no-flow boundary arbitrarily setting $\psi = \text{constant} = \psi_k$. Inside the terrain we set arbitrary values of the vorticity η , typically $\eta = 0$.

Let us first consider the method for determining the streamfunction ψ which satisfies Eq. (2.3) within the domain of the fluid outside the terrain and the boundary condition of no-flow through the terrain, i.e.,

$$\psi = \text{constant} = \psi_T \quad \text{on} \quad \partial T$$

We represent the streamfunction ψ_i ($i = 1, 2, \dots, m \times n$) as

$$\psi_i = \psi_i^{(0)} + \sum_{j=1}^N a_j G_{ij} \quad (2.4)$$

where $\psi_i^{(0)}$ satisfies

$$\Delta^2 \psi_i^{(0)} = -\eta_i \quad (2.5)$$

a_j is an N length column vector, and G_{ij} ($i = 1, 2, \dots, m \times n$; $j = 1, 2, \dots, N$) is an $(m \times n) \times N$ matrix which satisfies

$$\Delta^2 G_{ij} = \delta_{ij} \quad (2.6)$$

where δ_{ij} is the Kronecker delta and the index j ranges over all the points $j = 1, 2, \dots, N$ which lie on the terrain boundary. The matrix function G_{ij} is a discrete Green's function for the boundary and Δ^2 is a discrete difference operator approximating the Laplacian operator.

Equations (2.5) and (2.6) are solved on the full rectangular grid with boundary conditions on $\psi^{(0)}$ given by those required by the physics of the problem outside the terrain and by $\psi_i^{(0)} = \psi_R$ on the portion of the rectangle lying inside the terrain. The Green's functions G_{ij} satisfy either $G_{ij} = 0$ or $\partial G_{ij} / \partial n = 0$ on the rectangular boundary, depending upon whether ψ takes a Dirichlet or Neumann condition. $N + 1$ executions are required for the cyclic reduction algorithm; One for $\psi_i^{(0)}$ and N for the G_{ij} .

The constants a_j are determined by requiring that ψ_i take on the specified value ψ_T on ∂T . Thus on the N points lying on ∂T we require

$$\psi_i = \psi_i^{(0)} + \sum_{j=1}^N a_j \tilde{G}_{ij} = \psi_T \quad (2.7)$$

$i = 1, 2, \dots, N$

where \tilde{G}_{ij} is a portion of matrix G_{ij} only containing contributions from G_{ij} for i corresponding to points lying on ∂T . The matrix \tilde{G}_{ij} is thus an $N \times N$ matrix. The constants a_j are determined as

$$a_j = - \sum_{i=1}^N \tilde{G}_{ji}^{-1} (\psi_i^{(0)} - \psi_T) \quad (2.8)$$

We note that the matrices G_{ij} , \tilde{G}_{ij} , and \tilde{G}_{ji}^{-1} may be computed once for all time since they depend only upon the geometry of the domain (including, of course, the terrain boundary).

After each time advance in which an updated η field is obtained, we solve Eq. (2.5) for $\psi_i^{(0)}$. We then determine the solution ψ_i satisfying the terrain boundary condition and the remaining boundary conditions on the rectangular region as

$$\psi_i = \psi_i^{(0)} - \sum_{j=1}^N \sum_{i=1}^N \tilde{G}_{ji}^{-1} (\psi_i^{(0)} - \psi_T) G_{ij} \quad (2.9)$$

utilizing the known and stored values of \tilde{G}_{ji}^{-1} and G_{ij} .

The vorticity, temperature and turbulence variables are solved only in the region outside the terrain utilizing an alternating-direction-implicit technique which does not require uniform boundaries. Boundary conditions on the rectangular portion are conventional, but boundary conditions on the terrain boundary ∂T require special treatment. As on other no-slip boundaries, we do not integrate the equations all the way to the wall (which would require exceedingly fine and wasteful mesh spacing). Instead, we require that the variables take on their constant flux region values. For the vorticity this requirement results in a linear relationship between the boundary value of η and ψ on the first interior point. For the turbulent correlations, the requirements is that their normal gradients vanish.

Preliminary results demonstrate the feasibility of the Green's function approach to give the correct streamfunctions throughout the computational domain. The procedure yields a fairly realistic contour pattern for the streamfunction at flow separation over a two-dimensional mountain, as shown in Fig. 2.2. Here the flow is entering from the left, separating down the slope, and reattaching further downstream. An added divergence of the flow at the top

STREAMFUNCTION

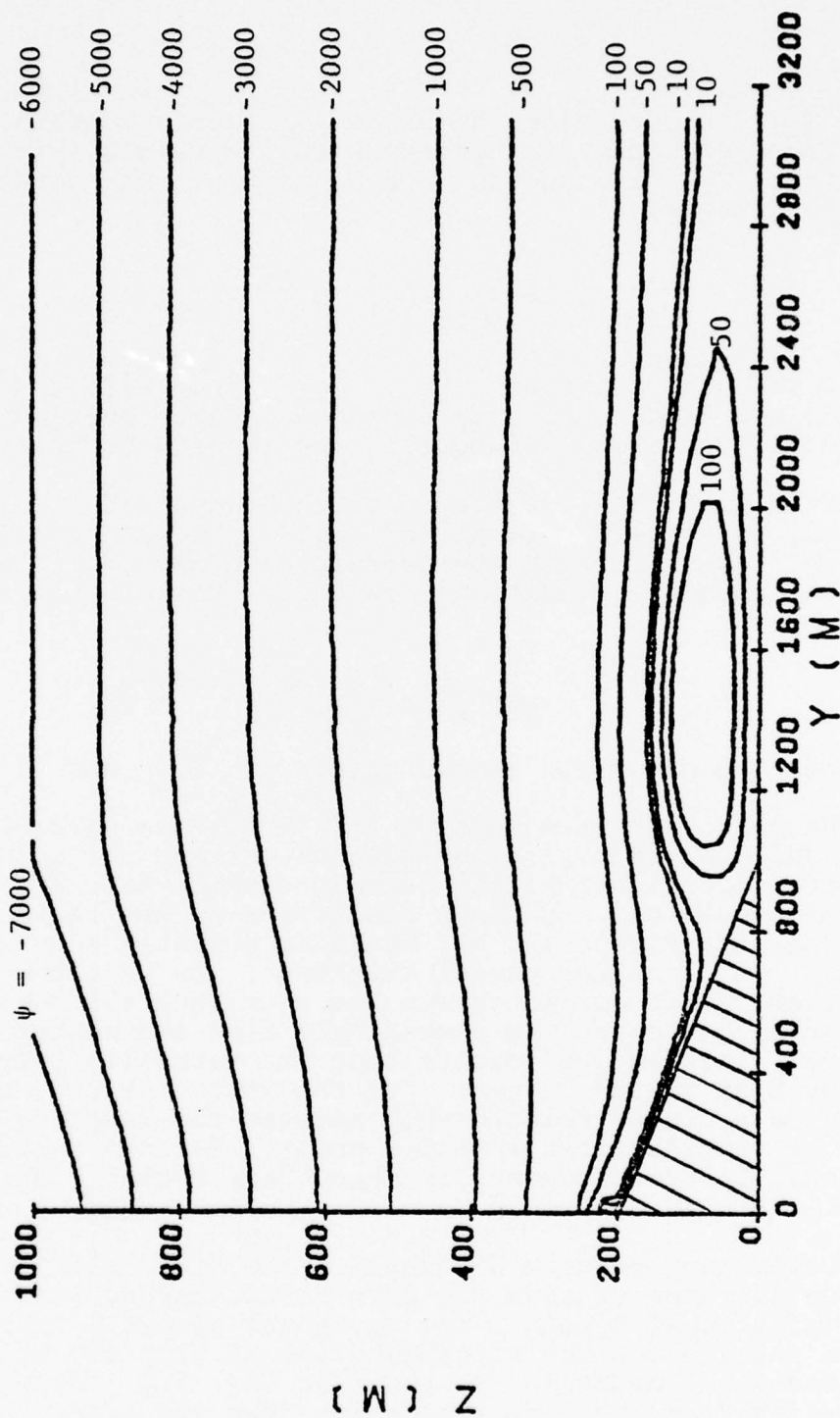


Figure 2.2 Streamfunction contours on the leeward side of a two-dimensional barrier.

of the calculation domain enhances separation. The separation point along the slope is fairly well held, but the bubble itself seems to push the reattachment point slowly downstream. Some questions must still be answered with regard to the best way to apply the vorticity and turbulence boundary conditions along the interior boundary.

2.3 Turbulent Transport of Aerosols

In previous reports (Donaldson, 1973, Lewellen and Teske, 1975) second-order closure has been applied to gaseous diffusion. The purpose here is to apply the same technique to the diffusion of finite size aerosol particles, in order to determine what conditions influence their turbulent diffusion and how the diffusion of such particles may be computed.

Following Marble (1970) the equations of motion for an incompressible flow containing a cloud of particles of concentration c may be written as

$$\frac{\partial u_i}{\partial x_i} = 0 \quad (2.10)$$

$$\frac{\partial c}{\partial t} + \frac{\partial cu_{Ai}}{\partial x_i} = S \quad (2.11)$$

$$\begin{aligned} \frac{\partial u_i}{\partial t} + \frac{\partial u_i u_j}{\partial x_j} &= \frac{1}{\rho} \frac{\partial}{\partial x_j} (-p \delta_{ij}) + \frac{1}{\rho} \frac{\partial}{\partial x_j} \mu \frac{\partial u_i}{\partial x_j} \\ &\quad + c \frac{(u_{Ai} - u_i)}{\tau_v} + F_i \\ \frac{\partial cu_{Ai}}{\partial t} + \frac{\partial (cu_{Ai} u_{Aj})}{\partial x_j} &= -c \frac{(u_{Ai} - u_i)}{\tau_v} + c F_i \end{aligned} \quad (2.13)$$

The characteristic time τ_v is the time required by a particle to reduce its velocity relative to the gas by e^{-1} of its original state, in the unaccelerated state. For a significant range of particle radii τ_v may be described by Stokes flow

$$\tau_v = \frac{2}{9} \rho_A \frac{\sigma^2}{\mu}$$

with ρ_A the density of the aerosol particle, and σ its radius.

We will follow the same procedure of Donaldson (1973) to obtain equations for the turbulent transport, $\overline{u_{Ai} c'}$, of the aerosol. When the variables are decomposed into an ensemble mean and a fluctuating contribution, i.e., $c = \bar{c} + c'$, $u_{Ai} = \bar{u}_{Ai} + u'_{Ai}$, etc., then Eqs. (2.10) to (2.13) may be averaged

to yield

$$\frac{\partial \bar{u}_i}{\partial x_i} = 0 \quad (2.14)$$

$$\frac{\partial \bar{c}}{\partial t} + \frac{\partial \bar{c} \bar{u}_{A_i}}{\partial x_i} = \bar{S} - \frac{\partial \overline{c' u'_{A_i}}}{\partial x_i} \quad (2.15)$$

$$\begin{aligned} \frac{\partial \bar{u}_i}{\partial t} + \frac{\partial \bar{u}_i \bar{u}_j}{\partial x_j} = & - \frac{1}{\rho} \frac{\partial}{\partial x_j} (\bar{p} \delta_{ij}) + \frac{\partial}{\partial x_j} \left(\nu \frac{\partial \bar{u}_i}{\partial x_j} \right) - \frac{\partial \overline{u'_i u'_j}}{\partial x_j} \\ & + \frac{\bar{c}(\bar{u}_{A_i} - \bar{u}_i)}{\tau_v} + \frac{1}{\tau_v} (\overline{c' u'_{A_i}} - \bar{c} \bar{u}'_i) + \bar{F}_i \end{aligned} \quad (2.16)$$

$$\begin{aligned} \frac{\partial \bar{c} \bar{u}_{A_i}}{\partial t} + \frac{\partial \overline{c' u'_{A_i}}}{\partial t} + \frac{\partial \bar{c} \bar{u}_{A_i} \bar{u}_{A_j}}{\partial x_j} = & - \frac{\partial}{\partial x_j} (\bar{c} \overline{u'_{A_i} u'_{A_j}} + \overline{c' u'_{A_i}} \bar{u}_{A_j} \\ & + \overline{c' u'_{A_j}} \bar{u}_{A_i} + \overline{c' u'_{A_i} u'_{A_j}}) - \frac{c}{\tau_v} (\bar{u}_{A_i} - \bar{u}_i) \\ & - \frac{1}{\tau_v} (\overline{c' u'_{A_i}} - \bar{c} \bar{u}'_i) + \bar{c} \bar{F}_i \end{aligned} \quad (2.17)$$

It is also possible to eliminate c from the particle momentum equation by subtracting \bar{u}_{A_i} times Eq. (2.11) from Eq. (2.13)

$$\frac{\partial u_{A_i}}{\partial t} + u_{A_j} \frac{\partial u_{A_i}}{\partial x_j} = - \frac{(u_{A_i} - \bar{u}_i)}{\tau_v} - S u_{A_i} + F_i \quad (2.18)$$

This momentum equation may be averaged to obtain

$$\begin{aligned} \frac{\partial \bar{u}_{A_i}}{\partial t} + \bar{u}_{A_j} \frac{\partial \bar{u}_{A_i}}{\partial x_j} = & - \frac{(\bar{u}_{A_i} - \bar{u}_i)}{\tau_v} - \bar{S} \bar{u}_{A_i} - \overline{S' u'_{A_i}} \\ & - \bar{u}'_{A_j} \frac{\partial \bar{u}'_{A_i}}{\partial x_j} + \bar{F}_i \end{aligned} \quad (2.19)$$

Now, by multiplying Eq. (2.15) by \bar{u}_{A_i} and Eq. (2.19) by \bar{c} and subtracting these two products from Eq. (2.17) the following equation for $\overline{c' u'_{A_i}}$ may be obtained.

$$\begin{aligned}
\frac{\partial \overline{c'u_{A_i}}}{\partial \tau} + \frac{\partial \bar{u}_{A_j} \overline{c'u_{A_j}}}{\partial x_j} &= - \overline{u_{A_i} u_{A_j}} \frac{\partial \bar{c}}{\partial x_j} - \bar{c} u'_{A_j} \frac{\partial \bar{u}_{A_i}}{\partial x_j} \\
&- \overline{c'u_{A_j}} \frac{\partial \bar{u}_{A_i}}{\partial x_j} - \frac{\partial \overline{c'u_{A_i} u_{A_j}}}{\partial x_j} - \frac{(\overline{c'u_{A_i}} - \overline{c'u_i})}{\tau_v} \\
&+ \overline{S'u_{A_i}} \bar{c}
\end{aligned} \tag{2.20}$$

An equation for the correlation $\overline{u_{A_i} u_{A_j}}$ appearing in Eq. (2.20) may be obtained by manipulating the equation for u'_{A_i} derived by subtracting Eq. (2.19) from Eq. (2.18).

$$\begin{aligned}
\frac{\partial \overline{u'_{A_i} u_{A_j}}}{\partial \tau} + \bar{u}_{A_k} \frac{\partial \overline{u'_{A_i} u_{A_j}}}{\partial x_k} &= - \overline{u'_{A_j} u_{A_k}} \frac{\partial \bar{u}_{A_i}}{\partial x_k} - \overline{u'_{A_i} u_{A_k}} \frac{\partial \bar{u}_{A_j}}{\partial x_k} \\
&- \frac{\partial \overline{u'_{A_i} u'_{A_j} u_{A_k}}}{\partial x_k} + \overline{u'_{A_i} u'_{A_j}} \frac{\partial \bar{u}_{A_k}}{\partial x_k} - \frac{1}{\tau_v} (2\overline{u'_{A_i} u_{A_j}} - \overline{u'_{A_i} u_j} \\
&- \overline{u'_{A_j} u_i}) - \overline{S'u_{A_j}} \bar{u}_{A_i} - 2\overline{S'u_{A_i} u_{A_j}} - 2\overline{S'u_{A_i} u_{A_j}} \\
&- \overline{S'u_{A_j}} \bar{u}_{A_j}
\end{aligned} \tag{2.21}$$

An equation for the cross correlation $\overline{u'_{A_i} u_j}$ may be obtained from Eqs. (2.12), (2.16), (2.18) and (2.19) to be

$$\begin{aligned}
\frac{\partial \overline{u'_{A_i} u_j}}{\partial \tau} + \bar{u}_k \frac{\partial \overline{u'_{A_i} u_j}}{\partial x_k} &= - (\bar{u}_{A_k} - \bar{u}_k) u'_j \frac{\partial \bar{u}_{A_i}}{\partial x_k} - \overline{u'_{A_i} u'_k} \frac{\partial \bar{u}_j}{\partial x_k} \\
&- \overline{u'_{A_j} u_{A_k}} \frac{\partial \bar{u}_{A_i}}{\partial x_k} - \frac{\partial \overline{u'_{A_i} u'_j u'_k}}{\partial x_k} - (\overline{u'_{A_k}} - \overline{u'_k}) u'_j \frac{\partial \bar{u}_{A_i}}{\partial x_k} \\
&- \overline{u'_{A_i}} \frac{\partial \bar{p}}{\partial x_j} + \frac{1}{\tau_v} \left[\overline{u'_{A_i} c'} (\bar{u}_{A_j} - \bar{u}_j) + \bar{c} (\overline{u'_{A_i} u_{A_j}} - \overline{u'_{A_i} u_j}) \right. \\
&+ \left. \overline{c' (u'_{A_i} u_{A_j} - u'_{A_i} u_j)} + \overline{u'_i u'_j} - \overline{u'_j u_{A_j}} \right] \\
&+ v \text{ terms}
\end{aligned} \tag{2.22}$$

An equation for $\overline{c'u_i}$ can also be generated from Eqs. (2.11), (2.15), (2.12) and (2.19) to be

$$\begin{aligned} \frac{\partial \overline{c'u_i}}{\partial \tau} + \bar{u}_j \frac{\partial \overline{c'u_i}}{\partial x_j} = & -(\bar{u}_{A_j} - \bar{u}_j) \overline{u'_i \frac{\partial c'}{\partial x_j}} - \overline{u'_i u'_{A_j}} \frac{\partial \bar{c}}{\partial x_j} \\ & - \overline{c'u'_j} \frac{\partial \bar{u}_i}{\partial x_j} - \frac{\partial \overline{c'u'_i u'_j}}{\partial x_j} - (\overline{u'_{A_j}} - \overline{u'_j}) \overline{u'_i \frac{\partial c'}{\partial x_j}} + \overline{S'u'_i} \\ & - \overline{c' \frac{\partial p'}{\partial x_i}} + \frac{\bar{c}}{\tau_v} (\bar{u}_{A_i} - \bar{u}_i) + \frac{\bar{c}}{\tau_v} (\overline{c'u'_{A_i}} - \overline{c'u'_i}) \\ & + \frac{1}{\tau_v} (\overline{c'^2 u'_{A_i}} - \overline{c'^2 u'_i}) + v \text{ terms} \end{aligned} \quad (2.23)$$

The extent of the new modeling required to close the system by carrying the full set of equations for $\overline{c'u_{A_i}}$, $\overline{c'u'_i}$, $\overline{u'_{A_i} u'_{A_j}}$, $\overline{u'_{A_i} u'_j}$, along with $\overline{u'_i u'_j}$ may be assessed from Eqs. (2.20) through (2.23). The list is quite extensive:

$$\begin{aligned} & \overline{u'_{A_i} \frac{\partial u'_{A_j}}{\partial x_j}}, \overline{c'u'_{A_i} u'_{A_j}}, \overline{c'u'_i u'_j}, \overline{u'_{A_i} u'_{A_j} u'_{A_k}}, \overline{c' \frac{\partial p'}{\partial x_i}}, \overline{c'^2 u'_{A_i}} \\ & \overline{u'_{A_i} u'_{A_j} \frac{\partial u'_{A_k}}{\partial x_k}}, \overline{(u'_{A_j} - u'_j) u'_i \frac{\partial c'}{\partial x_j}}, \overline{u'_j \frac{\partial u'_{A_i}}{\partial x_k}}, \overline{u'_{A_i} u'_j u'_k}, \overline{c'^2 u'_i} \\ & \overline{(u'_{A_i} - u'_i) u'_j \frac{\partial u'_{A_i}}{\partial x_k}}, \overline{u'_{A_i} \frac{\partial p'}{\partial x_i}}, \overline{c'u'_{A_i} u'_j}, \overline{u'_i \frac{\partial c'}{\partial x_j}} \end{aligned}$$

along with the terms involving S' and v . Rather than undertake this modeling task, we will take advantage of the fact that τ_v associated with most aerosols of interest is much shorter than the characteristic time of the atmospheric turbulence, Λ/q . We will assume that u_{A_i} may be expanded as

$$u_{A_i} = u_i + \frac{\tau_v q}{\Lambda} (u_{1_i}) + O(\tau_v q / \Lambda)^2 \quad (2.24)$$

If this expansion is carried through Eqs. (2.20) through (2.23), the leading order terms reduce to

$$\begin{aligned}
\frac{\partial \overline{c'u_i}}{\partial t} + \frac{\partial (\bar{u}_{A_j} \overline{c'u_i})}{\partial x_j} &= -\overline{u_i u_j} \frac{\partial \bar{c}}{\partial x_j} - \overline{c'u_j} \frac{\partial \bar{u}_i}{\partial x_j} - \frac{\partial \overline{c'u_i u_j}}{\partial x_j} \\
&- \frac{1}{\tau_v} (\overline{c'u_{A_i}} - \overline{c'u_i})
\end{aligned} \tag{2.25}$$

$$\begin{aligned}
\frac{\partial \overline{u_i u_j}}{\partial t} + \bar{u}_{A_k} \frac{\partial \overline{u_i u_j}}{\partial x_k} &= -\overline{u_j u_k} \frac{\partial \bar{u}_{A_i}}{\partial x_k} - \overline{u_i u_k} \frac{\partial \bar{u}_{A_j}}{\partial x_k} - \frac{\partial \overline{u_i u_j u_k}}{\partial x_k} \\
&- \frac{1}{\tau_v} (2\overline{u_{A_i} u_{A_j}} - \overline{u_{A_i} u_j} - \overline{u_i u_{A_j}}) - \overline{S'u_j} \overline{u_{A_i}} \\
&- 2\overline{S'u_i u_j} - 2\bar{S} \overline{u_i u_j} - \overline{S'u_i} \overline{u_{A_j}}
\end{aligned} \tag{2.26}$$

$$\begin{aligned}
\frac{\partial \overline{u_i u_j}}{\partial t} + \bar{u}_k \frac{\partial \overline{u_i u_j}}{\partial x_k} &= -(\bar{u}_{A_k} - \bar{u}_k) \overline{u_j' \frac{\partial u_i}{\partial x_k}} - \overline{u_i u_k} \frac{\partial \bar{u}_j}{\partial x_k} \\
&- \overline{u_j u_k} \frac{\partial \bar{u}_{A_i}}{\partial x_k} - \frac{\partial \overline{u_i u_j u_k}}{\partial x_k} - \overline{u_{A_i}} \frac{\partial \bar{p}}{\partial x_j} + \frac{1}{\tau_v} [\overline{u_{A_i} c'} (\bar{u}_{A_j} - \bar{u}_j) \\
&+ \bar{c} (\overline{u_{A_i} u_{A_j}} - \overline{u_{A_i} u_j}) + \overline{c' (u_{A_i} u_{A_j} - u_{A_i} u_j)} + \overline{u_i u_j} \\
&- \overline{u_j u_{A_i}}] + v \text{ terms}
\end{aligned} \tag{2.27}$$

$$\begin{aligned}
\frac{\partial \overline{c'u_i}}{\partial t} + \bar{u}_j \frac{\partial \overline{c'u_i}}{\partial x_j} &= -(\bar{u}_{A_j} - \bar{u}_j) \overline{u_i' \frac{\partial c}{\partial x_j}} - \overline{u_i u_j} \frac{\partial \bar{c}}{\partial x_j} \\
&- \overline{c'u_j} \frac{\partial \bar{u}_i}{\partial x_j} - \frac{\partial \overline{c'u_i u_j}}{\partial x_j} + \overline{S'u_i} - \overline{c' \frac{\partial p}{\partial x_i}} + \frac{\overline{c'^2}}{\tau_v} (\bar{u}_{A_i} - \bar{u}_i) \\
&+ \frac{\bar{c}}{\tau_v} (\overline{c'u_{A_i}} - \overline{c'u_i}) + \frac{1}{\tau_v} (\overline{c'^2 u_{A_i}} - \overline{c'^2 u_i}) + v \text{ terms}
\end{aligned} \tag{2.28}$$

Equations (2.25) through (2.28) must also be consistent with the equation for $\overline{u_i u_j}$ computed from Eqs. (2.12) and (2.16).

$$\begin{aligned} \frac{\partial \overline{u_i u_j}}{\partial t} + \bar{u}_k \frac{\partial \overline{u_i u_j}}{\partial x_k} = & -\overline{u_i u_k} \frac{\partial \bar{u}_j}{\partial x_k} - \overline{u_j u_k} \frac{\partial \bar{u}_i}{\partial x_k} - \frac{\partial \overline{u_i u_j u_k}}{\partial x_k} \\ & - \overline{u_i' \frac{\partial p'}{\partial x_j}} + \frac{1}{\tau_v} \left[\overline{u_i' c'} (\bar{u}_{A_i} - \bar{u}_j) + \bar{c}' (\overline{u_{A_i}' u_{A_j}'} - 2\overline{u_i' u_j'}) \right. \\ & \left. + \overline{u_{A_i}' u_j'} + \overline{u_j' c'} (\bar{u}_{A_i} - \bar{u}_i) + \bar{c}' (\overline{u_i' u_{A_j}'} - 2\overline{u_i' u_j'} + \overline{u_{A_i}' u_j'}) \right] \\ & + v \text{ terms} \end{aligned} \quad (2.29)$$

First, let us consider the case where $c \ll 1$ and the fluid turbulence may be decoupled from the particle motion. In this limit the terms involving c and c' may be dropped from Eq. (2.29). Let us also assume $S = 0$, and note that $\bar{u}_{A_i} - \bar{u}_i = 0(\tau_v g)$. Then subtracting Eq. (2.29) from (2.26) and (2.27) leads to

$$0 = \overline{u_i' \frac{\partial p'}{\partial x_j}} - \frac{1}{\tau_v} (\overline{2u_{A_i}' u_{A_j}'} - \overline{u_{A_i}' u_j'} - \overline{u_i' u_{A_j}'}) + \epsilon \quad (2.30)$$

$$0 = \frac{1}{\tau_v} (\overline{u_i' u_j'} - \overline{u_j' u_{A_i}'}) - \overline{u_{A_i}' \frac{\partial p'}{\partial x_j}} + v \text{ terms} \quad (2.31)$$

Also, from Eq. (2.24) it is possible to show that

$$2\overline{u_{A_i}' u_{A_j}'} - \overline{u_{A_i}' u_j'} - \overline{u_i' u_{A_j}'} = \overline{u_{A_i}' u_{A_j}'} - \overline{u_i' u_j'} + 0(\tau_v q/\Lambda)^2 \quad (2.32)$$

Thus, Eq. (2.30) leads directly to

$$\overline{u_{A_i}' u_{A_j}'} = \overline{u_i' u_j'} + \tau_v (\overline{u_i' \frac{\partial p'}{\partial x_j}} + \epsilon)$$

Which with our usual model for $\overline{u_i' \partial p' / \partial x_j}$ and ϵ gives

$$\overline{u_{A_i}' u_{A_j}'} = \overline{u_i' u_j'} + \frac{\tau_v q}{\Lambda} (\overline{u_i' u_j'} - \frac{q^2}{4} \delta_{ij}) \quad (2.33)$$

Similarly, from Eqs. (2.25) and (2.28)

$$\begin{aligned} \overline{c' u_{A_i}'} &= \overline{c' u_i'} + \tau_v c' \frac{\partial p'}{\partial x_i} \\ &= \overline{c' u_i'} (1 + A \tau_v q / \Lambda) \end{aligned} \quad (2.34)$$

It is surprising to note from Eqs. (2.33) and (2.34) that the leading term in $q\tau_v/\Lambda$ actually adds to both the particle velocity variance and its mass flux. The correlation $\overline{c'u}$ is reduced as $q\tau_v/\Lambda$ increases but the leading term in this reduction appears to be $O(q\tau_v/\Lambda)^2$.

Table I gives some values of τ_v for different size particles to aid in determining when $(q\tau_v/\Lambda) \ll 1$ is a valid approximation. Since Λ grows proportional to z near the surface it is possible to estimate the height at which $q\tau_v/\Lambda = 1$ for a given typical value of q (1 m/sec). At large distances above this height, the approximation should be valid. Thus, for most aerosols smaller than that associated with a fine mist ($\sigma \approx 50 \mu\text{m}$) the approximation is valid at heights greater than a few meters above the surface.

In the surface layer itself we must consider a more complete analysis. There is also a problem with the extremely small particles. If the stopping distance $q\tau_v$ is less than the Kolmogorov microscale, η , of the turbulence, then the particle cannot be transferred all the way to the surface by turbulence. Instead it must be diffused by Brownian motion across the surface sublayer. From Tennekes and Lumley (1972), $\eta = (\nu^2/\epsilon)^{1/4}$ and from our model $\epsilon = q^3/8\Lambda$, thus

$$\eta = (8\Lambda)^{1/4}(\nu/q)^{3/4} \quad (2.35)$$

The minimum η occurs when $\Lambda \approx \eta$ at the edge of the sublayer, so that

$$\eta_{\min} = 2\nu/q \quad (2.36)$$

Table I includes values of $q^2\tau_v/2\nu$ which show that for turbulent air with $q \approx 1$ m/sec typical particles with diameters less than approximately $1 \mu\text{m}$ must involve Brownian diffusion through a portion of the surface layer. Table I also includes values of D for these particles. When $q^2\tau_v/2\nu > 1$, particles will be carried by direct inertial impact to the surface. For particles below approximately $50 \mu\text{m}$ the approximation of $q\tau_v/\Lambda \ll 1$ will describe this turbulent diffusion down to the level we would ordinarily apply our surface boundary condition. For larger particles we must allow $q\tau_v/\Lambda$ to be order one or larger in the surface layer.

The time scale of the turbulence in the surface layer is sufficiently small that it is generally close to equilibrium conditions with negligible contributions from the left-hand side of Eqs. (2.23) and (2.28). As long as attention is restricted to the constant shear stress region, the turbulent diffusion terms in the correlation equation also contribute little to the balance. This gives validity to the approximation termed "Super-Equilibrium" by Donaldson, 1973. The Super-Equilibrium approximation to Eqs. (2.20) and (2.23) for the surface layer is

TABLE I

AEROSOL TRANSPORT PROPERTIES

(Spherical particles with $\rho_A = 1 \text{ gm/cm}^3$ in air at 20°C , 1 ATM; and $q = 1 \text{ m/sec}$)

Particle diameter 2σ (μm)	Diffusion Coefficient D^\dagger cm^2/sec	Relaxation time τ_v^\dagger (sec)	Terminal velocity $\tau_v g$ (cm/sec)	Height at which $q \cdot \tau_v / \Lambda = 1$ (m)	stopping distance microscale $q^2 \tau_v / 2v$
0.1	6.7×10^{-6}	8.8×10^{-8}	8.6×10^{-5}		2.9×10^{-3}
0.5	6.3×10^{-7}	1.0×10^{-6}	1.0×10^{-3}		3.3×10^{-2}
1.0	2.8×10^{-7}	3.6×10^{-6}	3.5×10^{-3}		0.12
5	4.9×10^{-8}	8.0×10^{-5}	7.8×10^{-2}	12.3×10^{-5}	2.7
10	2.4×10^{-8}	3.2×10^{-4}	3.1×10^{-1}	5×10^{-4}	10.6
50		7.7×10^{-3}	7.58	.012	2.6×10^2
100		3.1×10^{-2}	30.3	.048	1.0×10^3
500		7.7×10^{-1}	757.	1.18	2.6×10^6

 † Friedlander, 1977.

$$-\overline{u'_{A_i} w'_A} \frac{\partial \bar{c}}{\partial z} - \bar{c} \overline{u'_{A_i} \frac{\partial u'_A}{\partial x_j}} - \frac{\overline{c' u'_{A_i}} - \bar{c}' \bar{u}'_i}{\tau_v} = 0 \quad (2.37)$$

and

$$\begin{aligned} & -(\bar{u}_{A_i} - \bar{u}_j) \overline{u'_i \frac{\partial c'}{\partial x_j}} - \overline{u'_i w'_A} \frac{\partial \bar{c}}{\partial z_j} - \overline{c' w'} \frac{\partial \bar{u}_i}{\partial z} \\ & - \overline{(u'_{A_j} - u'_j) u'_i \frac{\partial c'}{\partial x_j}} - \overline{c' \frac{\partial p'}{\partial x_i}} = 0 \end{aligned} \quad (2.38)$$

To keep our approximation simple, the three terms $\overline{u'_{A_i} \frac{\partial u'_A}{\partial x_j}}$, $(\bar{u}_{A_j} - \bar{u}_j) \overline{u'_i \frac{\partial c'}{\partial x_j}}$ and $\overline{(u'_{A_j} - u'_j) u'_i \frac{\partial c'}{\partial x_j}}$ will be dropped since they all go to zero in both limits of $\tau_v \rightarrow 0$ and $\tau_v \rightarrow \infty$. The usual model of the last term in Eq. (2.38) should be modified to permit it to approach zero as $\tau_v \rightarrow \infty$. An appropriate choice appears to be

$$\overline{c' \frac{\partial p'}{\partial x_j}} = \frac{Aq \overline{c' u'_i}}{\Lambda(1 + K_1 q \tau_v / \Lambda)} \quad (2.39)$$

In the limit of $\tau_v \rightarrow 0$, Eq. (2.39) gives the decorrelation term as inversely proportional to the turbulent time scale, but when the slip time τ_v , is larger than Λ/q the term becomes inversely proportional to τ_v .

Rather than attempt to determine sufficient new models to obtain $\overline{u'_{A_i} w'_A}$ and $\overline{u'_i w'_A}$ from Eqs. (2.21) and (2.22), we will approximate both as

$$\overline{u'_{A_i} w'_A} = \overline{u'_i w'_A} = \overline{u'_i w'} / [1 + K_2 (q \tau_v / \Lambda)^2] \quad (2.40)$$

This approximation may be rationalized by noting that

$$u'_{A_i} = e^{-t/\tau_v} \int_0^t e^{t'/\tau_v} u' \frac{dt'}{\tau_v} \quad (2.41)$$

as long as the nonlinear term in Eq. (2.18) is ignored. If we also approximate u' as an harmonic oscillation, then Eq. (2.41) leads to

$$\overline{u'^2_A} = \overline{u' u'_A} = \overline{u'^2} / [1 + (q \tau_v / \Lambda)^2] \quad (2.42)$$

Equations (2.37) through (2.42) lead to

$$\overline{c'u_{Ai}} = \overline{c'u_i} - \tau_v \overline{u_i w} \frac{\partial \bar{c}}{\partial z} \left/ \left[1 + K_2 (q\tau_v/\Lambda)^2 \right] \right. \quad (2.43)$$

and

$$\frac{Aq\overline{c'u_i}}{\Lambda} \left[\frac{1}{1+K_1 q\tau_v/\Lambda} \right] = - \frac{\overline{u_i w}}{[1+K_2 (q\tau_v/\Lambda)^2]} \frac{\partial \bar{c}}{\partial z} - \overline{c'w} \frac{\partial \bar{u}_i}{\partial z} \quad (2.44)$$

These two equations may be rearranged to give

$$\overline{c'w} = - \frac{\Lambda}{Aq} \overline{w'w'} \frac{\partial \bar{c}}{\partial z} \left[\frac{1+K_1 q\tau_v/\Lambda}{1+K_2 (q\tau_v/\Lambda)^2} \right] \quad (2.45)$$

$$\overline{c'w_A} = - \frac{\Lambda}{Aq} \overline{w'w'} \frac{\partial \bar{c}}{\partial z} \left[\frac{1+(A+K_1)q\tau_v/\Lambda}{1+K_2 (q\tau_v/\Lambda)^2} \right] \quad (2.46)$$

Equation (2.46) may also be written as

$$\overline{c'w_A} = \overline{c'w} \left[\frac{1+(A+K_1)q\tau_v/\Lambda}{1+K_1 q\tau_v/\Lambda} \right] \quad (2.47)$$

which, for $q\tau_v/\Lambda \ll 1$, agrees to $O(q\tau_v/\Lambda)$ with Eq. (2.34). This leaves us with two coefficients K_1 and K_2 to determine turbulent transport of particles in the surface layer when $q\tau_v/\Lambda \geq 0(1)$.

In summary, our proposed approximation for turbulent transport of aerosols is based on writing the diffusion equation for \bar{c} as

$$\frac{\partial \bar{c}}{\partial t} + \frac{\partial \bar{c}\bar{u}_i}{\partial x_i} = S - \frac{\partial}{\partial x_i} \left[\bar{c} \frac{\tau_v}{\rho} \frac{\partial \bar{p}}{\partial x_i} + \overline{c'u_i} \left(\frac{1+(A+K_1)q\tau_v/\Lambda}{1+K_1 q\tau_v/\Lambda} \right) \right] \quad (2.48)$$

with the mass flux equation modified to

$$\begin{aligned} \frac{\partial \overline{c'u_i}}{\partial t} + \bar{u}_j \frac{\partial \overline{c'u_i}}{\partial x_j} = & - \frac{\overline{u_i u_j}}{1+K_2 (q\tau_v/\Lambda)^2} \frac{\partial \bar{c}}{\partial x_j} - \overline{c'u_j} \frac{\partial \bar{u}_i}{\partial x_j} \\ & + v_c \frac{\partial (q\Lambda)}{\partial x_j} \frac{\partial \overline{c'u_i}}{\partial x_j} - \frac{Aq}{\Lambda} \frac{\overline{c'u_i}}{(1+K_1 q\tau_v/\Lambda)} \end{aligned} \quad (2.49)$$

with the only restriction that $c \ll 1$. Above the surface layer, $q\tau_v/\Lambda$ will be small and only the mean drift term in Eq. (2.48) will be important. While in the surface layer where $q\tau_v/\Lambda$ can become of $O(1)$, Eqs. (2.48) and (2.49) lead to the same Super-Equilibrium relations as just given.

In combination with Eqs. (2.48) and (2.49) we must allow the effective height z_{oc} at which the aerosol concentration reaches the surface value to be a function of $q\tau_v$ as well as a function of surface characteristics. In fact for many atmospheric problems it appears that this change in surface boundary condition will be the major influence of particle size on turbulent transport of aerosols.

Aerosol surface deposition data is typically presented in terms of a deposition velocity, v_d , defined by the surface flux divided by the surface concentration (e.g., Chamberlain, 1967). The actual value of v_d depends on the height chosen to measure the 'surface' concentration due to the possibility of strong gradients near the surface. Within the neutral constant flux layer, Eqs. (2.48) and (2.49) reduce to

$$K \frac{\partial \bar{c}}{\partial z} + \tau_v g \bar{c} = v_d c_d \quad (2.50)$$

with

$$K = \frac{q\Lambda}{3} \left[\frac{1 + (A + K_1)q\tau_v/\Lambda}{1 + K_2(q\tau_v/\Lambda)^2} \right]$$

and

$$\Lambda = 6.5z$$

The general solution to Eq. (2.50) may be written as

$$c = \frac{v_d c_d}{\tau_v g} + (\text{const}) \exp \left[-\tau_v g \int K^{-1} dz \right] \quad (2.51)$$

When the boundary condition that

$$c = c_d \quad \text{at} \quad z = z_d$$

is applied to Eq. (2.51) it leads to

$$\frac{c}{c_d} = \frac{v_d}{\tau_v g} + \left(1 - \frac{v_d}{\tau_v g} \right) \exp \left[-\tau_v g \int_{z_d}^z K^{-1} dz \right] \quad (2.52)$$

As $\tau_v \rightarrow 0$, $K \rightarrow 0.22 qz$ and

$$\frac{c}{c_d} \rightarrow \frac{v_d}{.22q} \ln z/z_d + 1, \quad (2.53)$$

the classical logarithmic concentration variation. For finite values of τ_v Eq. (2.52) can be used to determine z_{oc} when v_d at any z_d is known.

3. MODEL CALCULATIONS

The general A.R.A.P. atmospheric boundary layer model, which includes the fluid mechanics of mean flow dynamics and turbulence; transport, evaporation, and condensation of water; and atmospheric radiation, has been exercised for a variety of situations. These exercises have been selected to demonstrate the power of the model in predicting a variety of archetypal atmospheric flow situations including fog episodes, diurnal variation of stratus over the ocean, the general structure of the trade-wind boundary layer, and an evaporatively cooled gust front. These exercises were selected with particular attention to corresponding experimental measurements of similar or identical flow situations.

3.1 Marine Boundary Layer Calculations

A major study of the interaction of turbulence with atmospheric radiation in a class of fog and stratus cloud episodes is described in Appendix A which is a reprint of work to be published in the Journal of the Atmospheric Sciences. In addition to the illustration of fog and cloud formation, development and dissipation for various situations, we present in Appendix A a theory of the moist atmospheric surface layer which provides a quantitative classification of foggy and fog-free surface layers dominated by turbulence. We further include, where available, observations of fog and stratus extent, cooling rates and liquid water content and show favorable comparison with the A.R.A.P. model.

A full comparison of the A.R.A.P. predictions of the dynamics and evolution of the boundary layer would require measurements of the fluid state at an initial state and at some subsequent time. Unfortunately, so far, we have been unable to obtain such sequential measurements. We are thus only able to provide a verification of the consistency of the A.R.A.P. model in the sense that the turbulence co-existing with the measured mean profiles at one time is well represented by the turbulence correlations predicted by the A.R.A.P. model for the same mean profiles. This is demonstrated in Appendix B where calculations for a trade-wind boundary layer which has received some experimental study have been carried out. These calculations based on the data summary and analysis of Lemone and Pennell (1974) and more recent GATE data also provide some limited comparison with alternative turbulence models based on direct three-dimensional calculation of the turbulence with modeling of the subgrid turbulent correlations (Deardorff, 1972; Sommeria, 1976).

As is well known, direct solution of an ensemble of instantaneous Navier-Stokes equations for the turbulent motions of the atmosphere is not a feasible or practical computation. A class of turbulent models which attempt direct calculation of the large-scale turbulence but which do not compute the small scales (of the order of the grid size and smaller) are known

as subgrid-scale turbulence models (Deardorff, 1972). In these computations the critical modeling centers on the sub-grid turbulent correlations which are structured within the grid length and time scales to lie in the so-called "inertial" range of the energy spectrum of the motion being computed. Such calculations must of necessity be fully three-dimensional and time-dependent - and hence computationally voluminous - even when the mean motion is principally one- or two-dimensional or steady.

The essential predictions of both calculations under these conditions are the dynamics of evolution to and the final slowly varying state over a period of several hours following initialization. Some arbitrariness necessarily underlies the comparison since the predicted quantities are not conceptually identical. The A.R.A.P. second-order closure model predicts the ensemble-average of the system. The calculation of Sommeria predicts the temporal average of the horizontal spatial average of the system. Specifically, for atmospheric scale motions of the order of 30 minutes, Sommeria calculates at 5 s time steps, averages the variables over the horizontal spatial coordinate and then averages these quantities over 4 minute periods. These 4 minute temporal averages are probably the quantities most closely related to the A.R.A.P. ensemble average.

The basic features of this comparison are as follows. Below the clouds and in the mixed layer the turbulent momentum flux, vertical velocity variance, and virtual heat flux compare very favorably as shown in Figs. 4 to 7 in Appendix B. There is, however, a sharp difference in the average density of liquid water in the clouds predicted by the two models which in turn strongly affects the turbulence structure in the cloud primarily through the liquid water droplet I.R. radiation interaction. The average liquid water content is exceedingly low in the subgrid turbulence calculation (10^{-5} - 10^{-6}) and perhaps too high (for the scattered cumulus case) in the A.R.A.P. calculation (10^{-4}). Correspondingly, there is about a factor of three to five difference in the turbulent humidity fluxes. As a result of the higher levels of water in the A.R.A.P. simulated clouds, turbulence production due to cloud-top cooling is enhanced over that in the subgrid turbulence model and there are relative maxima of turbulence in the clouds as well as in the mixed layer below the clouds. The resolution of these differences between the two models remains to be given. We are convinced that the simple A.R.A.P. averaging algorithm for the liquid water content considering the fluctuations about the saturated state gives results which agree within approximately 10 percent with those for the more complex Gaussian moment method used in the subgrid turbulence models (Sommeria and Deardorff, 1976). We have also shown good agreement between the A.R.A.P. liquid water predictions and measurements of the liquid water in fog and stratus events (see Appendix A). The discrepancy between the two models likely stems from the nature of averaging in the widely disparate states of scattered cumulus and continuous stratus.

3.2 Gust Front Formed by Evaporative Cooling

As a demonstration calculation, we present the results of a problem for which both nonhydrostatics and water change of phase are important. Rain falling through unsaturated air will cool the air as evaporation takes place. This air with its negative buoyancy can then form a downdraft which, when it impinges upon the ground spreads out to form the local gust front often associated with severe thunderstorms. We have made calculations of this phenomena for NASA (Teske and Lewellen, 1977) to determine the windshear and turbulence distributions present because of their potential hazard to aircraft operations. In those calculations the influence of evaporation was simulated by introducing a cold downdraft of some specified temperature defect at a given height z_{\max} with vertical velocity W_d . The downdraft is then permitted to fall and interact with the ground to form the outward spreading gust front.

For the present calculation, we introduce a downward jet at 1.6 km height, as shown in Fig. 3.1, with no virtual potential temperature defect with respect to its surroundings. We will show the results of two computations. For case A, the jet is supersaturated with a relatively large liquid water content, and for case B the jet is dry. By comparing the results of the two cases, it is possible to clearly see the role of evaporation in accelerating the resulting gust front. It should also be noted that, whereas Teske and Lewellen (1977) deals with an axisymmetric downdraft, the present calculations are for two-dimensional downdrafts. Other conditions such as height of the simulation domain and the boundary conditions on vorticity and velocity there, boundary conditions at the outer edge of the domain, and surface roughness are all the same. Initial conditions are also prescribed in a similar fashion by taking the boundary values of vorticity and humidity at z_{\max} and extrapolating them linearly to their surface values of $n_{o_i} = 0$ and $H = (0.86)H_s$. The turbulence is initialized as isotropic with $q_{\max}(=3 \text{ m/sec})$ sufficiently small that it can be dominated by turbulent production.

The resulting temperature pattern, as it evolves in time, is shown in Fig. 3.2. Contours of constant virtual potential temperature are shown at three times, $t = 200, 500, 750$ secs, for case A. At $t = 0$, $\theta_v = 0$ everywhere as it remains in case B. The maximum virtual potential temperature defect is 5.6° , and occurs 300 seconds after the start of the run. The absolute temperature of the air actually rises as the air moves down into regions of higher pressure by compression. But in order to stay saturated at the higher absolute temperature, it evaporates some of the liquid water present and is cooler than it would be if it descended along a dry adiabatic curve. At the later times, the -1 contour line shows that the same shape front as evidenced in Fig. 3.2 of Teske and Lewellen, 1977 (reproduced here as Fig. 3.3) has developed.

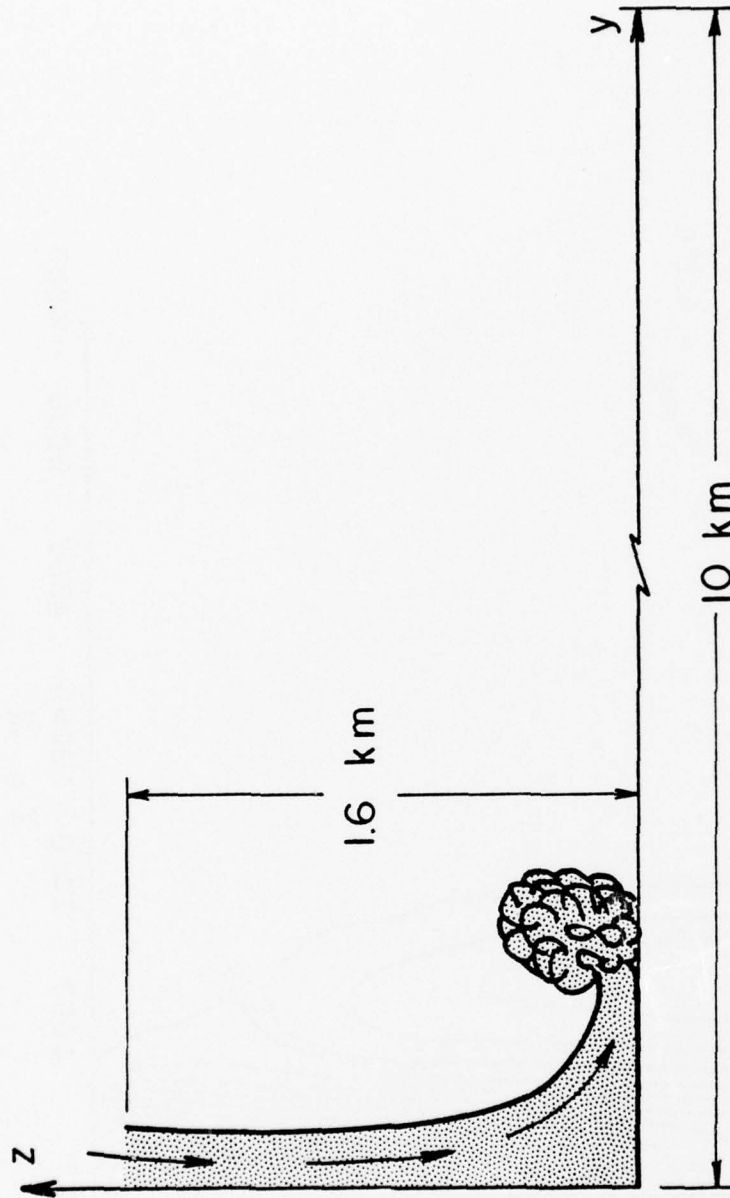


Figure 3.1 Sketch of coordinate system used to simulate the gust front formed by evaporative cooling.

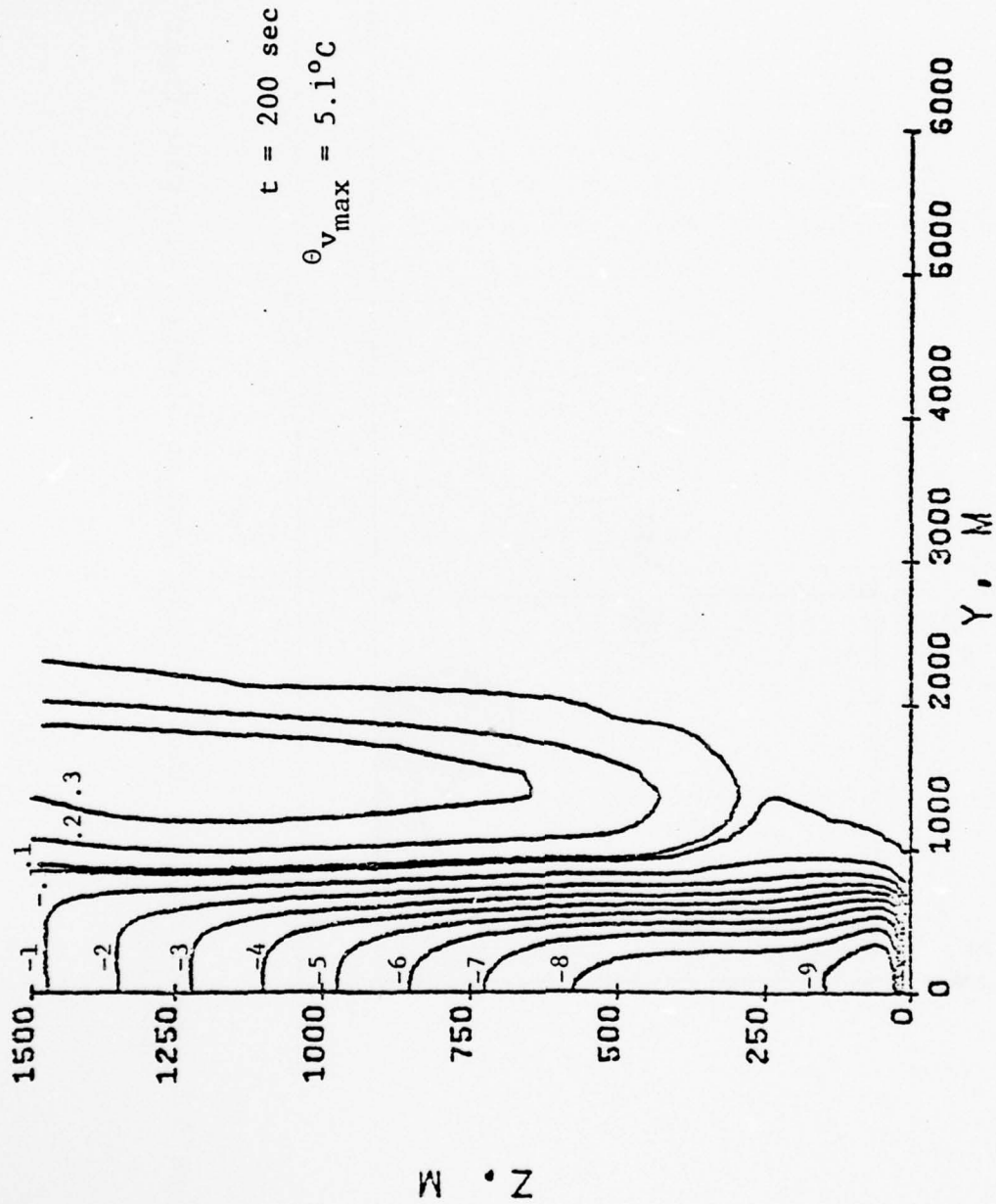


Figure 3.2a Contours of constant virtual potential temperature for case A with evaporation at $t = 200$ secs after initialization. (Contour notation: 9 = 90% of maximum value; 8 = 80% ; -9 = -90% ; .1 = 1% ; -.1 = -1% , etc.)

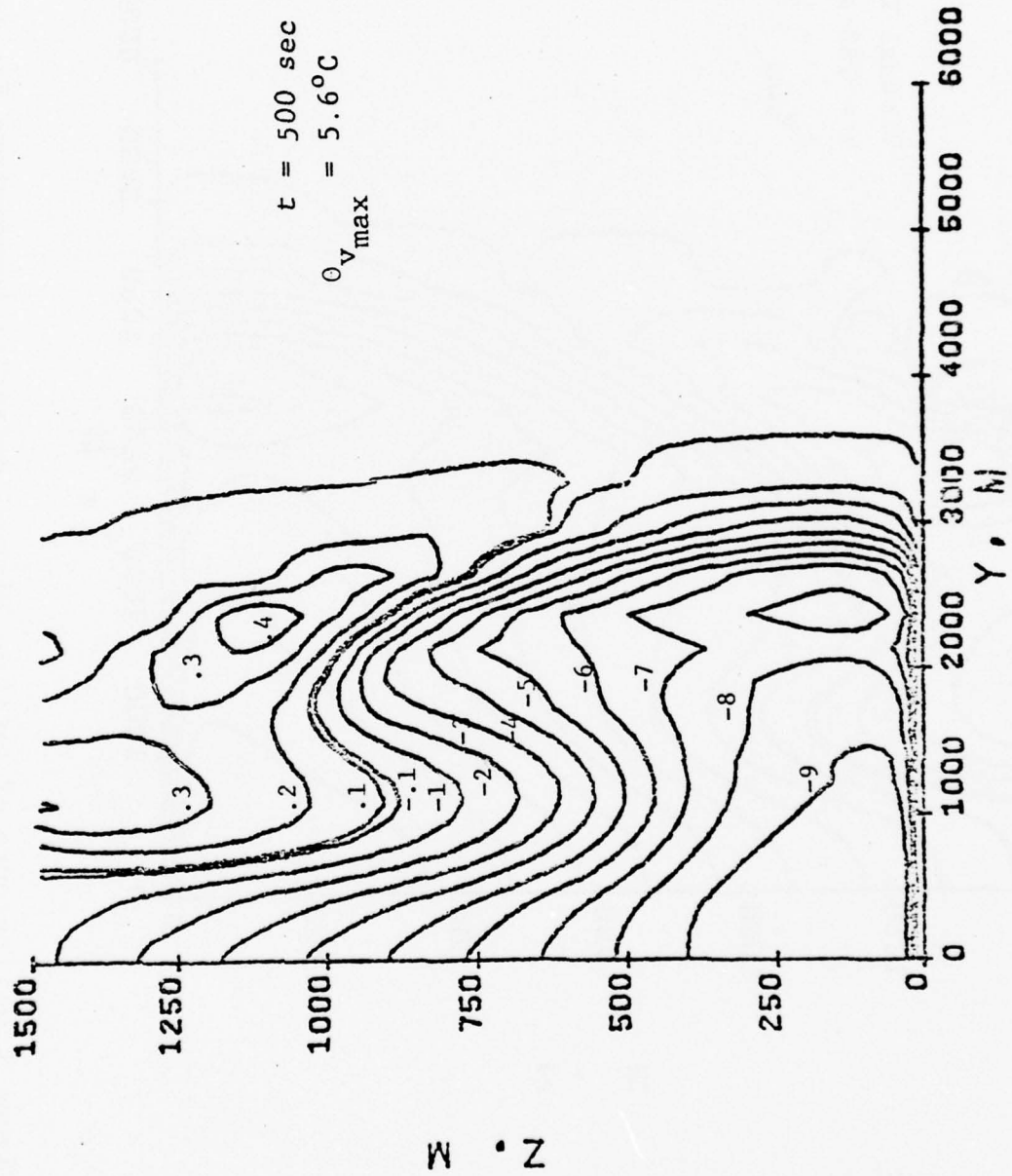


Figure 3.2b Contours of constant virtual potential temperature for case A with evaporation at $t = 500$ sec after initialization. (See Fig. 3.2a for contour notation.)

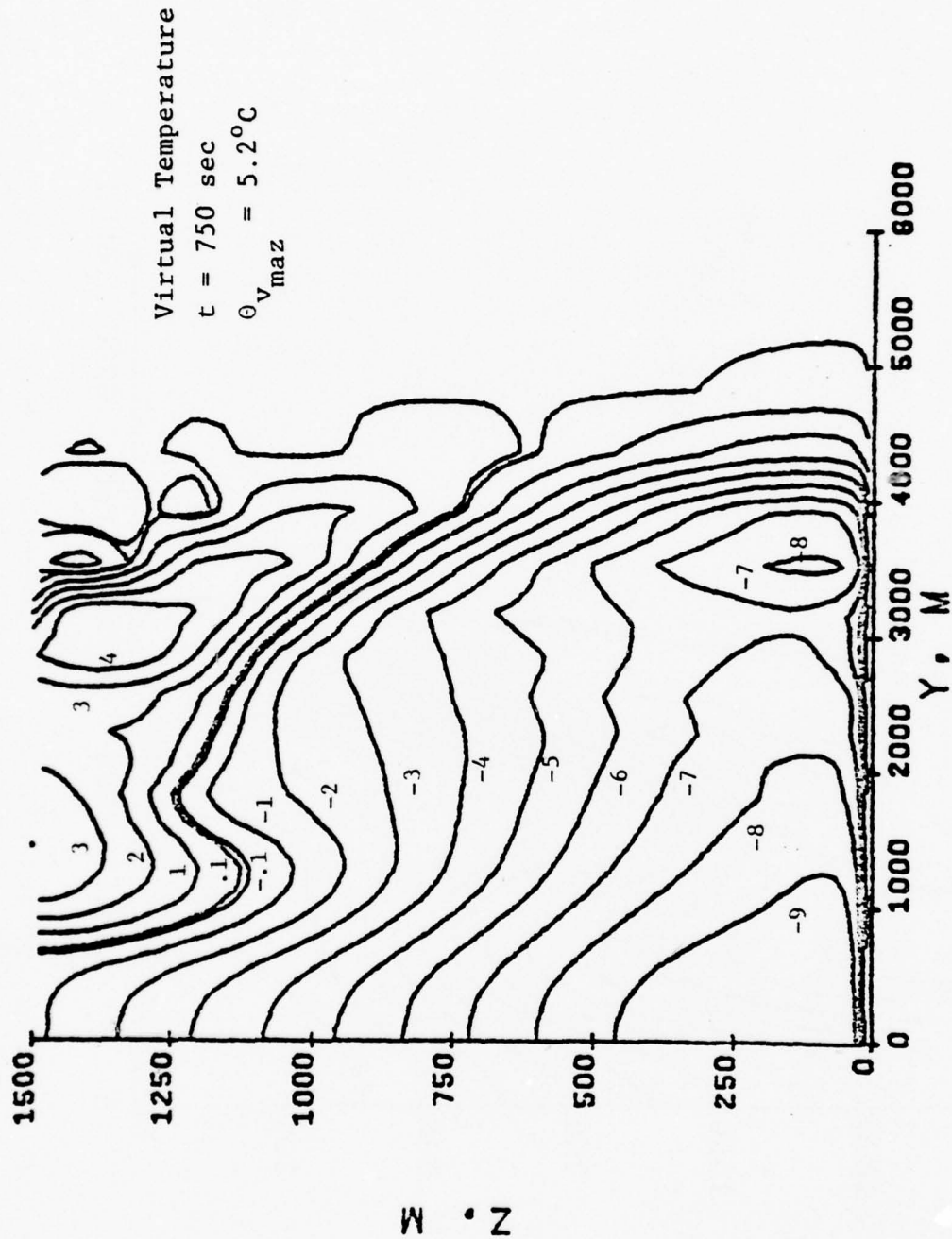


Figure 3.2c Contours of constant virtual potential temperature for case A with evaporation at $t = 750 \text{ sec}$. (See Fig. 3.2a for contour notation.)

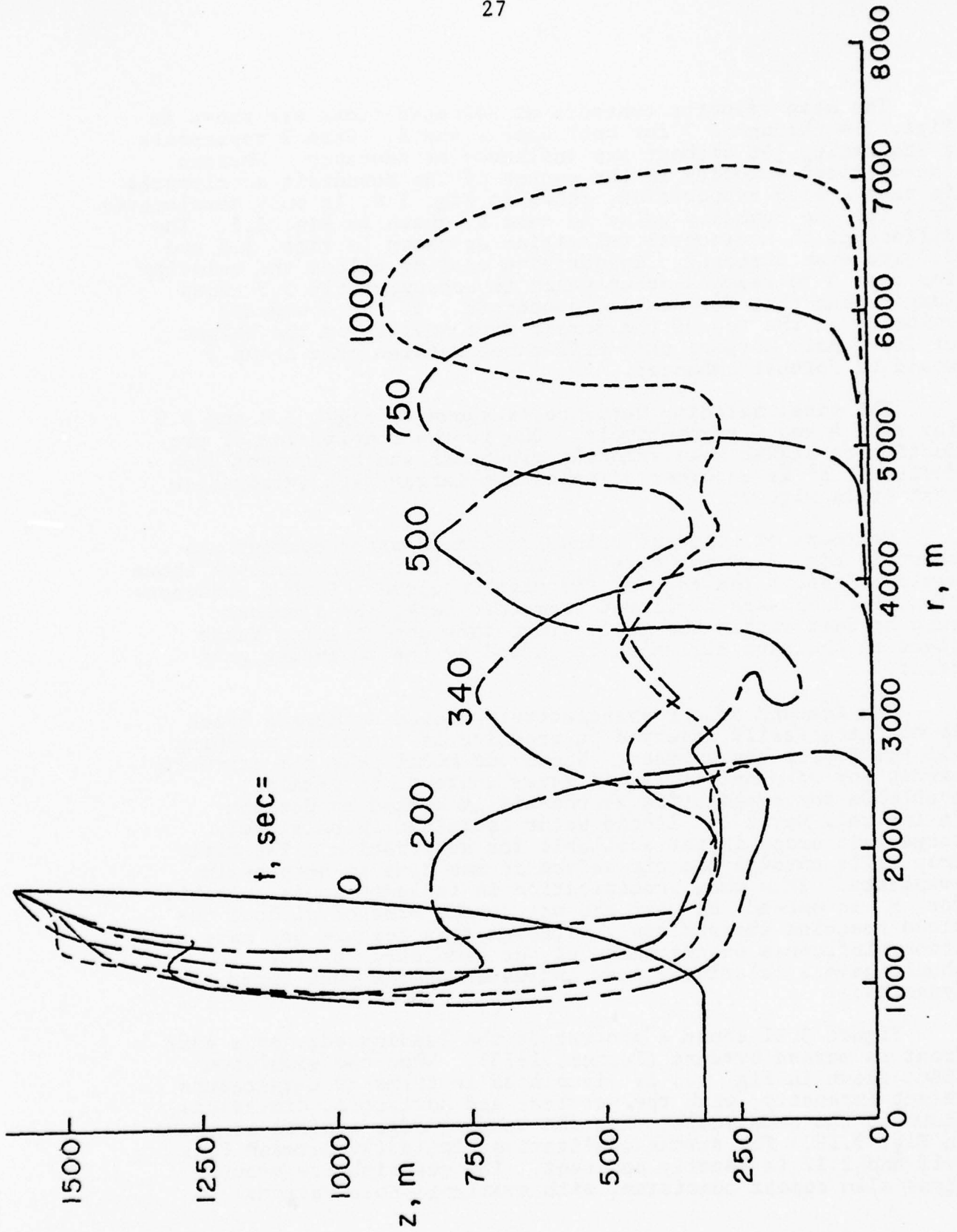


Figure 3.3 Evolution of the isopleth of potential temperature defect ($\Delta\theta = -2^\circ\text{C}$) for the dry, axisymmetric simulation of Teske and Lewellen, 1977.

The mean velocity contours at selected times are shown in Figs. 3.4 through 3.7 for both case A and B. Case B represents a stagnating jet without any influence of buoyancy. Whereas the vertical velocity in the center of the downdraft accelerates in case A with evaporation, shown in Fig. 3.4, it only decelerates from its top boundary value in case B, shown in Fig. 3.5. The difference in horizontal velocities as shown in Figs. 3.6 and 3.7 are even stronger. Evaporative cooling allows the velocity for case A to reach a value which is approximately 2.5 times larger than that for neutral downdraft. If the downdraft velocity at the top of the domain were smaller or the height of the domain larger, this difference between case A and B would be further enhanced.

The total velocity variance is shown in Figs. 3.8 and 3.9 for case A and B respectively. Due to the combination of production by higher mean velocity gradients and by buoyant production, q^2 is an order of magnitude larger with evaporation than it is without.

Contours of constant values of liquid water content are shown in Fig. 3.10 for case A. The smallest value contour shown would represent the edge of the visible cloud. Such a condensation cloud appears different from that marked by a tracer, such as dust within the gust, since some condensation takes place in the warm air which is lifted by the advancing gust front.

One feature of our evaporatively cooled downdraft which is not necessarily observed in practice is the cloud reaching all the way to the surface. Since our model does not currently permit any rain out of liquid water content, it remains available for evaporation as the air is heated by descent. In the real world the liquid water contained in relatively large rain drops is not available for evaporation. The water drop falls through the air before it has time to completely evaporate. Thus when precipitation is included it is possible for H to exceed H_s all the way to the surface without the cloud reaching the surface. Although this feature may have a strong influence on the shape of our simulated "cloud," it should have a relatively weak influence on the gust front dynamics.

Figure 3.11 shows a picture of the leading edge of a gust front as marked by dust (Turner, 1973). When the simulated front shown in Fig. 3.3 is visualized in terms of temperature defect intensity, with the vertical and horizontal dimensions shown to the same scale, then the leading edge appears as shown in Fig. 3.12. The strong qualitative similarity between Figs. 3.11 and 3.12 is readily apparent. The quantitative predictions also appear consistent with available observations.

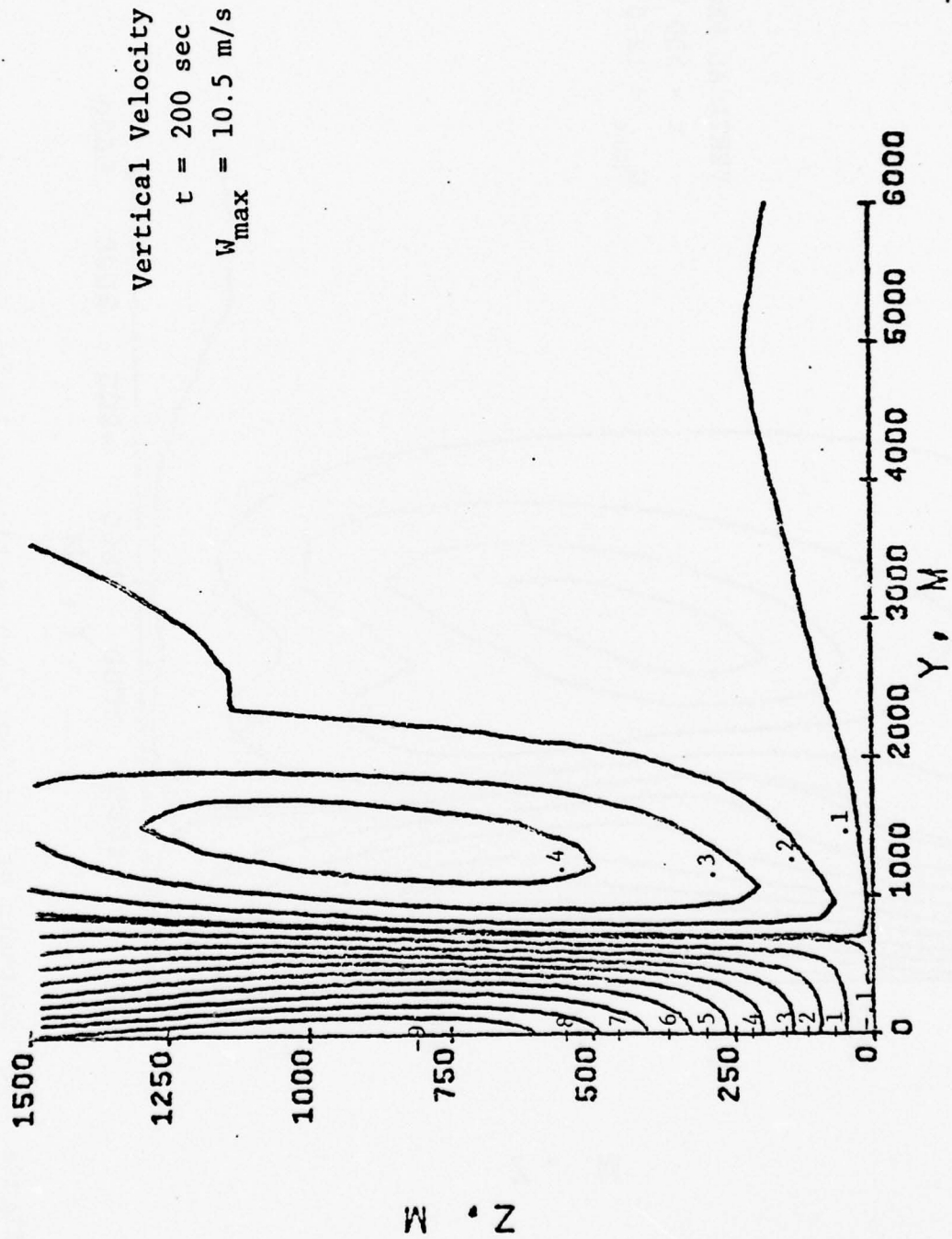


Figure 3.4a Contours of constant mean vertical velocity for case A with evaporation at $t = 200 \text{ sec}$ after initialization.

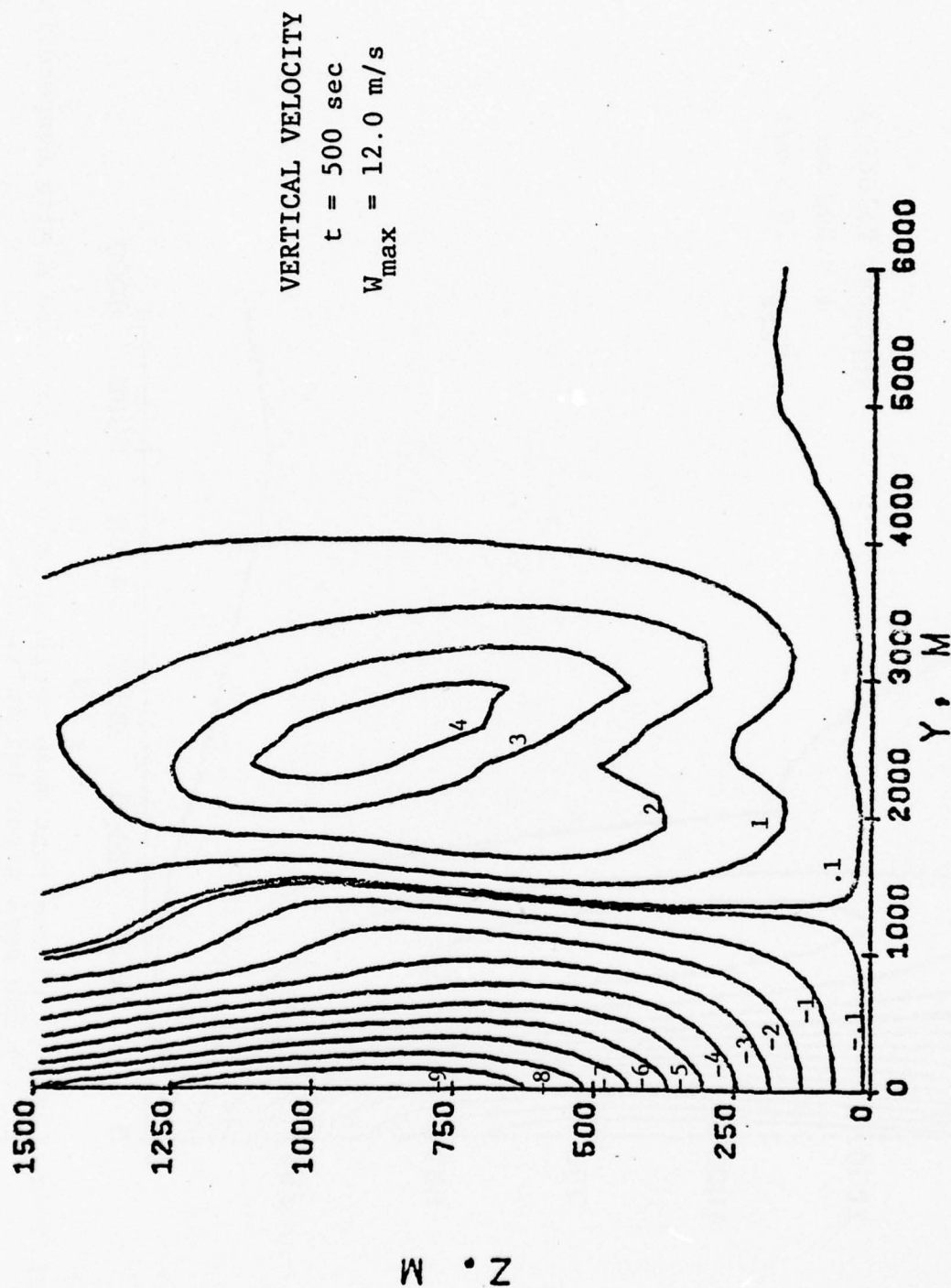


Figure 3.4b Contours of constant mean vertical velocity for case A with evaporation at $t = 500$ secs after initialization.

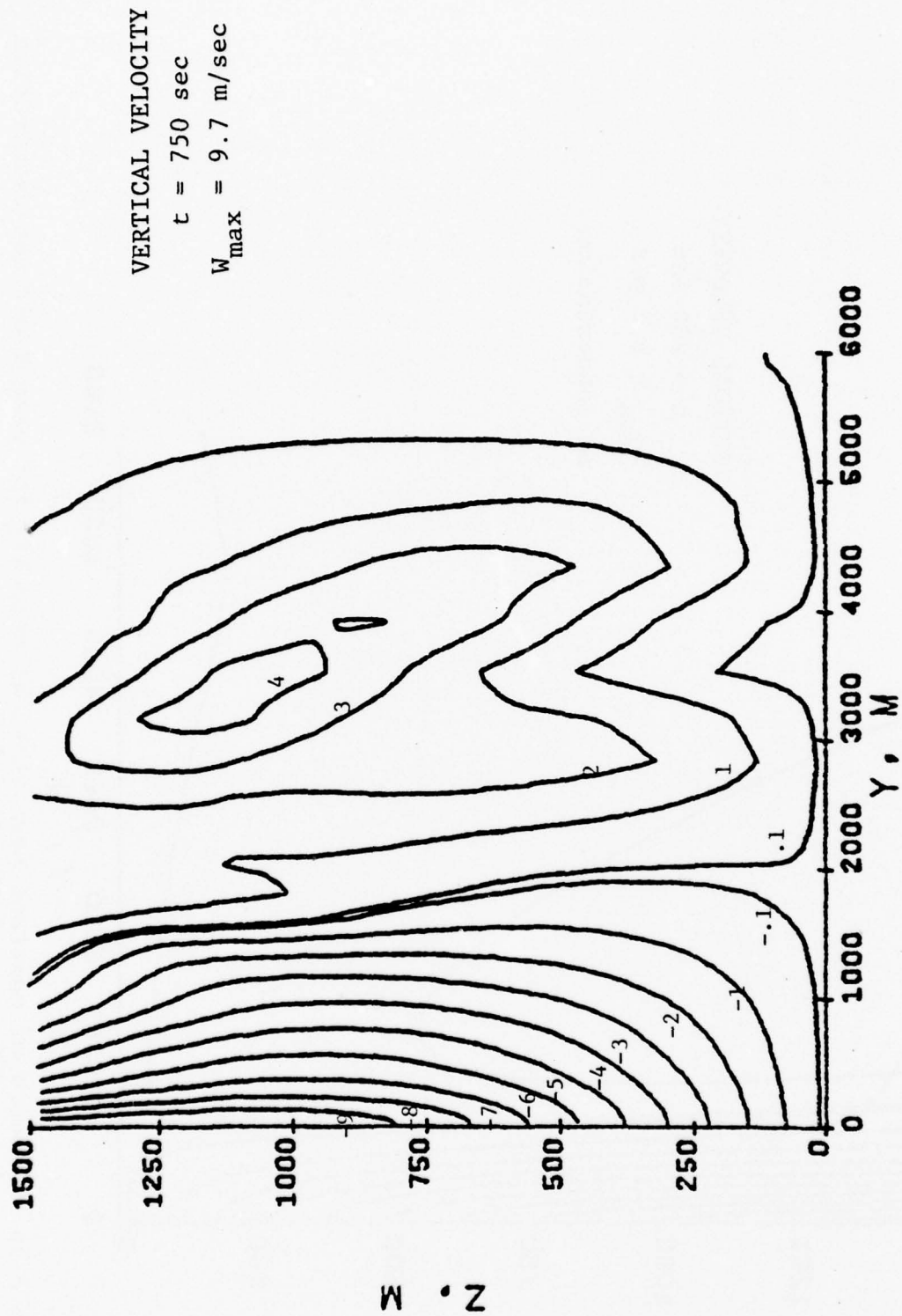


Figure 3.4c Contours of constant mean vertical velocity for case A with evaporation at $t = 750 \text{ sec}$ after initialization.

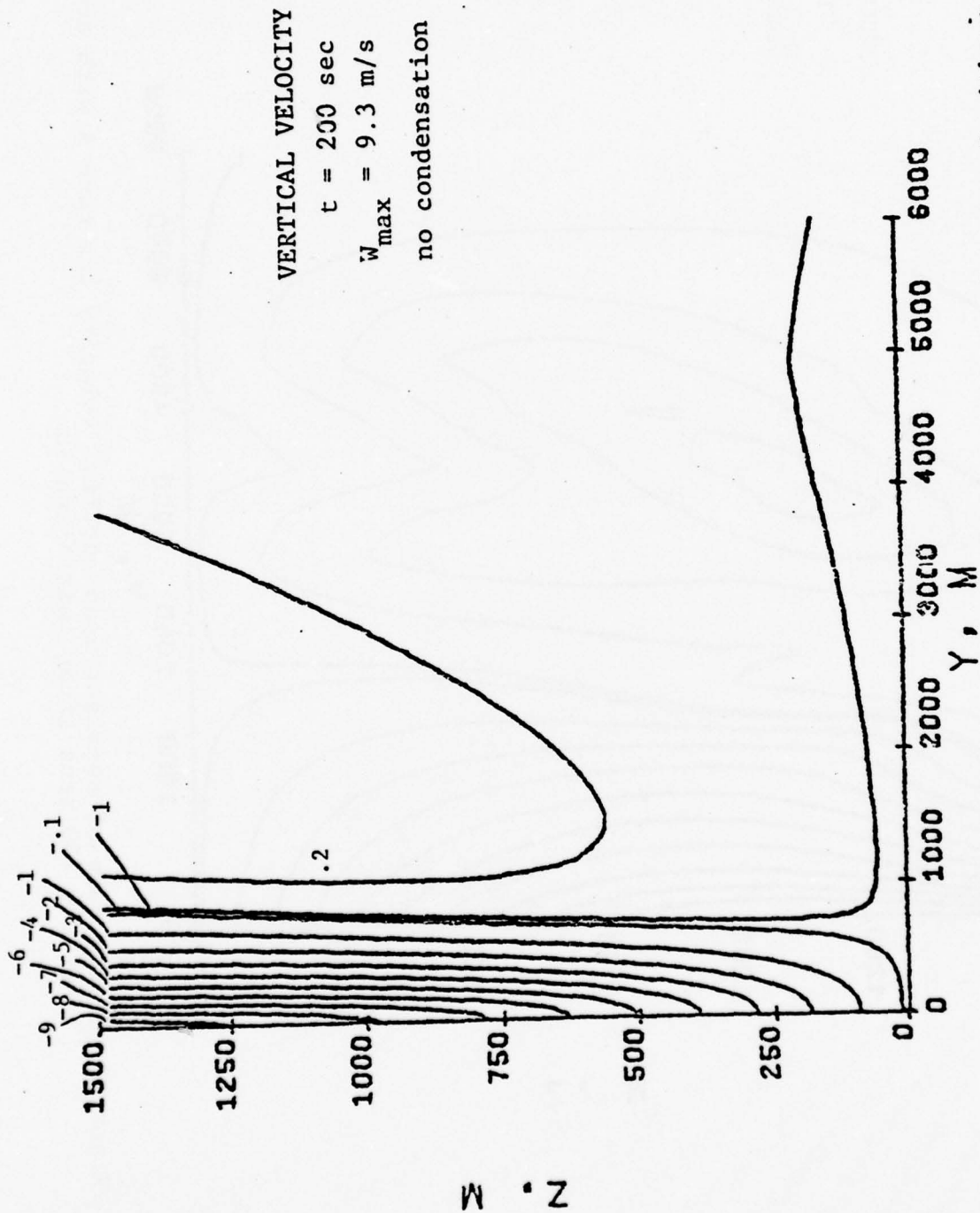


Figure 3.5a Contours of constant mean vertical velocity for case B without evaporation at $t = 200 \text{ sec}$ after initialization.

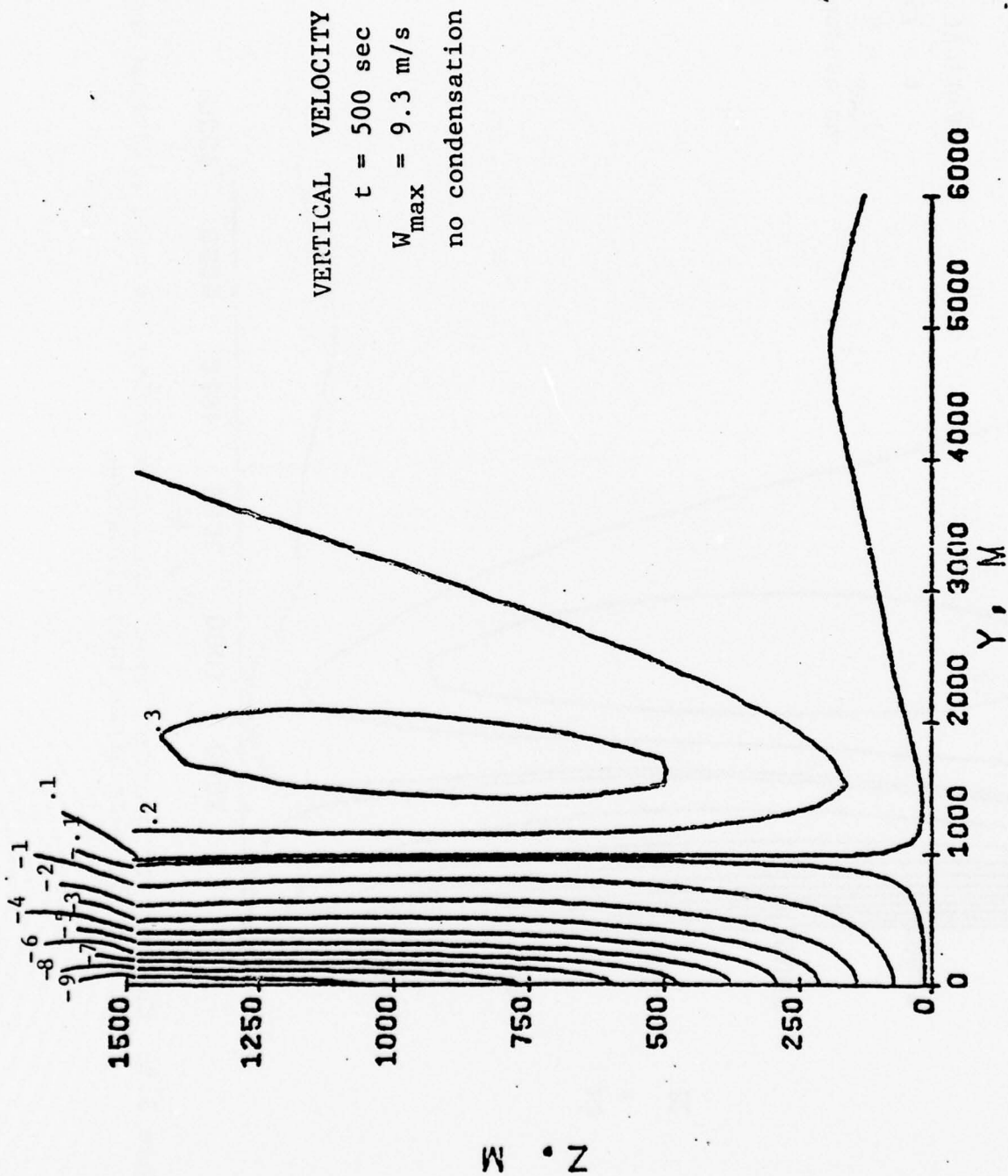


Figure 3.5b Contours of constant mean vertical velocity for case B without evaporation at $t = 500 \text{ sec}$ after initialization.

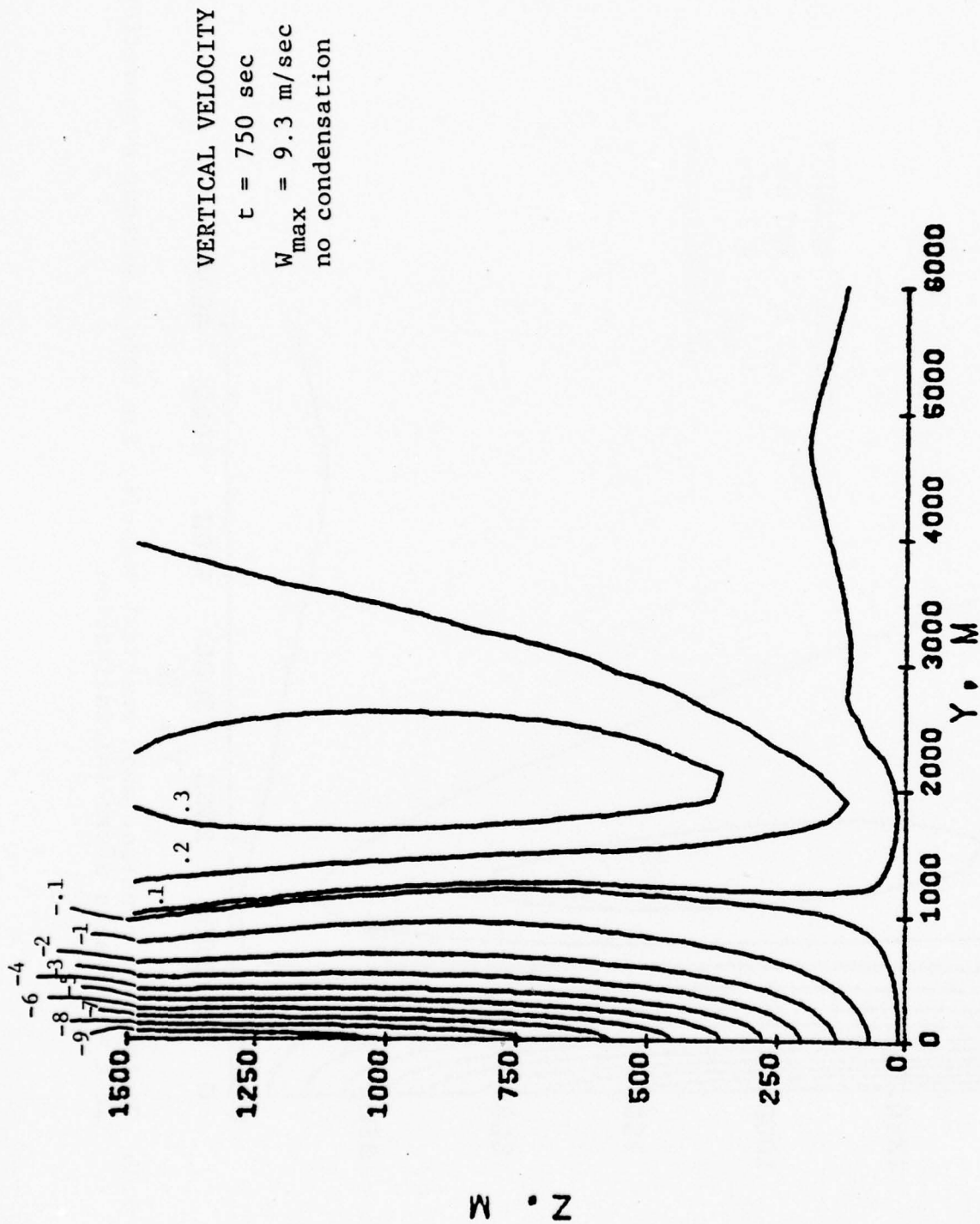


Figure 3.5c Contours of constant mean vertical velocity for case B without evaporation at $t = 750$ secs after initialization.

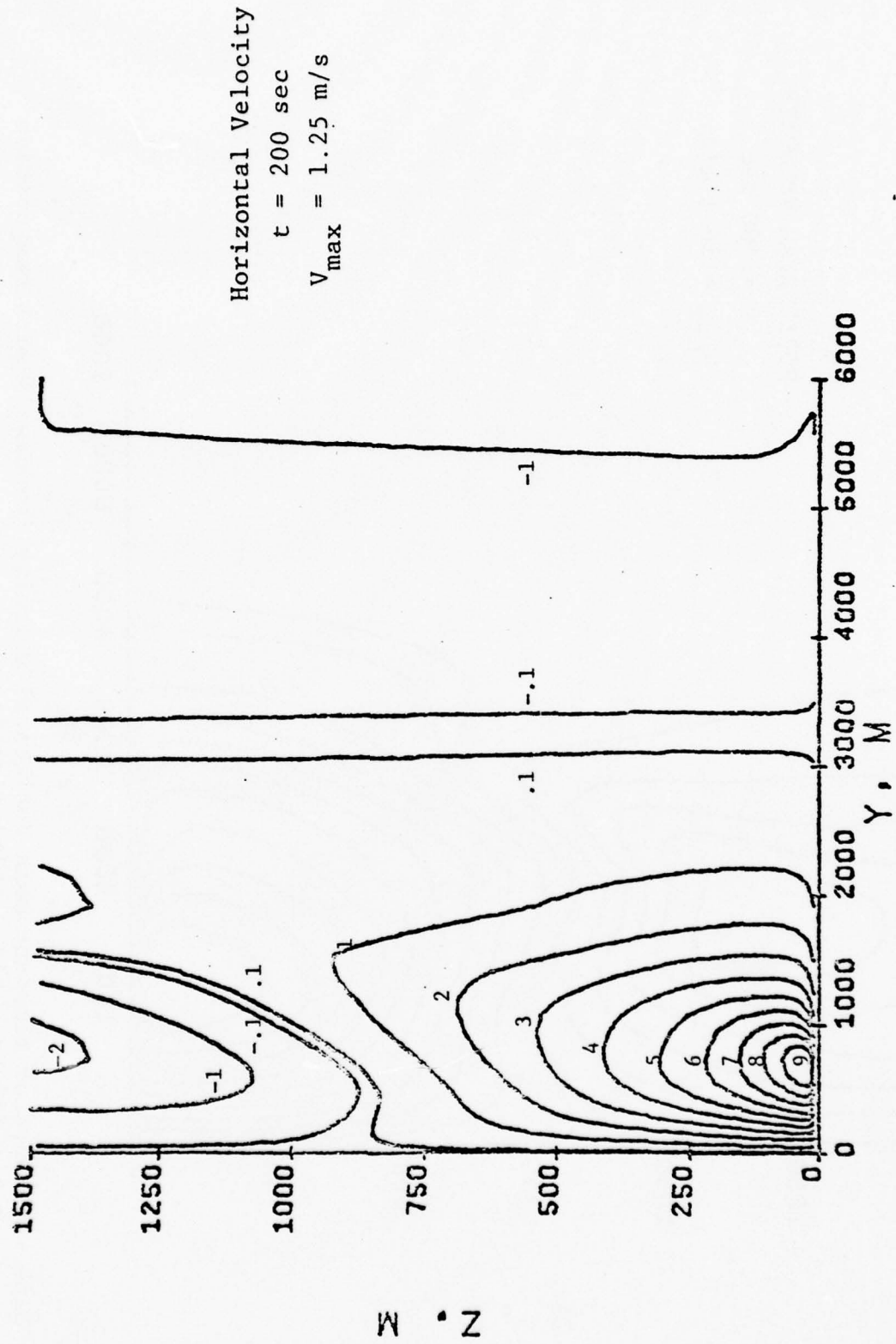


Figure 3.6a Contours of constant mean horizontal velocity for case A with evaporation at $t = 200$ secs after initialization.

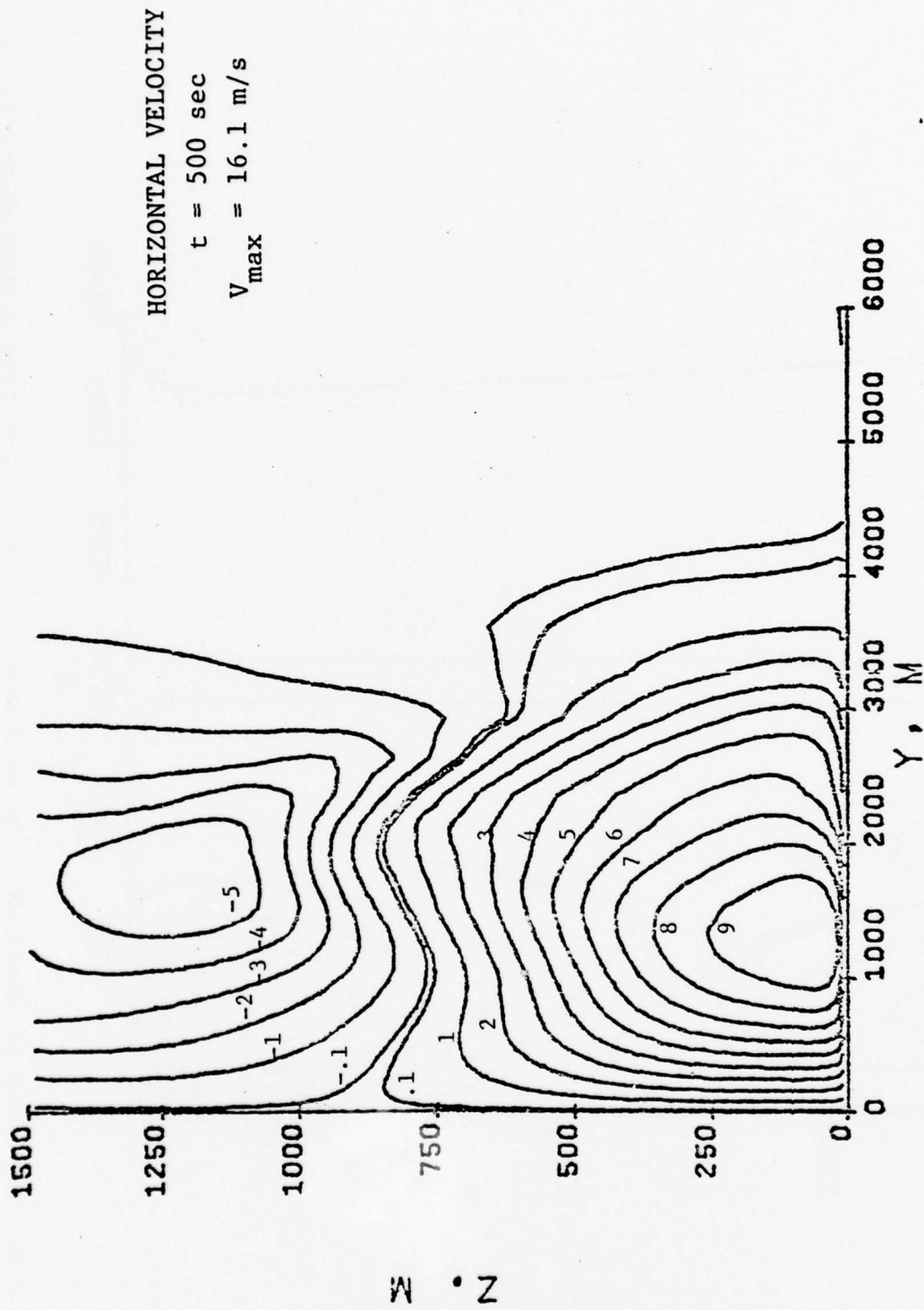


Figure 3.6b Contours of constant mean horizontal velocity for case A with evaporation at $t = 500$ secs after initialization.

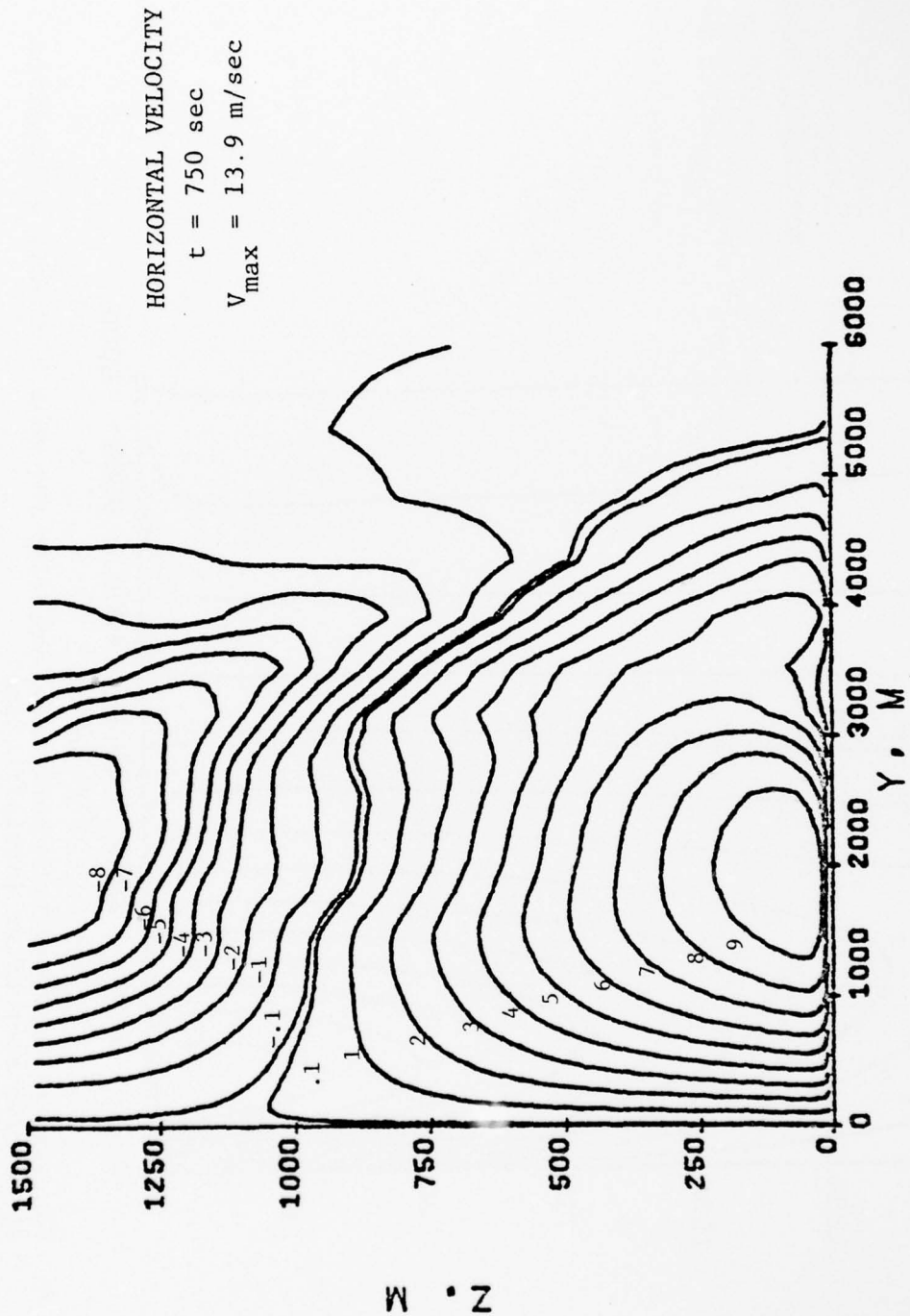


Figure 3.6c Contours of constant mean horizontal velocity for case A with evaporation at $t = 750$ secs after initialization.

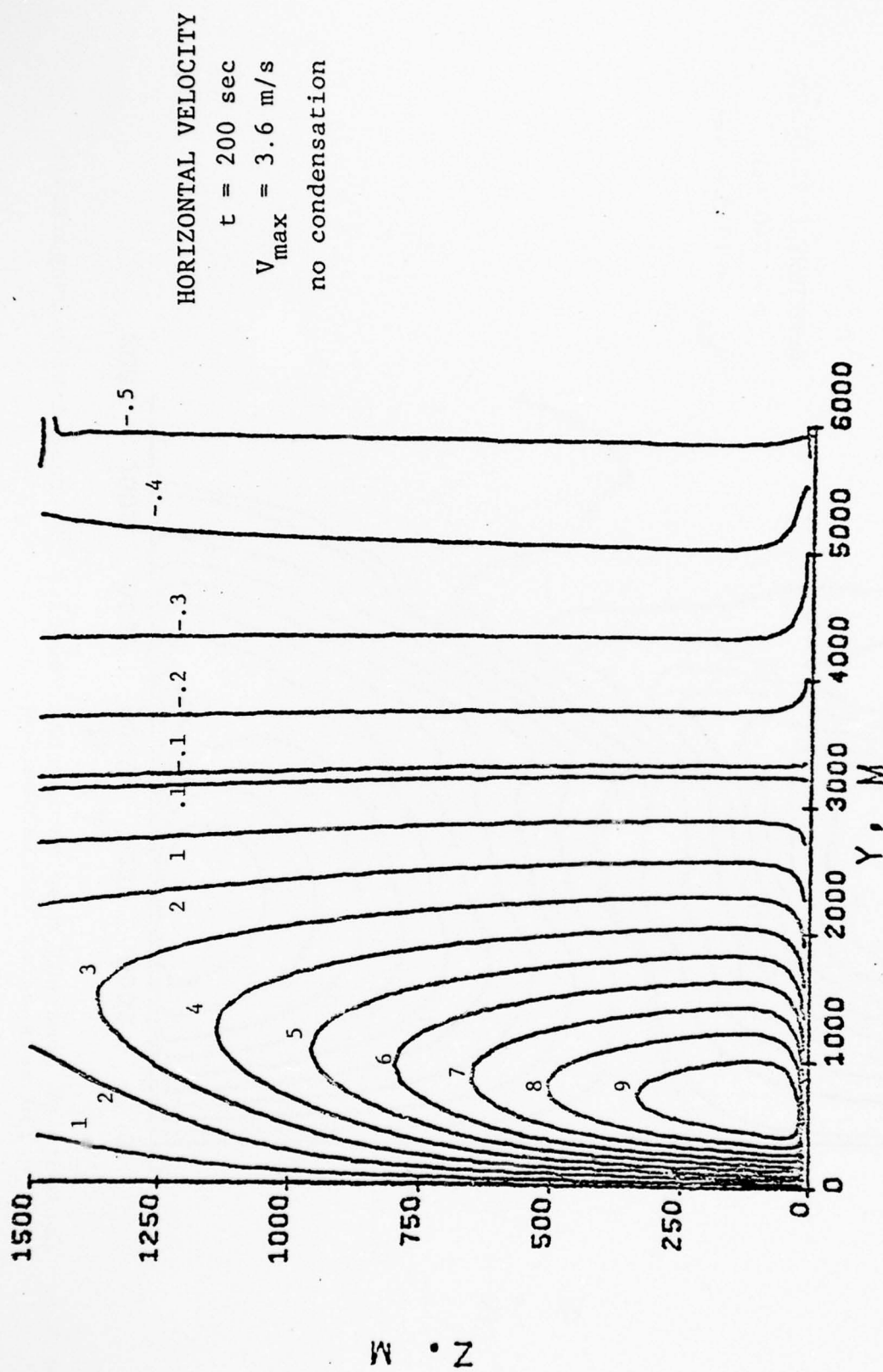


Figure 3.7a Contours of constant mena horizontal velocity for case B without evaporation at $t = 200 \text{ sec}$ after initialization.

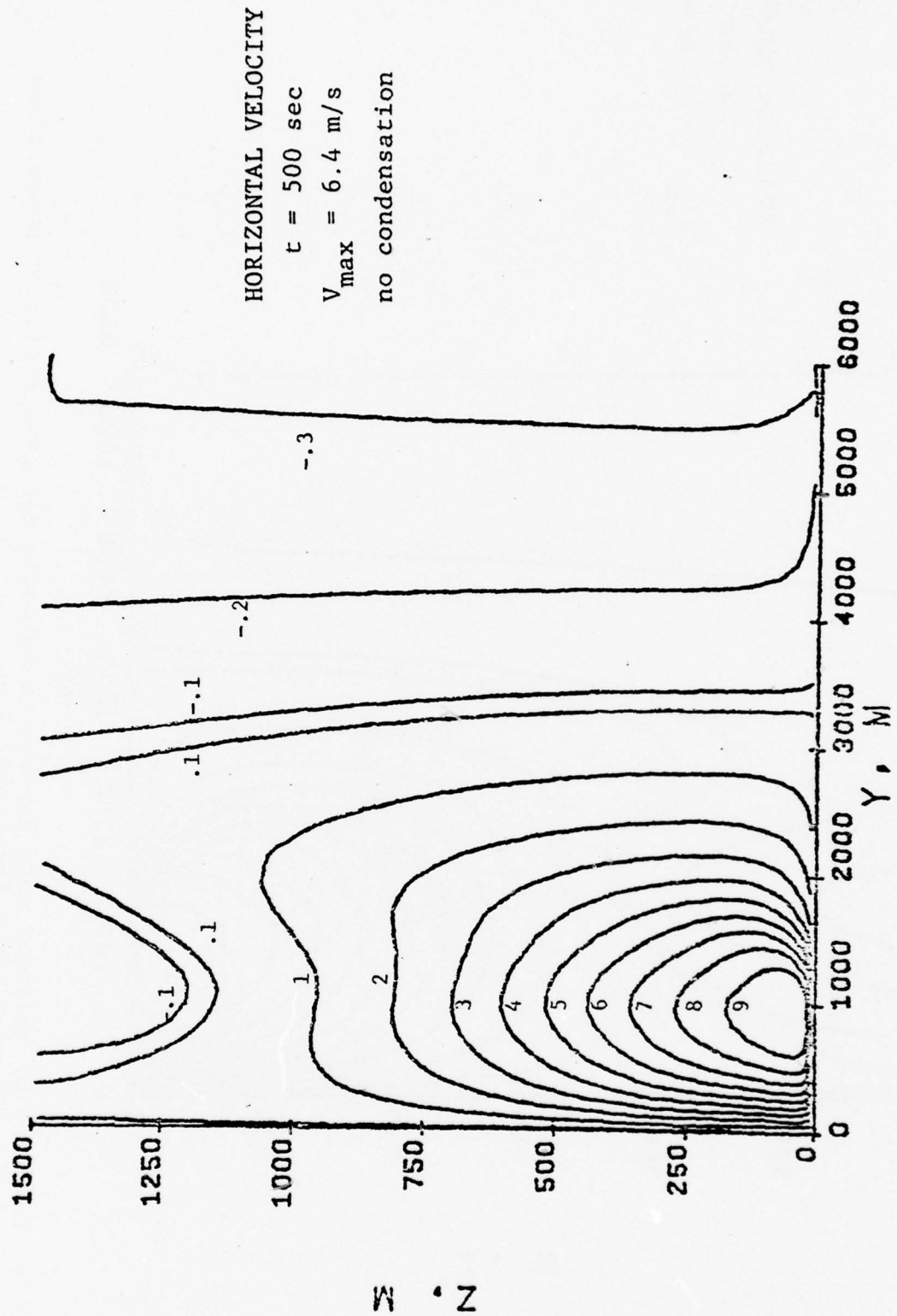


Figure 3.7b Contours of constant mean horizontal velocity for case B without evaporation at $t = 500$ secs after initialization.

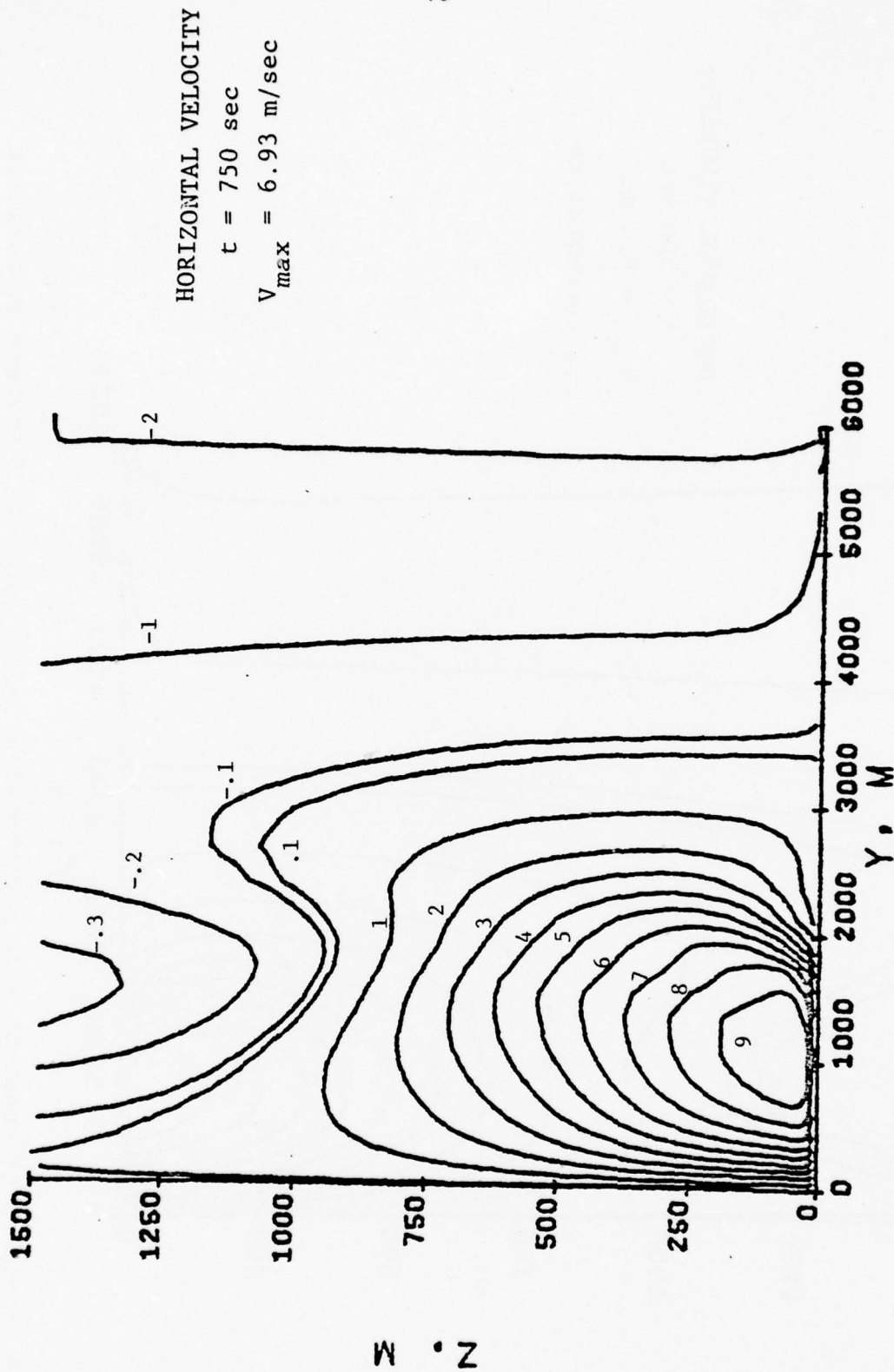
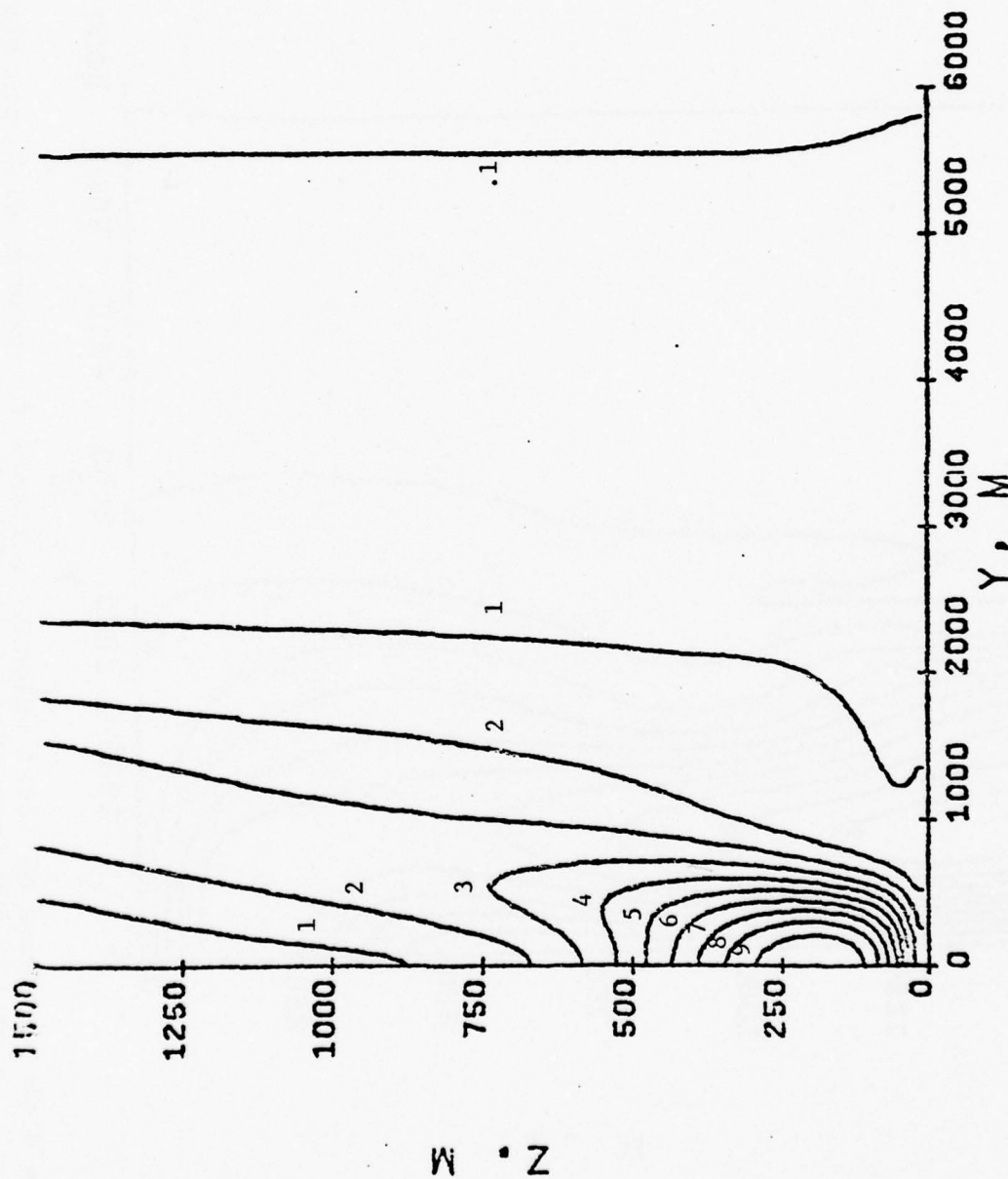


Figure 3.7c Contours of constant mean horizontal velocity for case B without evaporation at $t = 750 \text{ sec}$ after initialization.



TURBULENCE

$t = 200 \text{ sec}$

$q_{\max}^2 = 7.31 \text{ m}^2/\text{s}^2$

41

Figure 3.8a Contours of total velocity variance for case A with evaporation at $t = 200$ secs after initialization.

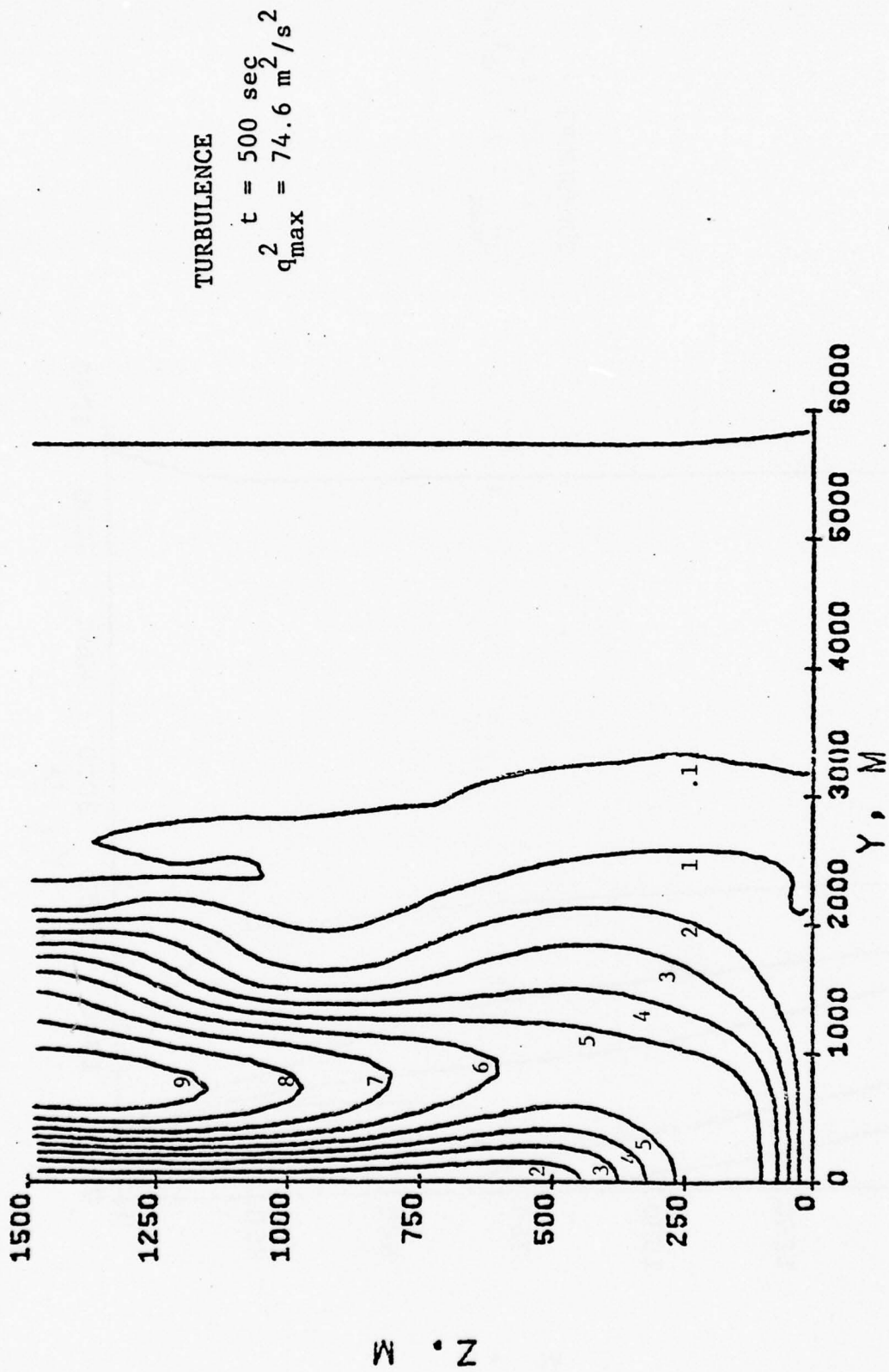


Figure 3.8b Contours of total velocity variance for case A with evaporation at $t = 500$ secs after initialization.

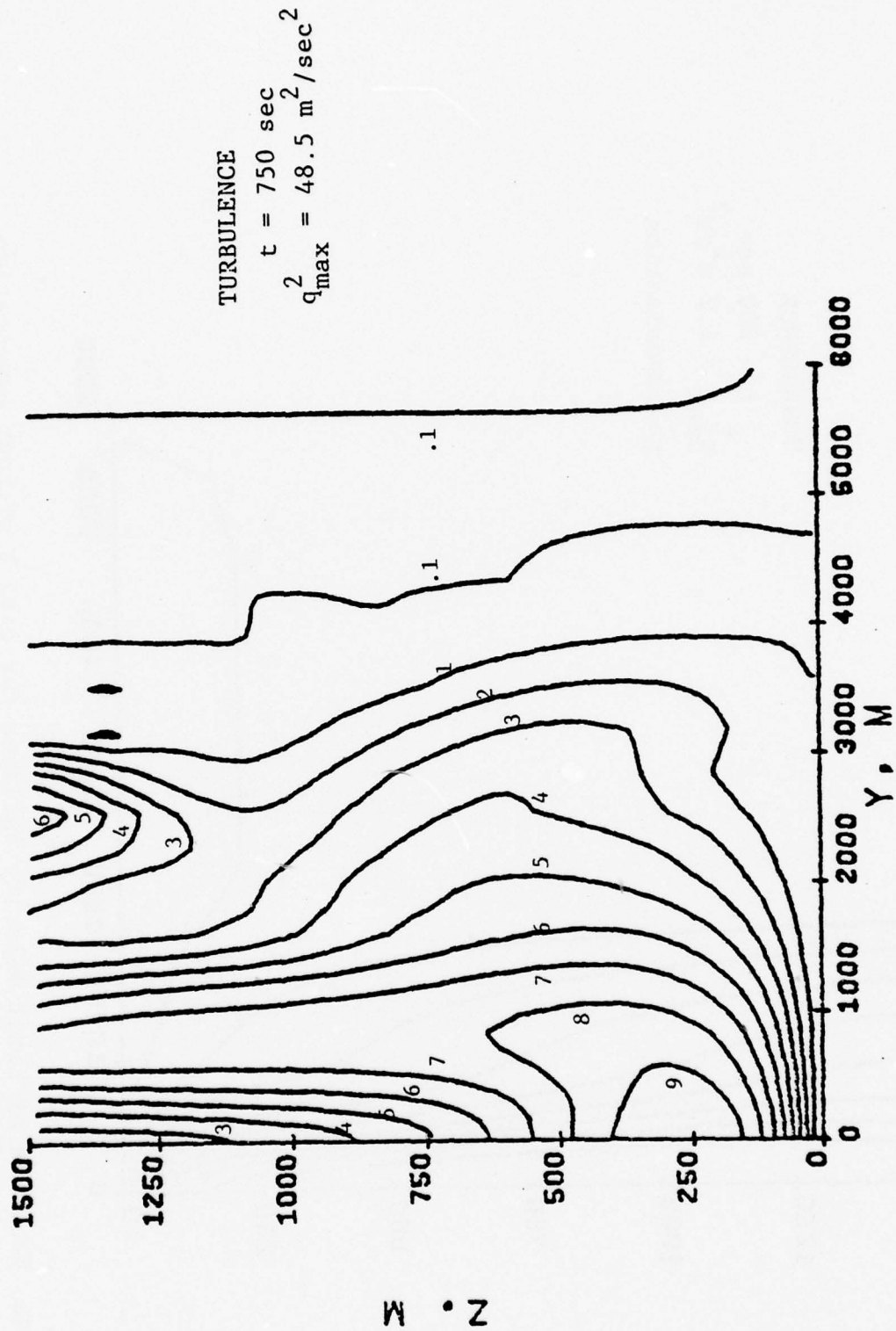


Figure 3.8c Contours of total velocity variance for case A with evaporation at $t = 750$ secs after initialization.

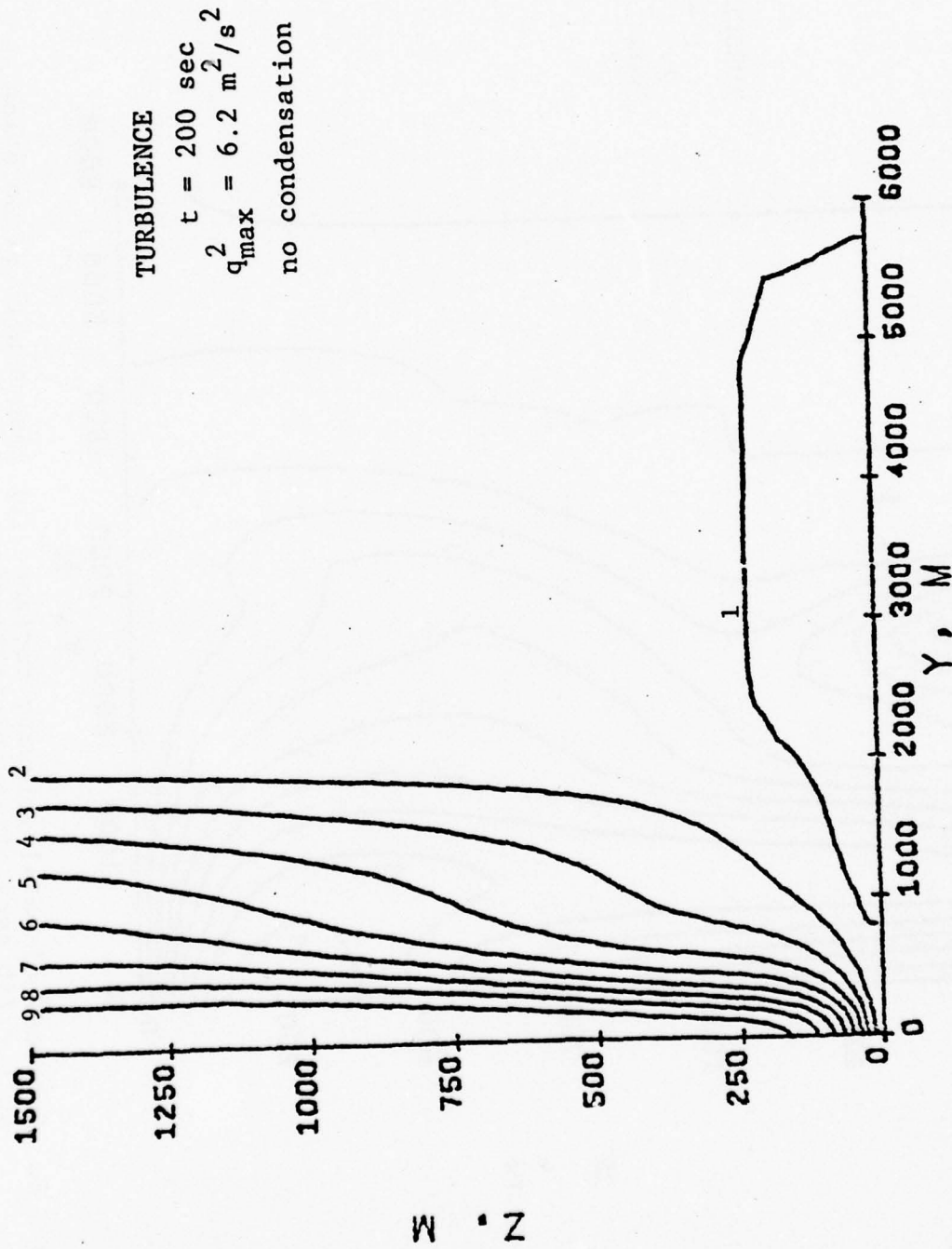


Figure 3.9a Contours of total velocity variance for case B without evaporation at $t = 200$ sec after initialization.

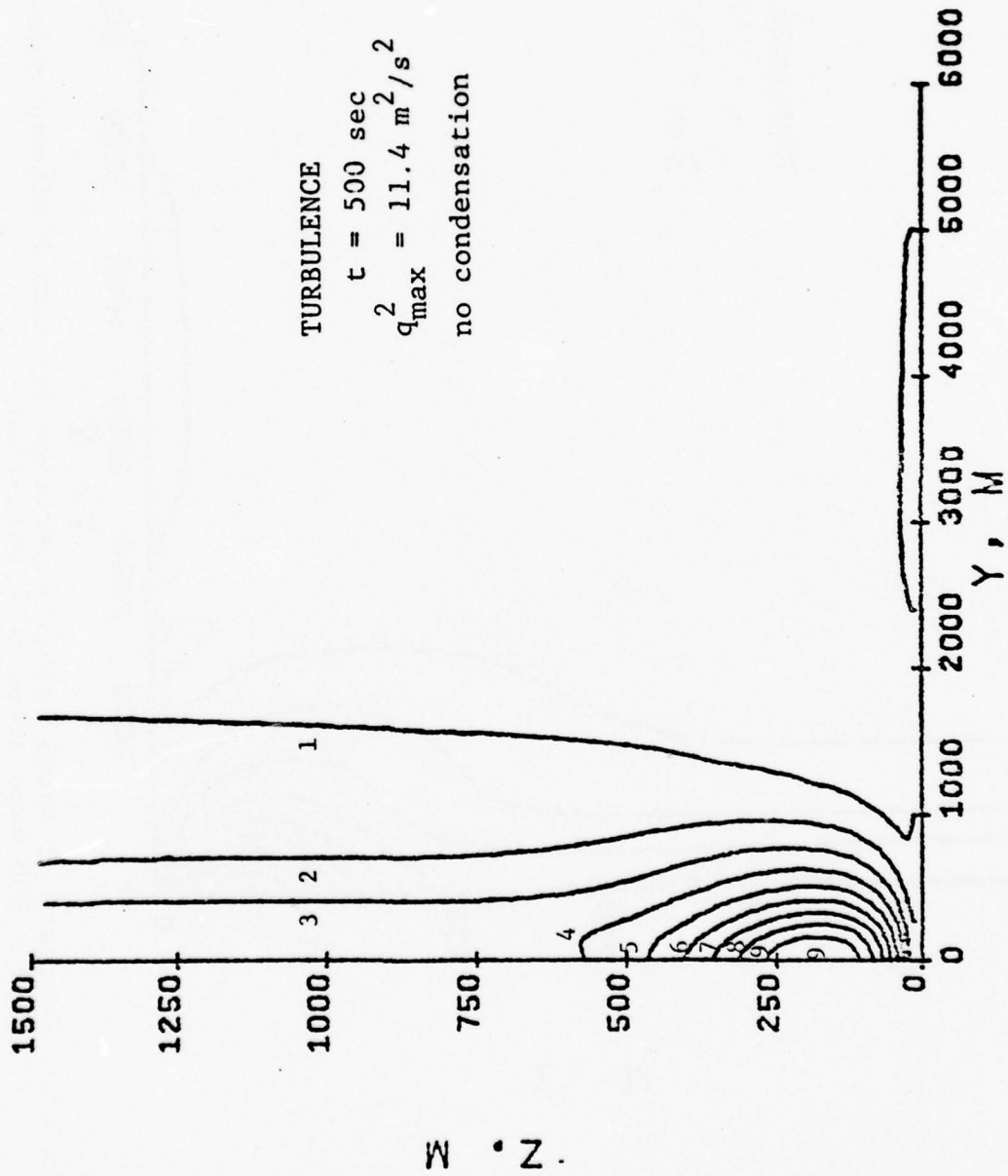


Figure 3.9b Contours of total velocity variance for case B without evaporation at $t = 500$ secs after initialization.

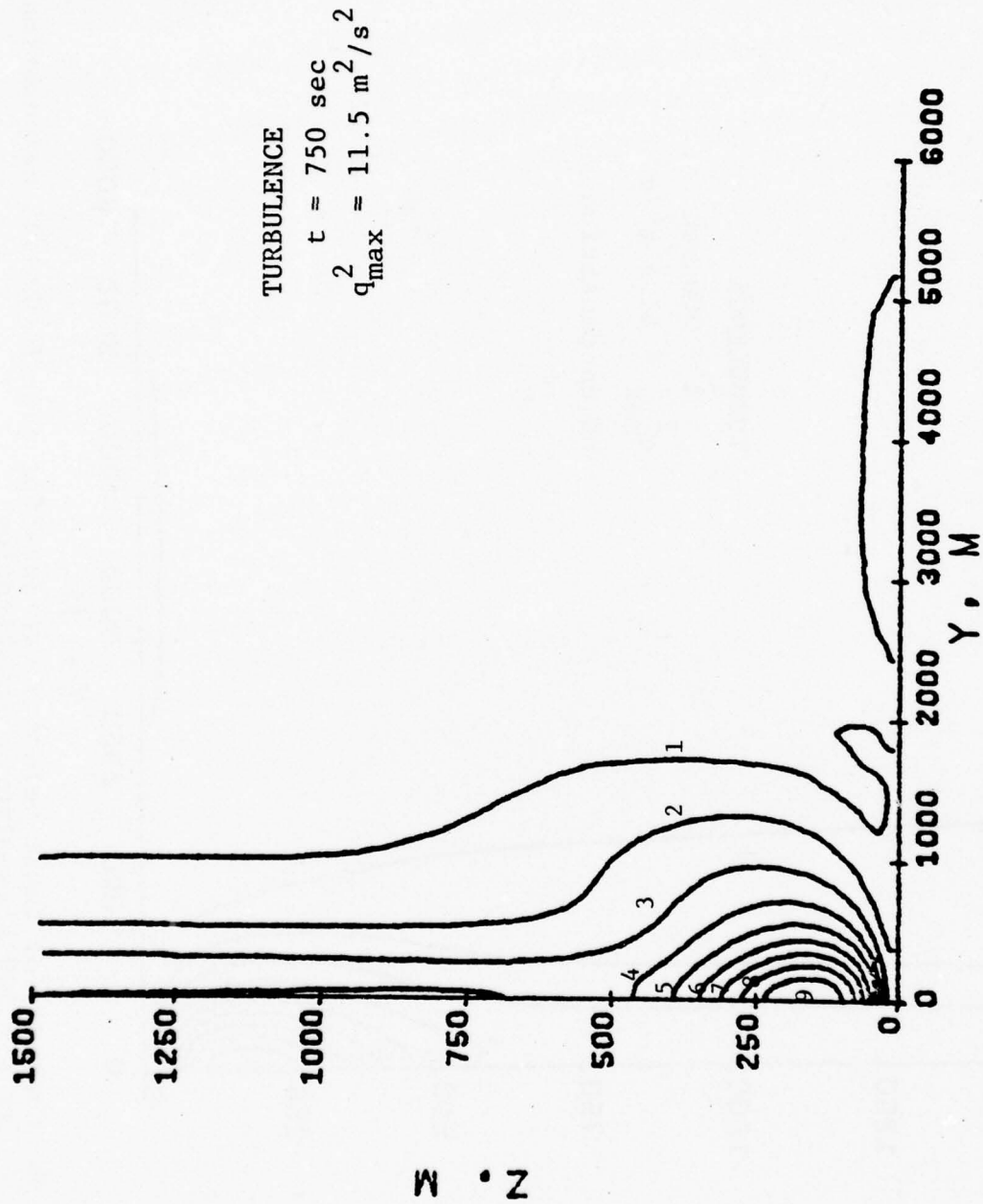


Figure 3.9c Contours of total velocity variance for case B without evaporation at $t = 350$ secs after initialization.

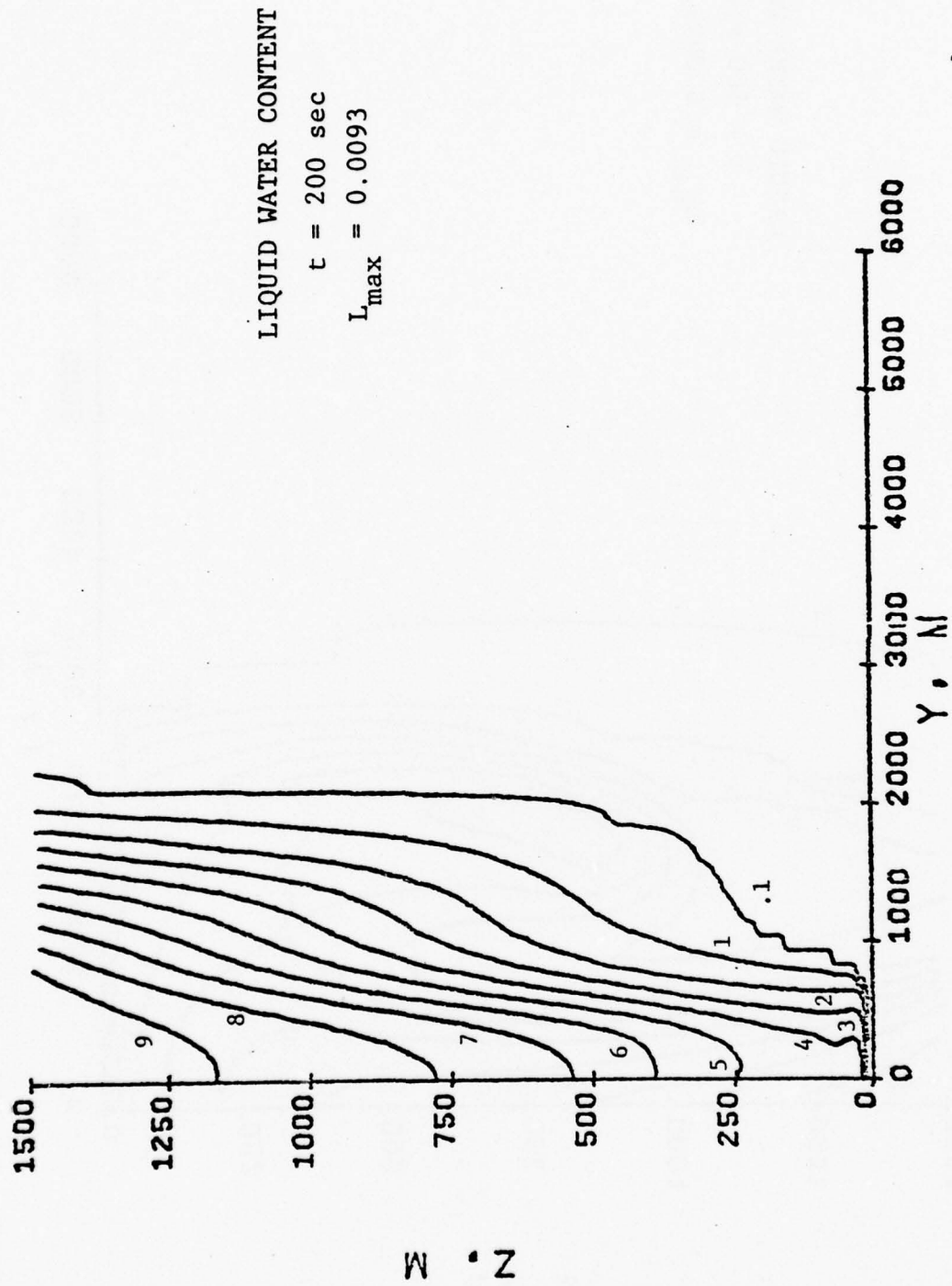


Figure 3.10a Liquid water content contours for case A with evaporation at $t = 200$ secs after initiation.

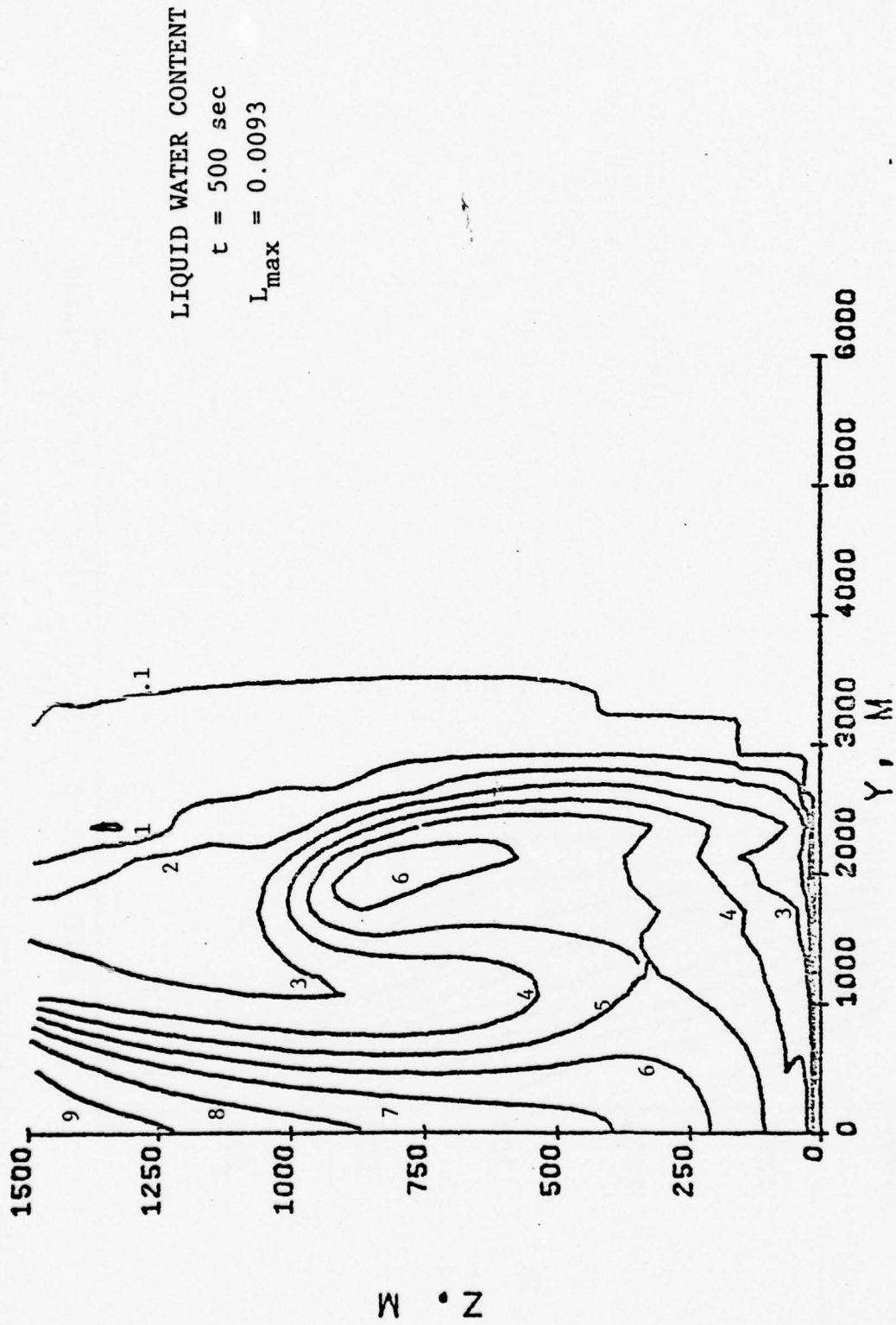


Figure 3.10b Liquid water content contours for case A with evaporation at $t = 500$ secs after initialization.

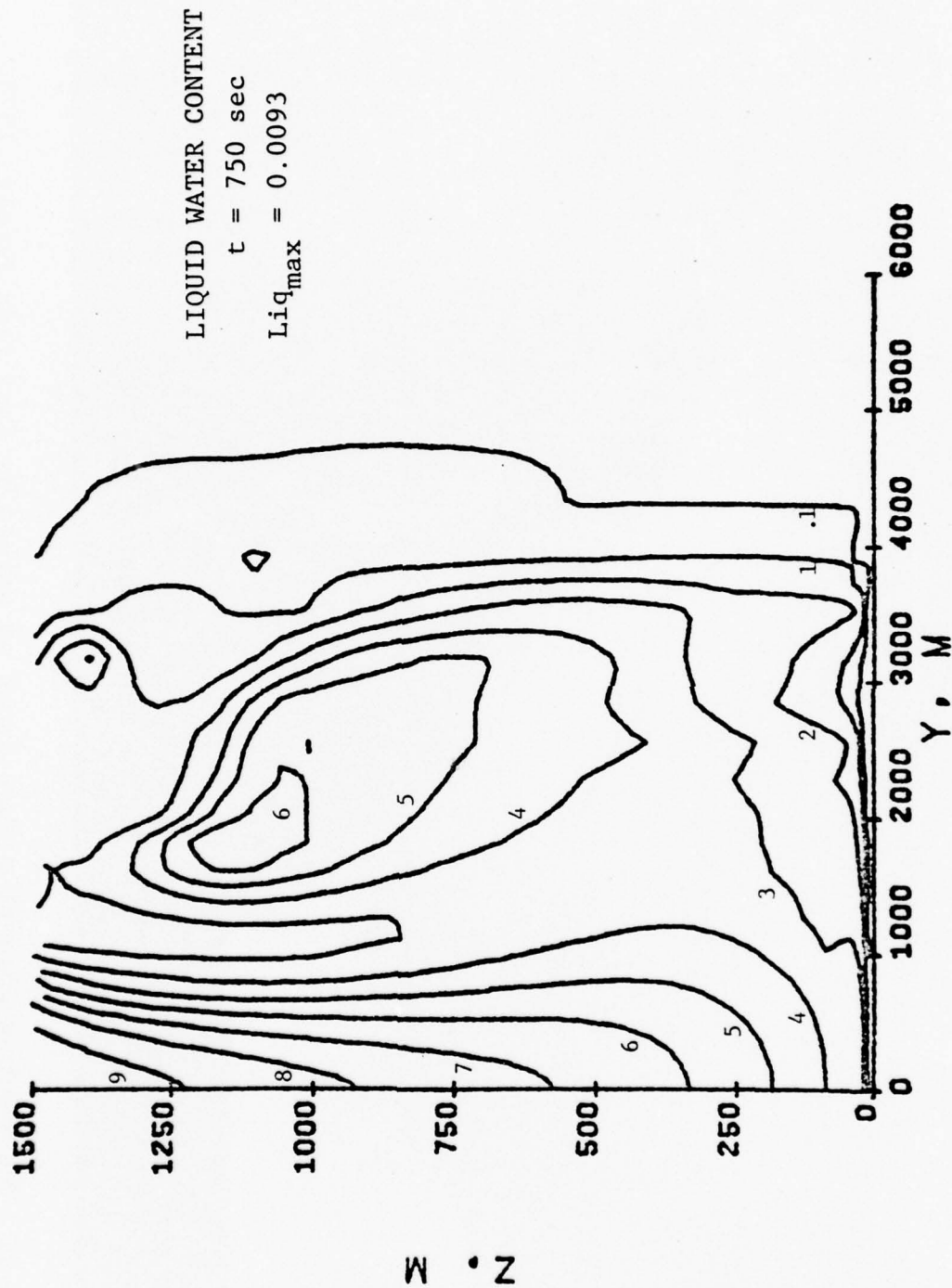


Figure 3.10c Liquid water content contours for case A with evaporation at $t = 750$ secs after initialization.



Figure 3.11 The leading edge of a gust front as marked by dust from Turner, 1973.

BEST AVAILABLE COPY



Figure 3.12 Model simulation of the leading edge of a gust front when visualized in terms of temperature defect intensity.

4. CONCLUSIONS AND RECOMMENDATIONS

We believe that substantial progress has been made during the last year toward the goal of providing the Navy with the capability of making detailed predictions of the low-level distributions of pertinent atmospheric variables. Although verification tests have not been adequate to provide detailed assessment of the accuracy of our model, the one-dimensional version of our model should be capable of making useful predictions over regions with strong spatial homogeneity. A copy of this program has been delivered to the Naval Environmental Prediction Research Facility.

During the current year, we have significantly extended the two-dimensional, unsteady model. However, additional work is required to make these features completely operational when all the other features of the program, such as density gradients, condensation, terrain variation and thermal radiation are being computed simultaneously. This consolidation of the model's capability will provide a unique research tool for simulating much of the physics which occurs in the atmospheric boundary layer in the vicinity of coast lines.

As demonstrated in Appendix A, we have been able to use our one-dimensional, unsteady model to simulate, quite realistically, many of the features observed in the evolution of coastal fog and low-level stratus. More features should be amenable to simulation with the extended two-dimensional version of our model. Ideally, by calculating model predictions for situations that have been carefully observed, it should be possible to both make model verification comparisons and suggest causal relationships between different physical features to aid in parameterization for larger scale models. We will continue to search for available data to be used for our model comparisons.

Under certain conditions, the large eddies in the marine boundary layer become highly organized. Such boundary-layer roll vortices have been the subject of several experimental measurement programs (e.g., LeMone, 1976). By fixing our computational coordinate system with respect to the axis of an individual roll vortex, we should be able to compute the large eddy velocities as a part of the ensemble-averaged mean velocity. The numerical results may then be compared with the aircraft observations published by LeMone. In addition to being a basic flow structure of interest in its own right, such a comparison between model results and field observations would provide a further verification test of the model. The only model development required for this calculation is the application of periodic boundary conditions to the two-dimensional, unsteady program.

We propose to continue our investigation of the structure and movements of sharp horizontal temperature gradients, i.e., fronts, in marine boundary layer. By combining an analytical investigation of the relationships between the basic parameters

in a highly simplified model of the front as an internal wave, with detailed calculations using our sophisticated two-dimensional numerical model, we should be able to increase our understanding of this phenomenon. We will look for frontal situations with characteristics which may be anticipated to have an impact on naval operations.

Our program's usefulness can be increased by decreasing the computational time required. We have taken several steps in this direction over the last year by changing the structure of the numerical convective operator, by adding a quasi-coupling between some of the equations, and by structuring the surface boundary conditions to permit larger grid spacing. We expect to continue this process of improving the program's efficiency. We are particularly interested in achieving a sufficiently significant decrease in computational requirements to make the extension to a three-dimensional model attractive.

The current analysis of aerosol transport lays the foundation for incorporating more cloud physics into our model. We would like to pursue this far enough to at least include a simple model of precipitation in our program. This will require carrying additional information about particle size and growth.

REFERENCES

1. Chamberlin, A.C. 1967. "Transport of Lycopodium spores and other small particles to rough surfaces," Proc. Roy. Soc. A 296, 45-70.
2. Donaldson, Coleman duP. 1973. "Construction of a dynamic model on the production of atmospheric turbulence and the dispersal of atmospheric pollutants. Workshop on Micrometeorology, 313-392.
3. Friedlander, S.K. 1977. Smoke, Dust and Haze. John Wiley & Sons, Toronto.
4. LeMone, M.A. 1976. "Modulation of turbulence energy by longitudinal rolls in an unstable planetary boundary layer," J. Atmos. Sci. 33, 1308-1320.
5. Lewellen, W.S. 1977 "Use of invariant modeling," Handbook of Turbulence, edited by W. Frost, Plenum Press, 237-290.
6. Lewlilen, W.S., Oliver, D.A., Teske, M.E., and Williamson, G.G. 1976. "Status report on a low-level atmospheric turbulence model for marine environment," A.R.A.P. Report No. 289.
7. Lewellen, W.S., and Teske, M.E. 1973. "Predictions of the Monin-Obukhov similarity functions from an invariant model of turbulence," J. Atmos. Sci. 30, 1340-1345.
8. Lewellen, W.S., and Teske, M.E. 1975. "Development of a low-level atmospheric turbulence model for marine environments," A.R.A.P. Report No. 255.
9. Lewellen, W.S., and Teske, M.E. 1976a. "Second-order closure modeling of diffusion in the atmospheric boundary layer. Boundary Layer Meteor. 10, 69-90.
10. Lewellen, W.S., and Teske, M.E. 1976b. "A second-order closure model of turbulent transport in the coastal planetary boundary layer," Presented at Conference on Coastal Meteorology, Virginia Beach, VA, Sept. 21-23, 1976.
11. Lewellen, W.S., Teske, M.E., and Donaldson, CduP. 1974. "Turbulence model of diurnal variations in the planetary boundary layer," Proc. 1974 Heat Transfer and Fluid Mechanics Institute (L.R. David & R E. Wilson, eds.), Stanford University press, 301-319.
12. Lewellen, W.S., Teske, M.E., and Donaldson, CduP. 1976. "Examples of variable density flows computed by a second-order closure description of turbulence," AIAA Journal, 14, 382-387.

13. Marble, F.E. 1970. "Dynamics of dusty gases," Annual Review of Fluid Mechanics, Vol. 2, 397-446.
14. Pennell, W.T., and LeMone, M.A. 1974. "An experimental study of turbulence structure in the fair-weather trade wind boundary layer," J. Atmos. Sci. 31, 1308-1323.
15. Roache, P.J. 1972. Computational Fluid Dynamics. Hermosa Publishers, Albuquerque.
16. Sommeria, G. 1976. "Three-dimensional simulation of turbulent processes in an undisturbed trade wind boundary layer," J. Atmos. Sci. 33, 216-241.
17. Sommeria, G., and Deardorff, J.W. 1977. "Subgrid-scale condensation in models of nonprecipitating clouds," J. Atmos. Sci., 34, 344-355.
18. Tennekes, H., and Lumley, J.L. 1972. A First Course in Turbulence, The MIT Press, Cambridge.
19. Teske, M.E., and Lewellen, W.S. 1977. "Turbulent transport model of a thunderstorm gust front," 10th Conf. on Severe Local Storms, Oct. 18-21, 1977, Omaha, Neb.
20. Turner, J.S. 1973. Buoyancy Effects in Fluids, Cambridge University Press, Great Britain.

APPENDIX A

THE INTERACTION BETWEEN TURBULENT AND
RADIATIVE TRANSPORT
IN THE DEVELOPMENT OF FOG
AND LOW-LEVEL STRATUS*

by

D. A. Oliver, W. S. Lewellen, and G. G. Williamson

Aeronautical Research Associates
of Princeton, Inc.

June 1977

ABSTRACT

A turbulent-radiative description of the low level atmosphere incorporating stratus cloud and fog is developed based on the methodology of second-order closure. Existence criteria for surface layer fog are developed on the basis of the turbulent description. Illustrative application is made to the formation and structure of several fog and cloud episodes including advective-radiative fog, subsidence capped stratus over the ocean, and surface fog resulting from the nocturnal lowering of stratus.

*To be published in the Journal of the Atmospheric Sciences, Feb. 1978.

1. Introduction

In this study we examine the mutual interaction of turbulence, radiation, and water condensation in the formation, structure, and evolution of the atmospheric boundary layer with fog or clouds. We formulate a turbulent-radiative theory of the atmospheric boundary layer based upon a second-order closure description of turbulence which includes the condensation, evaporation, and transport of water both as vapor and liquid. The methodology of second-order closure consists of extending the variables which describe the fluid beyond the mean velocity, humidity, and temperature fields to include the second-order turbulent correlations of these variables. This extended set of correlations is governed by an extended set of conservation laws obtained by taking exact second-order moments of the instantaneous Navier-Stokes system. Closure is obtained by modeling the unknown correlations which appear in the moment equations in terms of the describing field of second-order correlations (Donaldson, 1973; Mellor and Yamada, 1974; Lumley and Khajeh-Nouri, 1973; Wyngaard, et al., 1974).

The second-order closure model we apply has previously been used to obtain accurate prediction of the Monin-Obukhov similarity functions for the surface layer (Lewellen and Teske, 1973) as well as a detailed representation of the diurnal variation of the atmospheric boundary layer over land (Lewellen, Teske, and Donaldson, 1974), and the sea-breeze-land breeze

cycle in the coastal planetary boundary layer (Lewellen and Teske, 1976). A similar second-order closure model has been applied to the moist boundary layer (but neglecting the presence of condensed water and radiative transport) by Burk, 1977.

From such a turbulent-radiative theory, we obtain a description of the dynamics of a cloudy or foggy boundary layer. At the scale of the cloud itself we describe its internal dynamical and thermal structure including the distributions of turbulent heat and water fluxes and radiative heating and cooling. Of particular interest at this scale is the detailed behavior of cloud top mixing in which radiative cooling and turbulence production are strongly linked. We show that because of the unique radiative properties of the water molecule, stratus cloud and thick fog layer tops are not "burned away" by the sun's direct radiation; rather the tops of such clouds and fog are evaporated away by turbulent transfer of solar energy captured in the cloud or fog interior.

At the scale of the overall boundary layer, we describe the dynamics of formation and dissipation of cloud and fog events subject to diurnal or mesoscale boundary and initial conditions. In particular, we formulate in some detail the conditions for existence of surface fog in a turbulent surface layer as well as the conditions for diurnal lowering of stratus to the surface.

At present we carry out this program of description and illustration with a one-dimensional unsteady and two-dimensional steady state version of turbulent-radiative theory. We thus

restrict attention to layer fog and stratus cloud. We expect such a turbulent-radiative theory based upon second-order closure to be instructive in the development and evaluation of simple heat and moisture exchange models between the surface and the general circulation (Lilly, 1968; Schubert, 1976; Randall, 1976). Such a theory should also be complementary to alternative approaches to detailed models of atmospheric turbulence employing sub-grid turbulence modeling (Sommeria, 1976).

In Parts 2 and 3 we formulate the theoretical model. We then illustrate its descriptive and predictive power in application to surface fog existence criteria and the structure of fog in the turbulent surface layer (Part 4), advective-radiative fog (Part 5), stratus cloud in the boundary layer (Part 6), and diurnal lowering of stratus to the surface as fog (Part 7).

2. Turbulent description of the atmospheric boundary layer

The moist planetary boundary layer can be described by its instantaneous velocity field u_i , potential temperature θ_s , total water mixing ratio q , and pressure p . These variables are quite accurately governed by the instantaneous Navier-Stokes equations in the Boussinesq approximation in a coordinate system $x_i = x_i(x, y, z)$ rotating with angular velocity Ω_j in time t :

$$\frac{\partial u_i}{\partial x_i} = 0 \quad (1a)$$

$$\frac{Du_i}{Dt} + \frac{1}{\rho} \frac{\partial p}{\partial x_i} = g_i \frac{\theta_v}{T_r} - 2\epsilon_{ijk} \Omega_j u_k \quad (1b)$$

$$\frac{D\theta_s}{Dt} = S \quad (1c)$$

$$\frac{Dq}{Dt} = 0 \quad (1d)$$

The gravitational acceleration is g_i and T_r , ρ are the reference temperature and density of the undisturbed atmosphere about which the Boussinesq approximation is made. The source term for radiant energy is S and may be expressed in terms of the total (direct solar and terrestrial) radiant heat flux vector q_i^{rad} as

$$S = - \frac{1}{\rho C_p} \frac{\partial q_i^{\text{rad}}}{\partial x_i} \quad (2)$$

Our description is restricted to nonprecipitating boundary layers so that there is no source term for moisture in Eq.

(1d). Consistent with this approximation, we will restrict this analysis to equilibrium condensation so that the vapor mixing ratio q_v and the liquid mixing ratio q_l are given by

$$q_v = q + (q_s - q)H(q - q_s) \quad (3a)$$

$$q_l = (q - q_s)H(q - q_s) \quad (3b)$$

where $H(\cdot)$ is the Heaviside function and $q_s(p, T)$ is the saturation mixing ratio.

The conserved potential temperature θ_s is related to the absolute temperature T as

$$\theta_s = T - T_r + \Gamma z + \frac{L}{C_p} q_v \quad (4)$$

where $\Gamma = g/C_p$ is the adiabatic lapse rate, L is the latent heat of vaporization, and z is the coordinate along which the gravitational vector g_1 lies. The virtual potential temperature θ_v is the active temperature in the buoyancy force defined as

$$\theta_v = T - T_r + \Gamma z + (0.61q_v - q_l)T_r \quad (5)$$

The potential temperatures θ_s and θ_v are necessarily equal in a water-free atmosphere but not in a water-laden boundary layer. If all water is in vapor form so that $q_v = q$ then the energy equations expressed either in terms of θ_v or θ_s

are identical. With condensed liquid present this is not so and θ_v and θ_s are related by

$$\begin{aligned}\frac{D\theta_s}{Dt} &= S \\ \frac{D\theta_v}{Dt} &= S + \left(\frac{L}{C_p T_r} - 1.61 \right) T_r \frac{Dq_\ell}{Dt}\end{aligned}$$

showing that the condensation of water acts as a source of virtual energy but not of potential energy. Because of the extensive role θ_v will play in the turbulent moment equations, we represent the energy equation, Eq. (1c), in terms of θ_v and eliminate θ_s from the system:

$$\frac{D\theta_v}{Dt} = \kappa_s S + \kappa_g \Gamma w \quad (6)$$

The vertical velocity is w and κ_s and κ_g are coefficients generated from the vapor saturation function

$$\kappa_s = \begin{pmatrix} 1 \\ \mu \\ \tilde{\mu} \end{pmatrix} \quad \kappa_g = \begin{pmatrix} 0 \\ \alpha - \frac{\mu}{\tilde{\mu}} \tilde{\alpha} \end{pmatrix} \quad (7)$$

The parameters μ , $\tilde{\mu}$, α , $\tilde{\alpha}$ are

$$\begin{aligned}\mu &= 1 + 1.61 q_s \beta_T & \alpha &= 1 + 1.61 \frac{C_p}{R_m} \\ \tilde{\mu} &= 1 + \frac{R_v}{C_p} q_s \beta_T^2 & \tilde{\alpha} &= 1 + \frac{R_v}{R_m} q_s \beta_T\end{aligned} \quad (8)$$

The upper values of κ_s , κ_g apply away from saturation conditions; lower values apply at saturation. R_v and R_m are gas constants for water vapor and air respectively. The parameter β_T is the logarithmic derivative of the saturation mixing ratio with respect to temperature

$$\beta_T = \left(\frac{\partial \ln q_s}{\partial \ln T} \right)_p \quad (9)$$

If the saturation function is given in the Clapeyron representation

$$q_s(p, T) = q_{s\infty} \left(\frac{p_\infty}{p} \right) \exp \left[\frac{L}{R_v} \left(\frac{1}{T_\infty} - \frac{1}{T} \right) \right] \quad (10)$$

where $q_{s\infty}$, p_∞ , T_∞ are reference values at some state then β_T is given by

$$\beta_T = \left(\frac{L}{R_v T} \right) \quad (11)$$

Equations (1a,b,d) and (4) form the basis of the turbulent description. We now consider their turbulent ensemble average. Denote the ensemble average with an overbar and let a prime denote the deviation from the average. The mean fluid equations for \bar{u}_i , $\bar{\theta}_v$, \bar{q} , are then

$$\frac{\partial \bar{u}_i}{\partial x_i} = 0 \quad (12a)$$

$$\frac{D\bar{u}_i}{Dt} + \frac{1}{\rho} \frac{\partial \bar{p}}{\partial x_i} = - \frac{\partial}{\partial x_j} (\overline{u_i' u_j'}) + \frac{g_i}{T_r} \bar{\theta}_v - 2\epsilon_{ijk} \Omega_j \bar{u}_k \quad (12b)$$

$$\frac{D\bar{\theta}_v}{Dt} = - \frac{\partial}{\partial x_j} (\overline{u_j' \theta_v'}) + \kappa_s \bar{S} + \kappa_g \Gamma \bar{w} \quad (12c)$$

$$\frac{D\bar{q}}{Dt} = - \frac{\partial}{\partial x_j} (\overline{u_j' q'}) \quad (12d)$$

In Eqs. (12) it is understood that the substantial derivative $\frac{D}{Dt}$ is based upon the mean velocity \bar{u}_i . In the ensemble averaging, we neglect fluctuations in the coefficients κ_s , κ_g .

We now augment the fundamental set of mean flow variables to include the following second-order correlations:

$$\begin{array}{ll}
 \overline{u_i' u_j'} & \text{(Reynolds stresses)} \\
 \overline{u_i' \theta_v'} & \text{(heat flux)} \\
 \overline{u_i' q'} & \text{(moisture flux)} \\
 \left. \begin{array}{l} \overline{q' \theta_v'} \\ \overline{\theta_v'^2} \\ \overline{q'^2} \end{array} \right\} & \text{(temperature-humidity} \\
 & \text{correlations and} \\
 & \text{variances)}
 \end{array}$$

These second-order correlations are governed by an exact set of moment equations generated from the instantaneous Navier-Stokes system (1a-d) (Donaldson, 1973; Lewellen, 1977).

Unknown second-order correlations and third-order correlations which appear in the exact moment equations are modeled in terms of second-order correlations leading to the following closed system (Lewellen and Teske, 1975)

$$\begin{aligned}
 \frac{D}{Dt} \overline{u_i' u_j'} = & -\overline{u_i' u_k'} \frac{\partial \bar{u}_j}{\partial x_k} - \overline{u_j' u_k'} \frac{\partial \bar{u}_i}{\partial x_k} + \frac{\varepsilon_i}{T_r} \overline{u_j' \theta_v'} + \frac{\varepsilon_j}{T_r} \overline{u_i' \theta_v'} \\
 & - 2\varepsilon_{ikl} \Omega_k \overline{u_l' u_j'} - 2\varepsilon_{jlk} \Omega_l \overline{u_k' u_i'} \\
 & + 0.3 \frac{\partial}{\partial x_k} \left(q \Lambda \frac{\partial \overline{u_i' u_j'}}{\partial x_k} \right) - \frac{q}{\Lambda} (\overline{u_i' u_j'} - \delta_{ij} q^2/3) \\
 & - \delta_{ij} \frac{q^3}{12\Lambda}
 \end{aligned} \tag{13a}$$

$$\begin{aligned}
\frac{D}{Dt} \overline{u_1' \theta_v'} &= -\overline{u_1' u_j'} \frac{\partial \bar{\theta}_v}{\partial x_j} - \overline{u_j' \theta_v'} \frac{\partial \bar{u}_1}{\partial x_j} + \frac{g_1}{T_r} \overline{\theta_v'^2} \\
&\quad - 2\epsilon_{1jk} \Omega_j \overline{u_k' \theta_v'} + 0.3 \frac{\partial}{\partial x_j} \left(q\Lambda \frac{\partial \overline{u_1' \theta_v'}}{\partial x_j} \right) \\
&\quad - 0.75 \frac{q}{\Lambda} \overline{u_1' \theta_v'} + \kappa_g \Gamma \overline{u_1' w'}
\end{aligned} \tag{13b}$$

$$\begin{aligned}
\frac{D}{Dt} \overline{u_1' q'} &= -\overline{u_1' u_j'} \frac{\partial \bar{q}}{\partial x_j} - \overline{u_j' q'} \frac{\partial \bar{u}_1}{\partial x_j} + \frac{g_1}{T_r} \overline{q' \theta_v'} \\
&\quad - 2\epsilon_{1jk} \Omega_j \overline{u_k' q'} + 0.3 \frac{\partial}{\partial x_j} \left(q\Lambda \frac{\partial \overline{u_1' q'}}{\partial x_j} \right) \\
&\quad - 0.75 \frac{q}{\Lambda} \overline{u_1' q'}
\end{aligned} \tag{13c}$$

$$\begin{aligned}
\frac{D}{Dt} \overline{q' \theta_v'} &= -\overline{u_j' q'} \left(\frac{\partial \bar{\theta}_v}{\partial x_j} - \kappa_g \Gamma \delta_{1j} \frac{g_1}{|g|} \right) - \overline{u_j' \theta_v'} \frac{\partial \bar{q}}{\partial x_j} \\
&\quad + 0.3 \frac{\partial}{\partial x_j} \left(q\Lambda \frac{\partial \overline{q' \theta_v'}}{\partial x_j} \right) - 0.45 \frac{q}{\Lambda} \overline{q' \theta_v'}
\end{aligned} \tag{13d}$$

$$\begin{aligned}
\frac{D}{Dt} \overline{\theta_v'^2} &= -2\overline{u_j' \theta_v'} \frac{\partial \bar{\theta}_v}{\partial x_j} + 0.3 \frac{\partial}{\partial x_j} \left(q\Lambda \frac{\partial \overline{\theta_v'^2}}{\partial x_j} \right) \\
&\quad - 0.45 \frac{q}{\Lambda} \overline{\theta_v'^2} + 2\kappa_g \Gamma \overline{w' \theta_v'}
\end{aligned} \tag{13e}$$

$$\begin{aligned}
\frac{D}{Dt} \overline{q'^2} &= -2\overline{u_j' q'} \frac{\partial \bar{q}}{\partial x_j} + 0.3 \frac{\partial}{\partial x_j} \left(q\Lambda \frac{\partial \overline{q'^2}}{\partial x_j} \right) \\
&\quad - 0.45 \frac{q}{\Lambda} \overline{q'^2}
\end{aligned} \tag{13f}$$

In the development of Eqs. (13) correlations of the type $\overline{u_1' u_1'}$, $\overline{u_1' \theta_v'}$, and $\overline{u_1' q'}$ appear. These radiative correlations arise mainly because of fluctuations in the radiation absorption coefficient for water droplets which in turn arise

because of the fluctuations in q_ℓ . We observe that these correlations may modify the coefficients of the turbulent decay terms in Eqs. (13b,d, and e); but their structure is not likely to be modified. In the present calculation, we do not modify the coefficients of the model in Eqs. (13) to account for possible differences in radiative and molecular diffusion in small eddy destruction, since such effects require separate empirical confirmation and we do not expect the modifications to be large.

The variable q appearing in all correlation equations is the rms turbulence velocity. We note that each of the correlation Eqs. (13) is a balance equation involving production/destruction, diffusion, and turbulent decay. Three distinct production/destruction mechanisms are operative in the planetary atmosphere corresponding to the first terms on the right-hand side of the correlation equations. These three mechanisms are mean variable gradients, buoyancy, and rotation (Coriolis forces).

Central to all turbulent decay and diffusion processes in the correlation equations is the turbulent scale Λ . This scale function must also be determined to complete closure. The form of the scale equation is similar whether one begins with the two point velocity correlation to define an integral scale, the dissipation function $\epsilon = q^3/8\Lambda$, or the vorticity function q/Λ . In all cases the coefficients of the individual terms must be determined empirically. The form of the scale equation used in the present work is (Lewellen, 1977)

$$\begin{aligned} \frac{D\Lambda}{Dt} = & 0.35 \frac{\Lambda}{q^2} \overline{u_i' u_j'} \frac{\partial \bar{u}_i}{\partial x_j} + 0.75q + 0.3 \frac{\partial}{\partial x_j} \left(q\Lambda \frac{\partial \Lambda}{\partial x_j} \right) \\ & - \frac{0.375}{q} \left(\frac{\partial q\Lambda}{\partial x_j} \right)^2 + 0.8 \frac{\Lambda}{q^2} \frac{g_i}{T_r} \overline{u_i' \theta_v'} \end{aligned} \quad (14)$$

The correlations $\overline{q_s'^2}$, $\overline{q_s' q_v'}$, and $\overline{q_s' q'}$ (which do not appear explicitly in the moment equations) are also useful. For small fluctuations $\left(\frac{q_s'}{\bar{q}_s} \right) \ll 1$ these may be represented in terms of the basic set as

$$\overline{q_s'^2} = \beta_T^2 \bar{q}_s^2 \left[\frac{\gamma_\theta^2}{T_r^2} \overline{\theta_v'^2} + 2 \frac{\gamma_\theta}{T_r} \gamma_q \overline{q' \theta_v'} + \gamma_q^2 \overline{q'^2} \right] \quad (15)$$

$$\overline{q_s' \theta_v'} = \beta_T \bar{q}_s \left[\frac{\gamma_\theta}{T_r} \overline{\theta_v'^2} + \gamma_q \overline{q' \theta_v'} \right] \quad (16)$$

$$\overline{q_s' q'} = \beta_T \bar{q}_s \left[\frac{\gamma_\theta}{T_r} \overline{q' \theta_v'} + \gamma_q \overline{q'^2} \right] \quad (17)$$

where

$$\gamma_\theta = \begin{pmatrix} 1 \\ \frac{1}{\mu} \end{pmatrix} \quad \gamma_q = \begin{pmatrix} -.61 \\ \frac{1}{\mu} \end{pmatrix} \quad (18)$$

and upper and lower values apply to nonsaturated and saturated cases, respectively.

We now turn to the specification of the ensemble average liquid water content which is given by

$$\bar{q}_\ell = \overline{(q - q_s)H(q - q_s)} \quad (19)$$

This average is not equal to the simple form

$$\bar{q}_\ell = (\bar{q} - \bar{q}_s)H(\bar{q} - \bar{q}_s) \quad (20)$$

This is because the liquid water content q_ℓ is a physically positive definite quantity. It may be seen that the contributions

made when $\bar{q}+q' > \bar{q}_s+q'_s$ cannot be balanced by contributions made when $\bar{q}+q' < \bar{q}_s+q'_s$. Thus, the form Eq. (20) is correct only when the flow is sufficiently saturated that no local unsaturated region is contained within an eddy.

The exact specification of the average liquid water ratio may be calculated by taking the moment implied by Eq. (19) over the joint probability distribution function $f(q, q_s)$ for q and q_s . Since the statistical detail of second-order closure is limited to second-order moments, the distribution function $f(q, q_s)$ is not known or describable. Only the second moments of f may be elements of the theory. The liquid water moment may be carried out by assuming the form of $f(q, q_s)$ e.g., a joint Gaussian distribution about the mean (Sommeria and Deardorff, 1977; Mellor, 1977), however it is possible that quite arbitrary artificiality may be injected into the theory at significant formal expense by such assumed distribution functions. We adopt an equally arbitrary but much simpler procedure for the determination of q_ℓ which requires assumptions about the nature of the averages rather than the nature of the distribution function.

To account for the fact that eddies may contain both saturated and unsaturated fluid, we define a transition regime which separates completely unsaturated and completely saturated regimes. This occurs when the majority of the fluctuations in q and q_s give $q-q_s$ and $\bar{q}-\bar{q}_s$ opposite senses. This transition regime may be defined as occurring whenever

$$\Delta \geq |\bar{q} - \bar{q}_s| \quad (21)$$

where Δ is a characteristic measure of the size of fluctuation which may contain both saturated and unsaturated eddies:

$$\Delta = \sqrt{q'^2} + \sqrt{q'_s{}^2} \quad (22)$$

We then approximate the average liquid water content as

$$q_l = \begin{cases} \bar{q} - \bar{q}_s & \Delta < |\bar{q} - \bar{q}_s| \\ \frac{1}{2}[\bar{q} - \bar{q}_s + \Delta] & \Delta \geq |\bar{q} - \bar{q}_s| \end{cases} \quad (23)$$

Equations (23) have the correct limits of zero and $\bar{q} - \bar{q}_s$ when equality holds in Eq. (21). Further, if q' and q'_s are each symmetrically distributed about their means, Eq. (23) indicates that when $\bar{q} = \bar{q}_s$ and q' (or q'_s) vanishes, only negative q'_s (or positive q') will lead to condensation.

The coefficients κ_s , κ_g also require modification in the transition regime. We structure these coefficients in the transition regime to vary linearly between their saturated and unsaturated values in direct proportion to the liquid water content. Thus, in the transition regime defined by the inequality (21)

$$\kappa_s = 1 + \left(\frac{\mu}{\bar{\mu}} - 1 \right) \frac{q_l}{\Delta} \quad (24)$$

$$\kappa_g = \left(\alpha - \frac{\mu}{\bar{\mu}} \tilde{\alpha} \right) \frac{q_l}{\Delta} \quad (25)$$

otherwise, κ_s and κ_g are given by Eqs. (7).

We now remark on boundary conditions appropriate to the system consisting of Eqs. (12) and (13). The boundary condition on the mean velocity at the surface is given in terms

of the effective aerodynamic roughness z_0 . Over water, the effective roughness height z_0 is given by Froude similarity scaling (Charnock, 1955). We use the Froude number based on u_* determined empirically by Wu (1969)

$$\frac{u_*}{\sqrt{gz_0}} \approx 8 \quad (26)$$

Surface boundary conditions are applied at a reference height $z = z_r$ which is greater than z_0 but sufficiently small that two conditions are satisfied. First the characteristic time of the dynamics of turbulence, Λ/q , is small enough so that the turbulent quantities are in a local equilibrium balance between production and decay and, second, that z_r falls well within the constant flux region where the turbulent flux of momentum, heat, or species remains constant with height. The boundary conditions applicable at z_r are that the gradients of mean flow variables are related to the surface fluxes

$$u_* = \sqrt{\overline{u'w'}} \Big|_0, \quad \theta_{v*} = \overline{w'\theta_v} \Big|_0 / u_*, \quad q_* = \overline{w'q'} \Big|_0 / u_*$$

through the Monin-Obukhov similarity functions (Lewellen and Teske, 1973):

$$\frac{\partial \bar{u}}{\partial z} = \frac{u_*}{kz} f_u(\zeta) \quad (27)$$

$$\frac{\partial \bar{\theta}_v}{\partial z} = \frac{\theta_{v*}}{kz} f_\theta(\zeta) \quad (28)$$

$$\frac{\partial \bar{q}}{\partial z} = \frac{q_*}{kz} f_q(\zeta) \quad (29)$$

In the above, k is the von Kàrmàn constant, L_m is the Monin-Obukhov length

$$L_m = - \frac{u_*^2 T_r}{kg\theta_{v*}} \quad (30)$$

and ζ is the height z nondimensionalized by The Monin-Obukhov length. The similarity functions f_u and f_θ have been determined empirically (Businger, et al., 1970) and theoretically (Lewellen and Teske, 1973; Mellor, 1973).

Over the ocean surface, values for H and θ_v are more likely to be known than the surface fluxes $\overline{w'q'}|_0$ and $\overline{w'\theta'_v}|_0$. In this case, Eqs. (27)-(29) are analytically integrated between z_r and z_0 and the surface values $\bar{\theta}_{v0}$, \bar{q}_0 applied.

At the upper boundary of the computational domain (which lies outside the boundary layer) we specify the lapse rate, geostrophic wind, and upper air water mixing ratio. All turbulence quantities are made to vanish at the upper boundary for stable atmospheres. Notice that the lapse rate specification allows the boundary temperature to be computed in the course of the dynamics of evolution of the boundary layer. This is particularly important because a diurnal radiative cooling/heating in general exists on the boundary as well as in the interior of the fluid.

Sample calculations using this system of equations and boundary conditions were reported earlier (Lewellen and

Teske, 1975) without including the influence of coupling to thermal radiation.

3. Radiant heat transfer description

We separate the direct solar (short wavelength) from the terrestrial (long wavelength) fields. Each of these fields is described in terms of the one-dimensional (z) upward and downward frequency and angular averaged radiation intensities F^+ , F^- . These intensities are governed by the upward and downward transport equations in integral form (Goody, 1964).

$$F^+(z) = [F^+(z_0) - \sigma(z_0)]\tau(z_0, z) + \sigma(z) - \int_{z_0}^z \tau(z', z) \frac{\partial \sigma}{\partial z'} dz' \quad (31)$$

$$F^-(z) = [F^-(h) - \sigma(h)]\tau(h, z) + \sigma(z) - \int_h^z \tau(z', z) \frac{\partial \sigma}{\partial z'} dz' \quad (32)$$

The boundary values at the surface $z = z_0$ and boundary layer "top" $z = h$ are $F^+(z_0)$ and $F^-(h)$ respectively. The radiative heat flux q_z^{rad} is given in terms of F^+ , F^- for either radiation field as

$$q_z^{\text{rad}} = F^+ - F^- \quad (33)$$

and the total radiant heat flux is the sum of the direct solar heat flux and the terrestrial heat flux.

The absorption, scattering, and emissive properties of the atmosphere are embedded in the source function $\sigma(z)$ and

the transmission function $\tau(z_1, z_2)$ between two levels z_1, z_2 . We neglect scattering in the present analysis. For direct solar radiation, emission is neglected and $\sigma(z) \equiv 0$. The boundary intensity $F^-(h)$ is set equal to the incident solar flux at h while $F^+(z_0)$ is determined by the surface reflectivity. The transmission function τ is modeled after that of Manabe and Strickler (1964) for water vapor and CO_2 . To account for liquid water, we include a transmission

$\tau_{\text{liq}}^S(z_1, z_2)$ as a factor in the total transmission τ of the form

$$\tau_{\text{liq}}^S(z_1, z_2) = \exp(-\beta \alpha^S m) \quad (34)$$

where m is the absorbing mass

$$m = \int_{z_1}^{z_2} \rho \xi dz \quad (35)$$

β is the diffusivity factor, and α^S is the specific absorption coefficient for direct solar radiation by water droplets. Feigel'son (1964) notes that solar absorption is not sensitive to droplet size for wavelengths less than 2μ . Integrating the spectral liquid water absorption coefficient tabulated by Feigel'son over the direct solar spectrum, we find

$$\alpha^S = 16 \text{ cm}^2/\text{gm}$$

For the terrestrial field, the source function σ is set equal to the integrated Planck function. For boundary conditions, we set $F^+(z_0)$ equal to the surface Planck function and $F^-(H)$ equal to the terrestrial downward flux emitted by the upper atmosphere. The transmission function for water vapor and CO_2 follows that of Feigel'son (1970) with the liquid water transmission included as a factor in the transmission τ of the form τ_{liq}^T

$$\tau_{liq}^T = \exp(-\beta \alpha^T m) \quad (36)$$

Here α^T is the averaged liquid water absorption coefficient for terrestrial radiation which depends strongly upon the droplet size distribution ranging in value from 200-1700 cm²/gm (Feigel'son, 1970) for spectra with average drop size radii ranging from 4.5 to 7 μ . We maintain the droplet size effect on radiative absorption as a parameter through α^T . Detailed inclusion of variation with droplet size requires prediction of the droplet number density within a cloud or fog as well as the liquid water content. Experimental evidence (Mack, et al., 1974) does not validate the simplifying assumption of uniform droplet density in space. Their observations indicate an order of magnitude variation in droplet number density through the boundary layer while mean droplet size varies by about 30 percent. A characteristic value of α^T for fog and stratus (mean drop radius approximately 6 μ) is 600 cm²/gm.

The significant difference between the absorption coefficients α^S and α^T is noteworthy. The absorption coefficients may be represented in terms of absorption lengths as

$$l_{rad}^T = \frac{1}{\alpha^T_{\rho < q_l}} \quad l_{rad}^S = \frac{1}{\alpha^S_{\rho < q_l}} \quad (37)$$

and exhibited in Table I for various (spatial) average liquid water contents $\langle q_l \rangle$. These values indicate that water is radiatively more active with the terrestrial spectrum than the direct solar spectrum for drops in the 4-10 μ range typical of fog and cloud. This sharp difference in radiative emission/absorption

in the terrestrial and solar spectrum will influence strongly the structure of cloud/fog cooling and the mechanism by which direct solar radiation evaporates away clouds or fog. We discuss these implications in Parts 6, 7, and 8.

Boundary conditions for terrestrial radiative transport are $F^- = 0$ at the upper boundary and $F^+ = B_0$ (B_0 is the black-body flux) at the surface. For direct solar radiation, F^- is specified as the incident downward solar flux at the upper boundary and $F^+ = \tau F^-$ at the surface where τ is the surface reflectance. The upper boundary for radiative transport is set at the atmospheric scale height and the average liquid water content and average water vapor content of the atmosphere contained within the radiative boundary and the fluid upper boundary is specified.

Table I.

Radiative absorption depths for fogs & stratus

$$l_{\text{rad}}^{s,T} = \frac{1}{\alpha_{s,T}^{<q_\ell>}}$$

	Average Liquid Water Contents $\langle q_\ell \rangle$ (g/kg)	Direct Solar Radiation l_{rad}^s (m)	Terrestrial Radiation l_{rad}^T (m)
Tenuous Fog	.025	20,000	600
	.1	5,500	167
	.2	2,700	83
	.4	1,350	41
Dense Stratus	.8	700	21
Tops	1.0	500	16

4. Fog in turbulent dominated surface layers

We now take up the first of several illustrative cases based upon the turbulent-radiative model we have just developed. We first consider the case in which turbulent transport dominates radiative transport in a surface fog. This represents a simple application of the turbulence theory and also allows a useful extension of the Monin-Obukhov analysis of the surface layer to include fog. The surface layer of the boundary layer is that region in which the turbulent fluxes of water, momentum, and heat may be taken as constant.

In the absence of radiation and for fog layers within the surface layer, the turbulent correlations for θ_s and q are identical to one another (although dissimilar to the correlation equations for u_1). The distributions of $q - q_0$ and $\theta_s - \theta_{s0}$ as well as their turbulent correlations must therefore be similar to one another and a function of z/L_m and z/z_0 only. Surface similarity leads to the formation of the following theorem

as essentially noted by G. I. Taylor (1917):

All fluid states in a surface layer in turbulent interaction must map onto a straight line in the $q-\theta_s$ plane which passes through the surface state (q_0, θ_{s0}) and has a slope determined by the surface humidity to heat flux ratio q_*/θ_{s*} .

Thus, surface layer similarity provides the basis for existence criteria of turbulent dominated surface fogs. In the $q-\theta_s$ plane of Figure 1, the surface state is denoted by "O" and the straight line OCDE represents the distribution of q and θ_s in the surface layer. The saturation function $q_s(p, T)$ may be represented in $q-\theta_s$ coordinates and is also shown in Figure 1. [Over the range of the surface layer ($z \ll T_r \Gamma^{-1}$) we neglect the variation of q_s with pressure.] The tangent to the saturation curve at the surface is denoted β_0 and is the thermodynamic derivative with respect to temperature in $q_s-\theta_s$ coordinates:

$$\beta_0 = \left(\frac{\partial q_s}{\partial \theta_s} \right)_p \quad (38)$$

The slope β_0 is simply related to the logarithmic temperature derivative β_T as

$$\beta_0 = \frac{q_s}{\mu} \beta_T \quad \begin{matrix} (39) \\ (39) \end{matrix}$$

The Clapeyron saturation function in $q_s-\theta_s$ coordinates becomes asymptotic to a straight line with slope $\beta_+ = \frac{q_0}{\theta_{s0}}$ for large θ_s .

For saturated conditions at the surface, any fluid trajectory will be a straight ray emanating from the surface point q_0 , θ_{s0} . Such a fluid trajectory entering the region below the line with slope β_0 will be a fog-free surface trajectory. This region is determined by the saturation conditions which determine β_0 and the turbulent surface layer conditions which determine θ_{s*} , q_* . Thus, surface fog is not possible for

$$\begin{aligned} \theta_{s*} < 0, \quad \frac{q_*}{\theta_{s*}} < \beta_0 \\ \theta_{s*} > 0, \quad \frac{q_*}{\theta_{s*}} > \beta_0 \end{aligned} \quad (40)$$

In the region between the lines with slopes β_+ and β_0 , surface fog exists adjacent to a cold surface and at a finite depth as shown by the typical surface trajectory O-C-D-E, the top of fog being at D and the maximum liquid content at C. Above the line with slope β_+ and the q axis, cold surface fog again exists, but it cannot be bounded within the surface layer.

In the region of $\theta_{s*} > 0$, warm surface fog exists. Such a fog may be bounded within the surface layer with a trajectory completely analogous to O-C-D-E for cold surface fog or it may be unbounded within the surface layer.

We observe that the existence or nonexistence of surface fog may be assessed directly in terms of the surface flux ratio q_*/θ_{s*} and that the critical value of q_*/θ_{s*} is equal to the tangent of the saturation curve at the surface:

$$\left(\frac{q_*}{\theta_{s*}}\right)_{\text{crit}} = \beta_0$$

Since most of our description is cast in $q-\theta_v$ variables, the relationship between $\left(\frac{q_*}{\theta_{s*}}\right)_{\text{crit}}$ and $\left(\frac{q_*}{\theta_{v*}}\right)_{\text{crit}}$ is useful.

From the definitions of Eqs. (3) and (4), the relationship between the fluxes, θ_{s*} and θ_{v*} may be written as

$$\theta_{v*} = \lambda_{\theta} \theta_{s*} - \lambda_q T_r q_* \quad (41)$$

where

$$\lambda_{\theta} = \begin{pmatrix} 1 \\ \frac{\mu}{\theta} \end{pmatrix} \quad \lambda_q = \begin{pmatrix} \frac{L}{C_p T_r} - .61 \\ 1 \end{pmatrix}$$

and lower values apply at saturation conditions. It thus follows that

$$\left(\frac{q_*}{\theta_{v*}}\right)_{\text{crit}} = \frac{\left(\frac{q_*}{\theta_{s*}}\right)_{\text{crit}}}{\lambda_{\theta} - \lambda_q T_r \left(\frac{q_*}{\theta_{s*}}\right)_{\text{crit}}} \quad (42)$$

For a cold surface fog ($\theta_{s*} < 0$) a large humidity flux and small heat flux promote fog formation. Thus dry

nearly adiabatic air over-running a cold water surface fogs easily. On the other hand, for a warm surface fog ($\theta_{s*} > 0$), the flux ratio must be smaller in magnitude than the critical value. Hence, cold air with high relative humidity over-running a warm surface will tend to fog. Further, for fluid trajectories with q_{**}/θ_{s*} in the fog regime the liquid water distribution is determined by the difference between the straight fluid trajectory OECD and the saturation curve. In particular, the maximum liquid water occurs at C and the total height of the fog layer occurs at D in Figure 1.

An illustrative family of fog distributions as given by integrating the similarity functions from Eqs. (28) and (29) is shown in Figure 2. Of particular interest, is the structure of the liquid water profiles in the fog layer for stable ($\zeta > 0$) and unstable ($\zeta < 0$) regimes. Stable fog layers have maximum q_l close to the surface and drop off sharply in liquid water content up to their maximum depth. Unstable layers are well-mixed and do not show a pronounced maximum except for very thin layers $\delta/L_m \ll 1$. Both families of fogs deepen and their maximum liquid water contents increase as their flux ratios q_{**}/θ_{s*} depart more from the critical value β_0 .

Let us now determine under what conditions the surface fog layer may be dominated by turbulent rather than radiative transport. The surface turbulent heat flux will be determined by the temperature gradient in the surface layer; but this gradient will also determine the maximum liquid water developed in the fog layer and hence the radiative emission from the layer.

EXISTENCE DIAGRAM FOR TURBULENT DOMINATED FOG

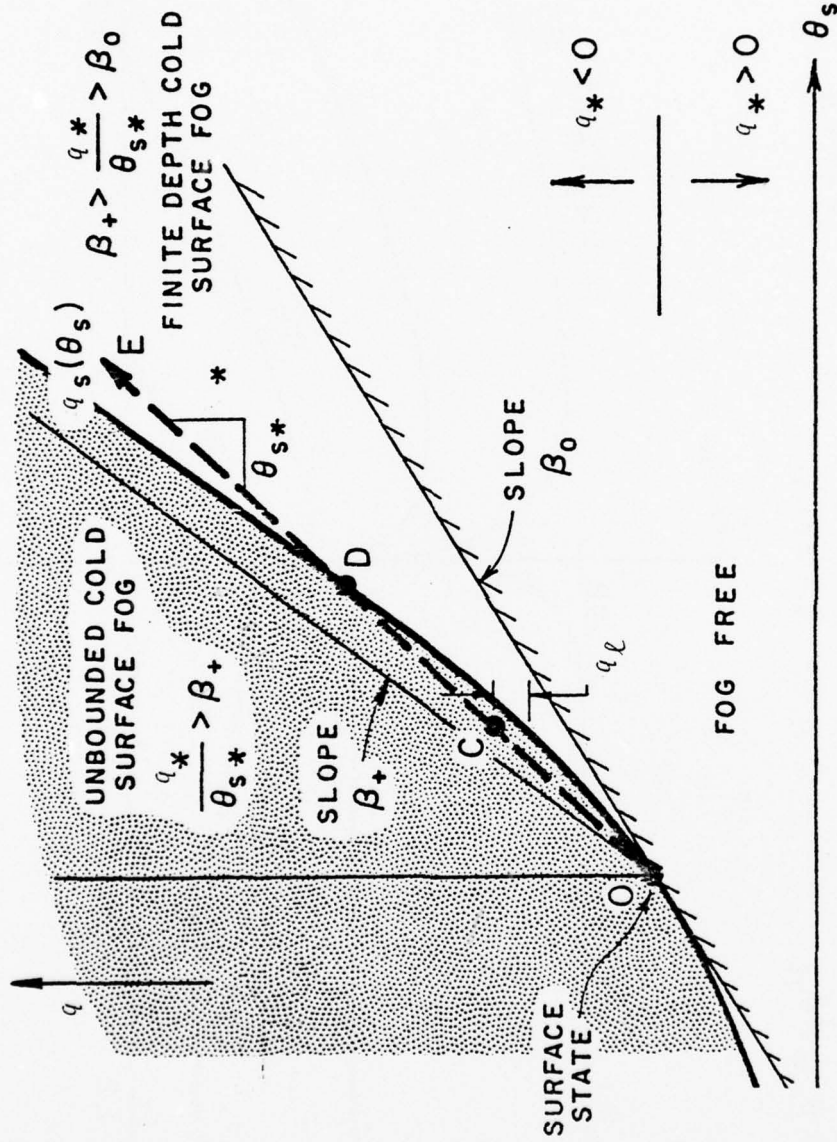


Figure 1. Existence diagram for turbulent dominated fog. Slope of the saturation function q_s in θ_s space, β_0 , determines the critical q_{s*}/θ_{s*} for surface layer distributions OCDE which will be foggy or fog-free. For a typical foggy layer, fog bank height is at D and maximum liquid water content at C.

LIQUID WATER DISTRIBUTION IN TURBULENT DOMINATED SURFACE LAYER

$$Q_* \equiv q_* / q_o$$

$$\Theta_{s*} \equiv \theta_{s*} / \theta_{so}$$

$$\left(\frac{Q_*}{\Theta_{s*}} \right)_{\text{CRIT}} = .78$$

$$L_m \equiv - \frac{u_*^2 T_o}{k \theta_{v*} g}$$

$$\zeta = z / L_m$$

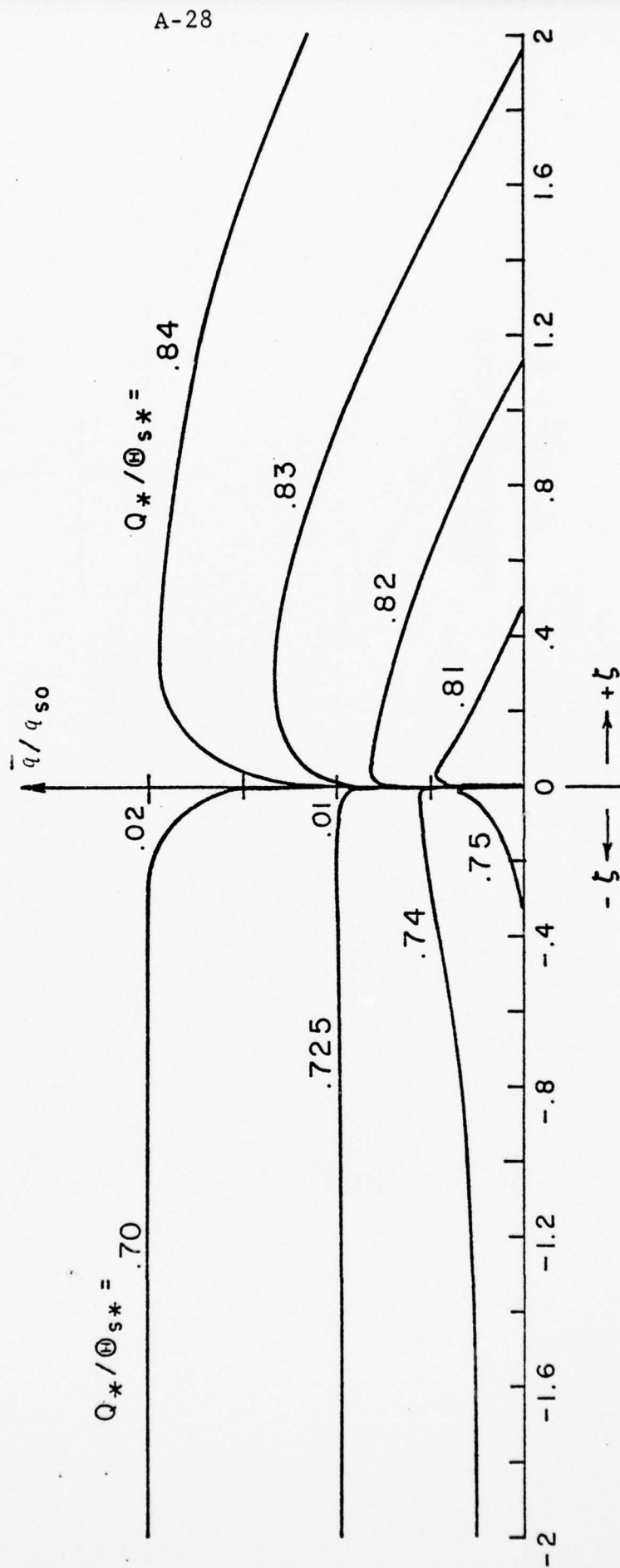


Figure 2. Illustrative liquid water distribution in stable ($\zeta > 0$) and unstable ($\zeta < 0$) surface layers.

For a radiatively thin fog layer ($\delta/\ell_{\text{rad}} \ll 1$) it is possible to estimate the radiative to turbulent heat flux for the fog layer as

$$\frac{q_{\text{rad}}}{q_{\text{turb}}} \approx \frac{4(\alpha^T \delta) \left(\frac{\partial T^4}{\partial p} \right) \left(\beta_0 - \frac{q_*}{\theta_{s*}} \right) \ln\left(\frac{\delta}{z_0}\right)}{u_*} \quad (43)$$

For the nominal condition of a 300°K surface, $\left(\beta_0 - \frac{q_*}{\theta_{s*}} \right) \approx .00002$, and $\alpha^T \approx 500 \text{ cm}^2/\text{gm}$,

$$\frac{q_{\text{rad}}}{q_{\text{turb}}} \approx \frac{\delta \ln(\delta/z_0)}{2000 u_*} \quad (44)$$

a result which depends only upon the strength of the wind and the depth of the fog. We see that it takes a relatively strong wind to make q^{rad} negligible compared to q^{turb} . For $\delta = 10 \text{ m}$, $z_0 = 10^{-3} \text{ m}$, a surface shear velocity of $u_* = 0.6 \text{ m/sec}$ (corresponding to a neutral wind at 10 meters of 14 m/sec) or greater is required to make q^{rad} less than 10 percent of q^{turb} . We conclude that radiation plays a significant role in most surface fogs of depths greater than a few meters.

BEST AVAILABLE COPY

5. The boundary layer with advective-radiative fog

We return to the full turbulent-radiative description [Eqs. (12), (13), (31), (32)] to illustrate the more general case of fog formation with both radiant and turbulent transport. We wish to utilize that description to predict the formation and structure of a commonly observed class of coastal fogs over water in which convection and radiation play equally important roles. Fogs are frequently found to occur in coastal regions subject to strong upwelling and non-uniform surface temperatures where winds bring the surface air from a region of cold water onto a region of warmer water (warm surface fog). Such fogs have been reported and documented by Mack, Pillie', and Kockmond (1973), and Leipper (1948). As an example of such advective-radiative fogs predicted by the present model we consider the following archetypal situation. A stable, steady boundary layer running over constant temperature water is incident on a region of linearly increasing surface temperature. As a result, an unstable mixed layer will be initiated and fog may form in the newly developing layer.

The incident profiles for this illustration are characterized by an $q_*/\theta_{v*} = .00015$ under conditions where

$$\left(\frac{q_*}{\theta_{v*}} \right)_{\text{crit}} = .0006 \quad .$$

The full profiles are determined by wind velocity of 2.8 m/sec and an absolute temperature difference of +1°C at $z = 20$ m elevation above the sea surface of $T = 13^\circ\text{C}$. Thus, the

incident flow is in the cold surface fog-free regime (Fig. 1). Direct solar radiation was suppressed (simulating nighttime conditions). The surface humidity was maintained at its saturation value at the surface temperature. Surface temperature linearly increases from the origin by 0.5°C in 3 km. The response of this layer is shown in Fig. 3. The combined action of increasing surface temperature and radiative cooling generates a fog layer which grows as the air is convected over the warmer water. Near the origin of the change in surface temperature ($x = 100$ m) a thin fog layer of about 18 m depth exists with maximum liquid water content just above the surface. At 1000 m the fog layer has grown to about 40 m and at 5000 m the layer is 100 m deep. At this depth the liquid water content has developed two relative maxima: one near the surface and one near the fog top. This is because the 100 m deep fog bank is no longer radiatively thin (Table I) and fog-top radiative cooling is beginning to dominate over surface radiative cooling. The early stages of a temperature inversion formation at the top of the fog bank are also in evidence.

After the change from stable to unstable conditions and the onset of radiative cooling, the local q_*/θ_{v*} shifts to a value of 0.0008. Such a flux ratio places a turbulent dominated layer in the warm surface fog-free regime of Figure 1. Fog nevertheless exists in such a layer because of the radiative cooling present. A convenient measure of the effect of radiation in a fog layer of thickness δ is an effective radiative flux q_*^{rad} defined as

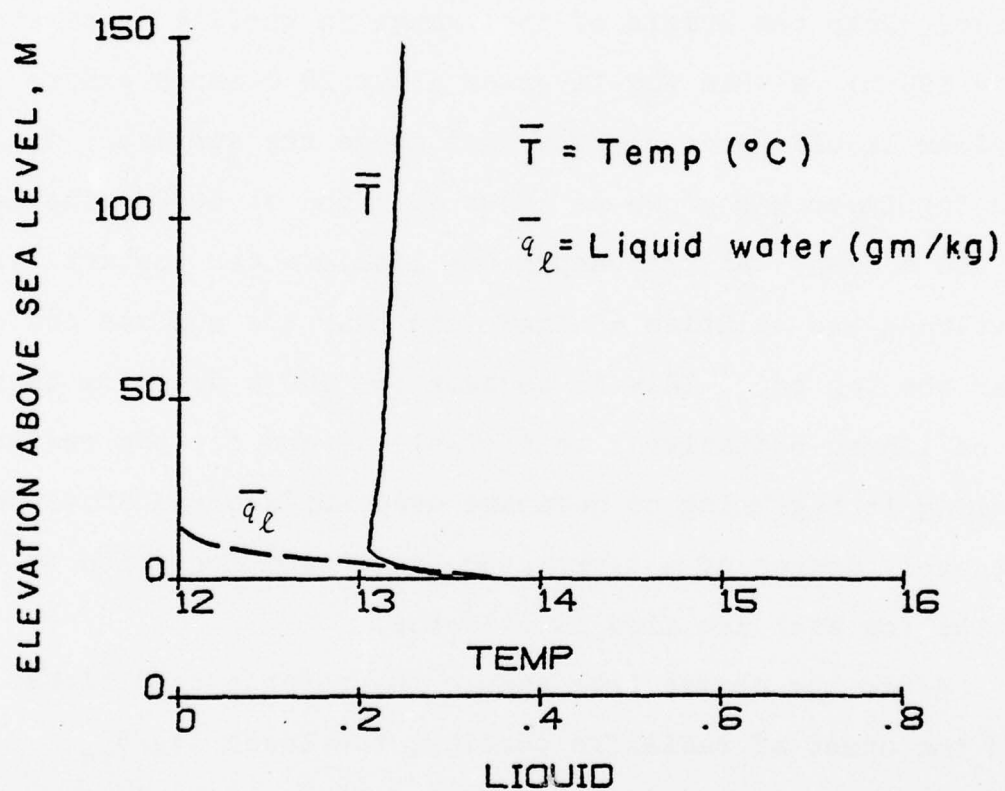


Figure 3a. Temperature and liquid water content profiles in an advective-radiative fog at $x = 100$ m .

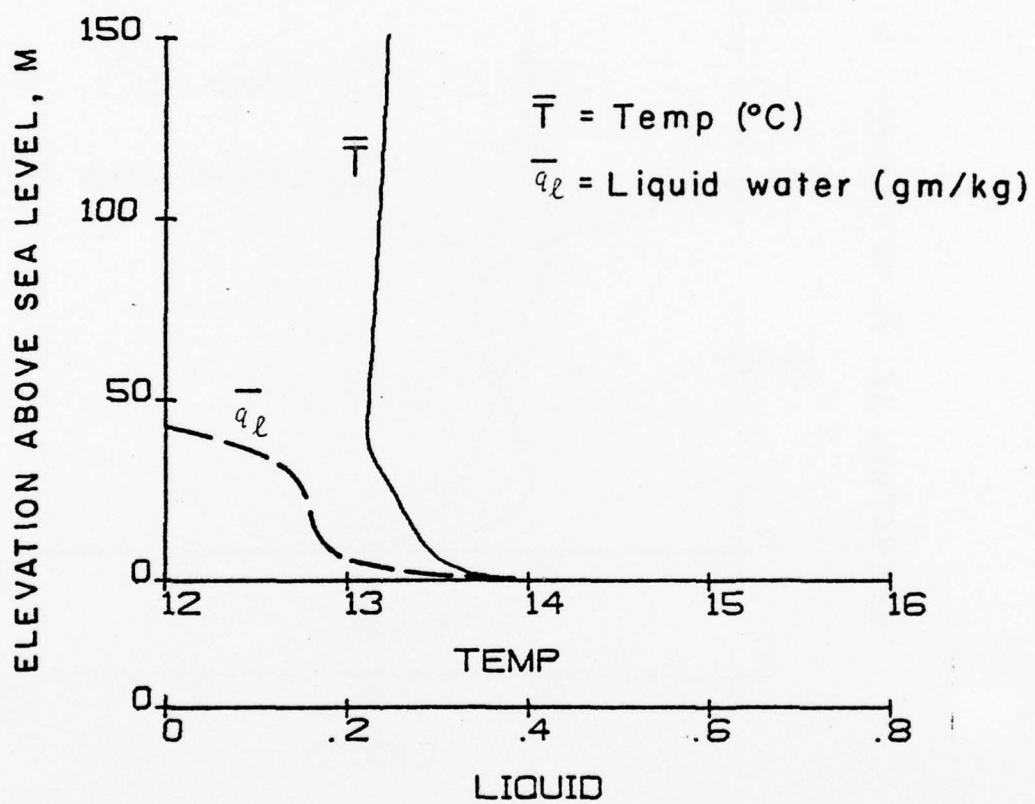


Figure 3b. Temperature and liquid water content profiles in an advective-radiative fog at $x = 1000$ m .

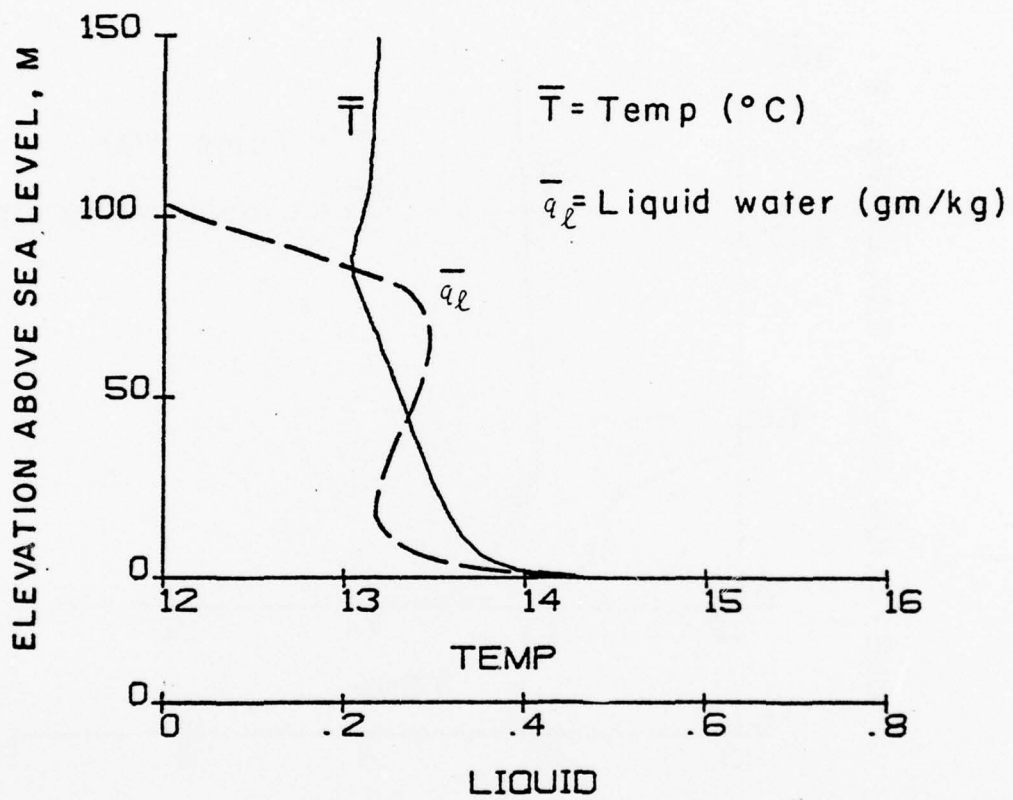


Figure 3c. Temperature and liquid water content profiles in an advective-radiative fog at $x = 3000$ m .

$$u_* \theta_*^{\text{rad}} = \frac{1}{\rho C_p} \int_0^{\delta} \left(\frac{\partial q^{\text{rad}}}{\partial z} \right) dz$$

Direct comparison of θ_*^{rad} with θ_{s*} provides an assessment of the strength of radiation transport compared to turbulent transport in the fog layer. For this warm surface advection fog, $\theta_*^{\text{rad}}/\theta_{s*}$ is approximately 0.5. The role of radiation is therefore pivotal in its evolution.

The structure of radiative cooling in the fog is shown in Fig. 4. In the first 1000 m, maximum, radiative cooling is concentrated at the surface but then begins to shift upward into the center and top of the cloud bank as it becomes radiatively thick to terrestrial radiation. The turbulence level depicted in Fig. 5 shows a steady increase in x as the unstable mixed layer grows with the maximum turbulence levels concentrated in the center of the cloud bank.

ISOPLETHS OF RADIATIVE COOLING

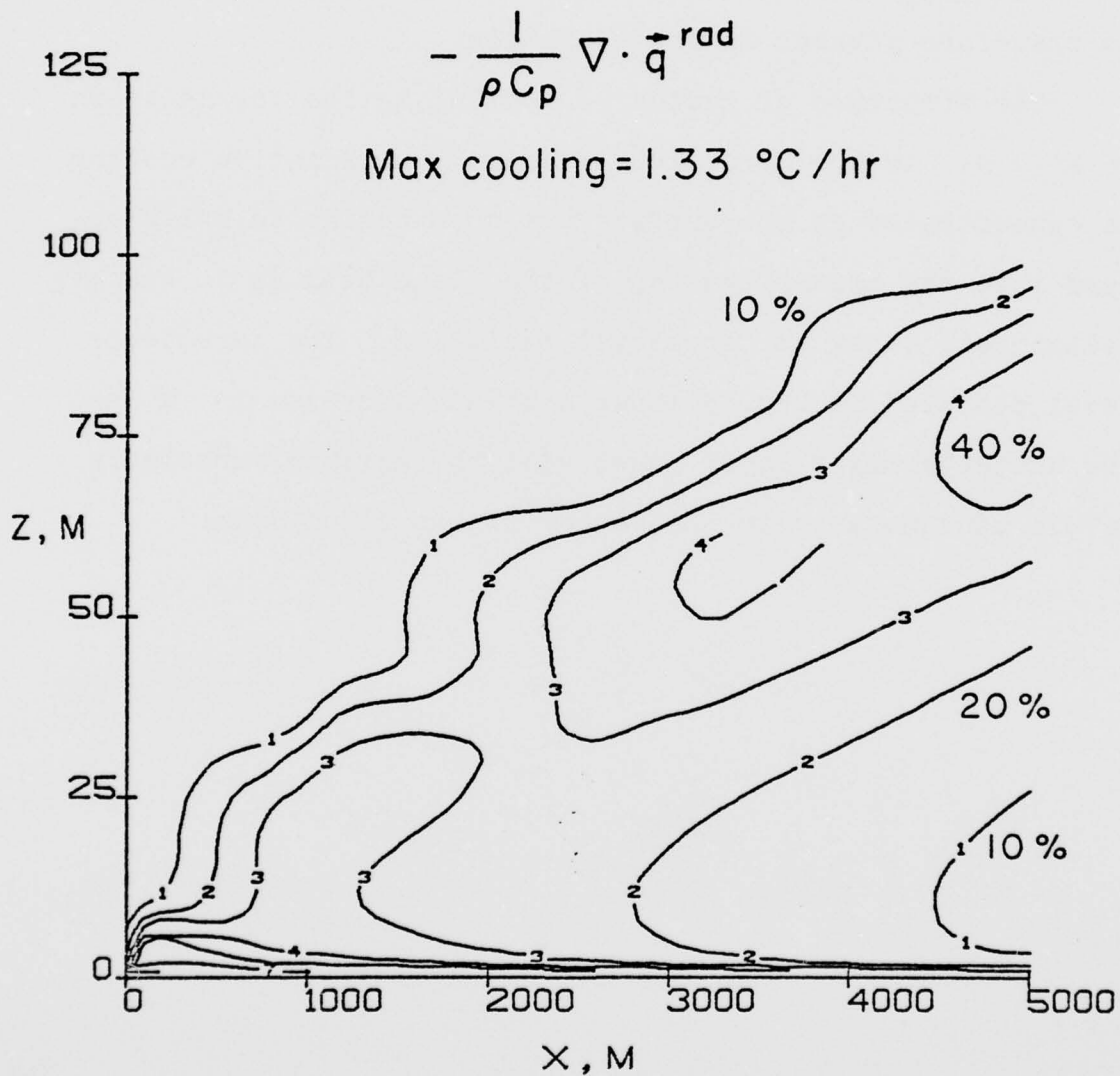


Figure 4. Radiative cooling distribution in advective-radiative fog. Note shift of maximum cooling rate away from surface to top of cloud bank as fog bank becomes radiatively thick ($\delta \gtrsim \lambda_{\text{rad}}^T$).

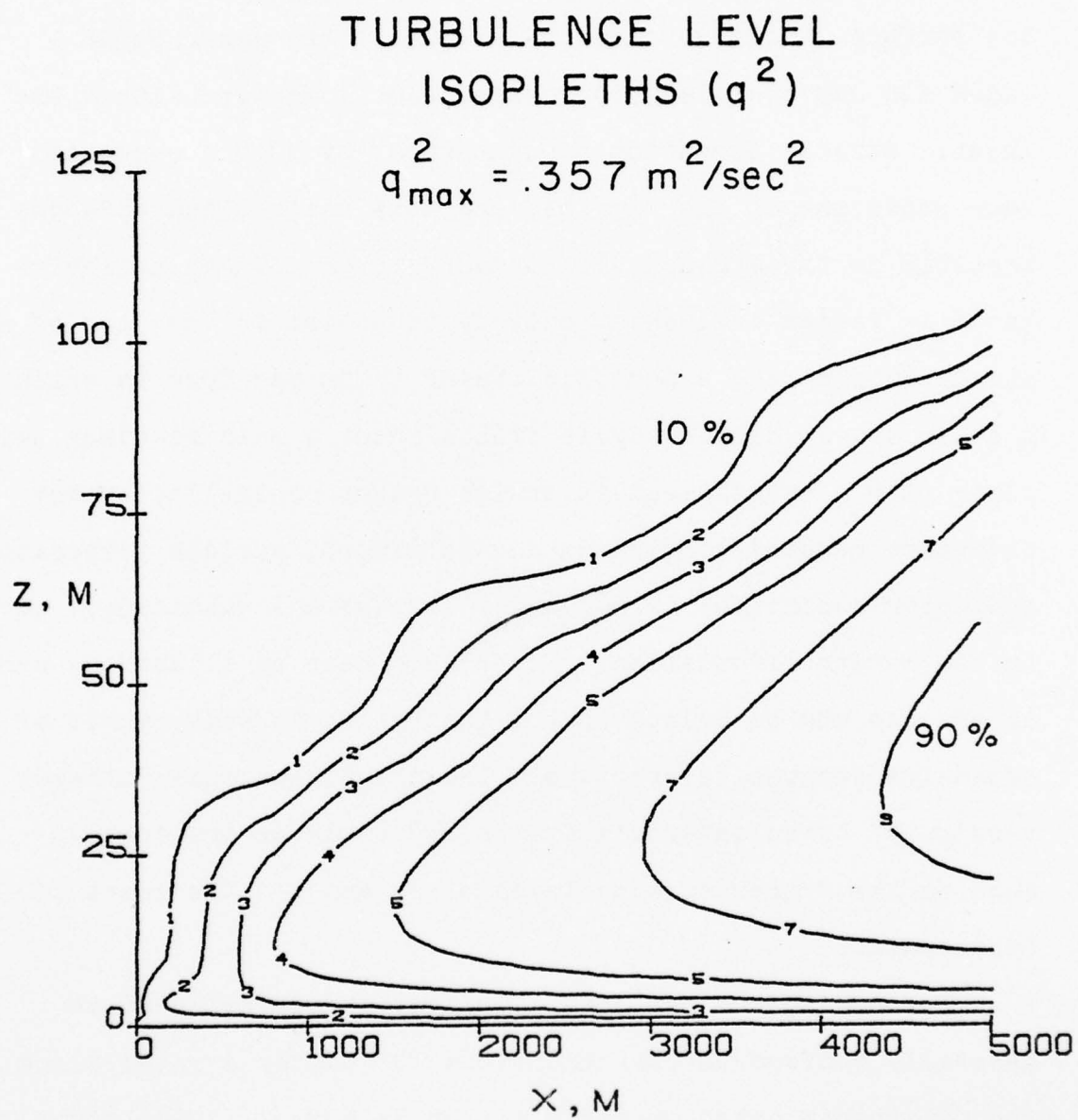


Figure 5. Turbulence (q^2) distribution in advective-radiative fog.

6. Boundary layer with stratus cloud

A boundary layer over a large expanse of water capped by a subsidence inversion will turbulently ingest moisture from the surface. Long wavelength cooling of the water vapor laden air may then lead to condensation somewhere within the layer. Stratus formation brought about by such a sequence represents one of the simplest and most basic cloud episodes possible in the atmospheric boundary layer. In an expansive basin or region influenced only by advection in the form of a steady subsidence, a periodic steady state may form in which a solar driven diurnal cycle exists about a mean boundary layer state with a steady mean inversion height controlled by the radiative conditions (season and latitude), surface temperature, and upper conditions (wind, water content and subsidence) set by the larger circulation. We proceed next to illustrate such an episode and to relate that illustration to occurrences of expansive stratus layers (where the one-dimensional unsteady version of turbulent-radiative theory would be applicable) such as the summer stratus layer along and off the coast of California.

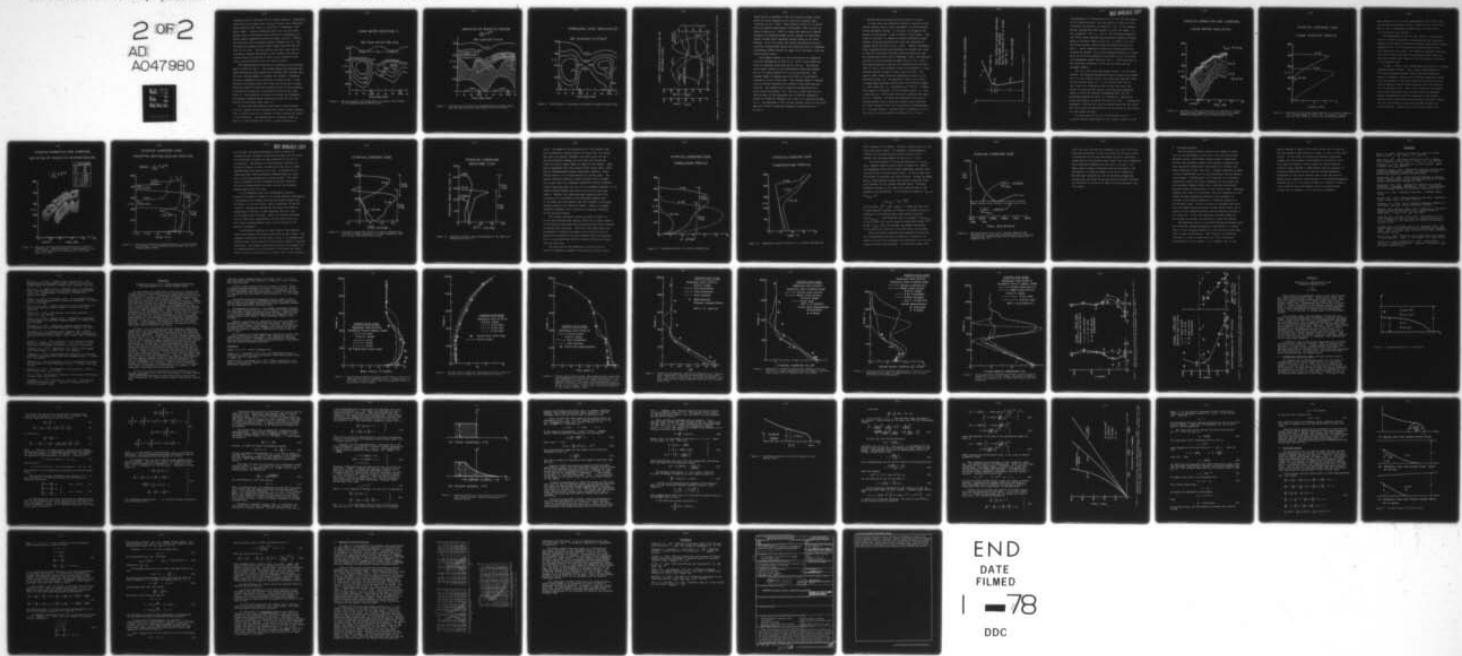
The conditions for this illustration are selected to generally conform to the conditions for summer stratus along the California coast as described by Neiberger (1944) and more recently observed by Mack et al. (1974). Surface boundary conditions are established for a fixed temperature sea state of 17°C , surface water mixing ratio at saturation, and surface roughness determined by Froude scaling [Eq. (26)]. Radiation

AD-A047 980

AERONAUTICAL RESEARCH ASSOCIATES OF PRINCETON INC N J F/G 4/1
1977 STATUS REPORT ON LOW-LEVEL, ATMOSPHERIC TURBULENCE MODEL F--ETC(U)
NOV 77 W S LEWELLEN , D A OLIVER, M E TESKE N00019-77-C-0131
ARAP-320 NL

UNCLASSIFIED

2 OF 2
AD
A047980



END
DATE
FILMED
1 -78
DDC

conditions are for latitude 40°N at summer solstice. Geostrophic conditions set an upper level wind of 10 m/sec and a subsidence whose characteristic value is $.5 \times 10^{-6} \text{ sec}^{-1}$ (Neiberger, 1961; Lilly, 1968). Initial conditions (which will be lost after several days of simulation) were selected to correspond to a mildly stable temperature profile of lapse $\partial\theta_v/\partial z = .003^{\circ}\text{C/m}$ and clear sky with an initial relative humidity of 0.9. The calculation is begun shortly before sunset the first day and runs for six days. Behavior during day-light hours must be considered somewhat approximate in the present illustration because droplet scattering of direct solar radiation would reduce solar penetration into the cloud interior.

The quasi-periodic evolution of cloudiness in the boundary layer is shown in Fig. 6. The stratus grows both downward and upward during nocturnal periods and thickens until sunrise when the solar heating begins to disperse the stratus. Radiative cooling is dominant at the cloud top as shown in Fig. 7, and produces an unstable lapse rate within the cloud and a correspondingly enhanced turbulence production which is also maximum in nocturnal periods and in the upper portion of the cloud (Fig. 8). The radiation cooling at the cloud top strengthens the capping inversion which oscillates up and down over the period of the diurnal cycle (Fig. 9).

We note that the predicted cloud base in these diurnal cycles is highest in late afternoon and lowest in early morning (Fig. 9) while cloud top is highest in early morning and lowest in late afternoon. Correspondingly the inversion height is highest in early morning and lowest in later afternoon--a

LIQUID WATER ISOPLETHS, \bar{q}_ℓ

Max liquid content = .561 g/kg

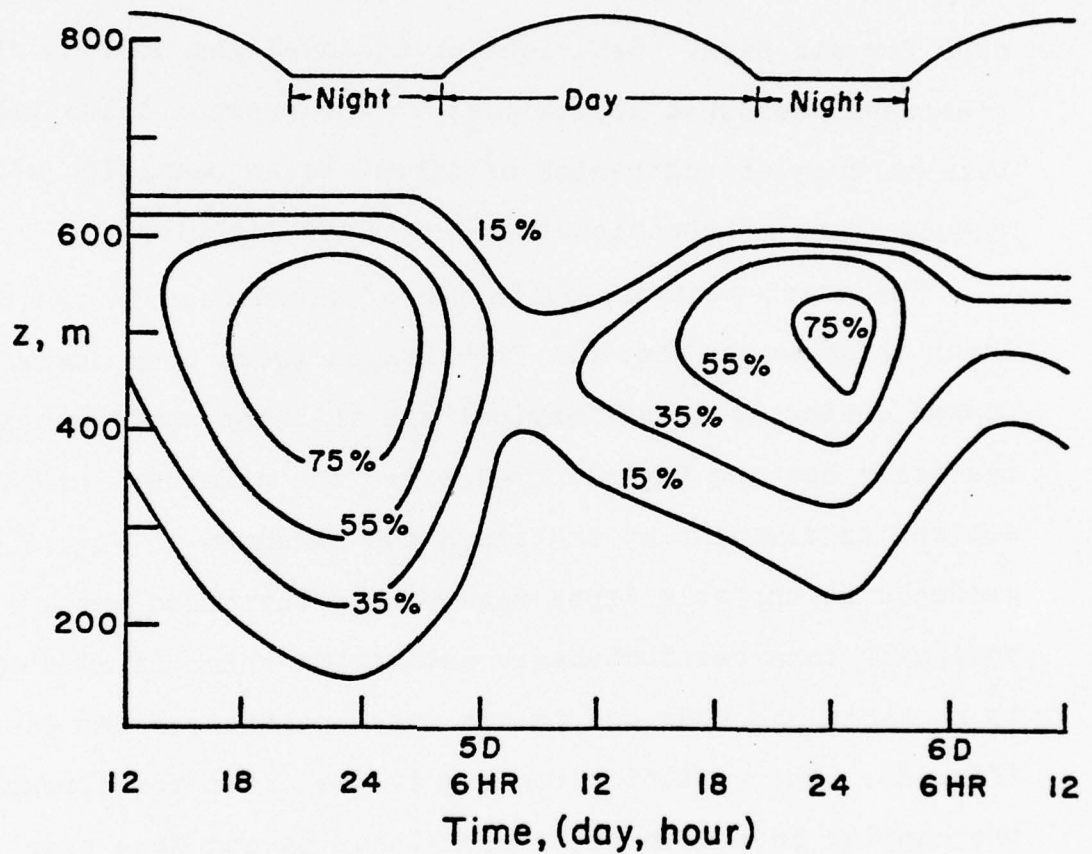


Figure 6. Diurnal variation of liquid water in stratus cloud formed in a subsidence capped boundary layer.

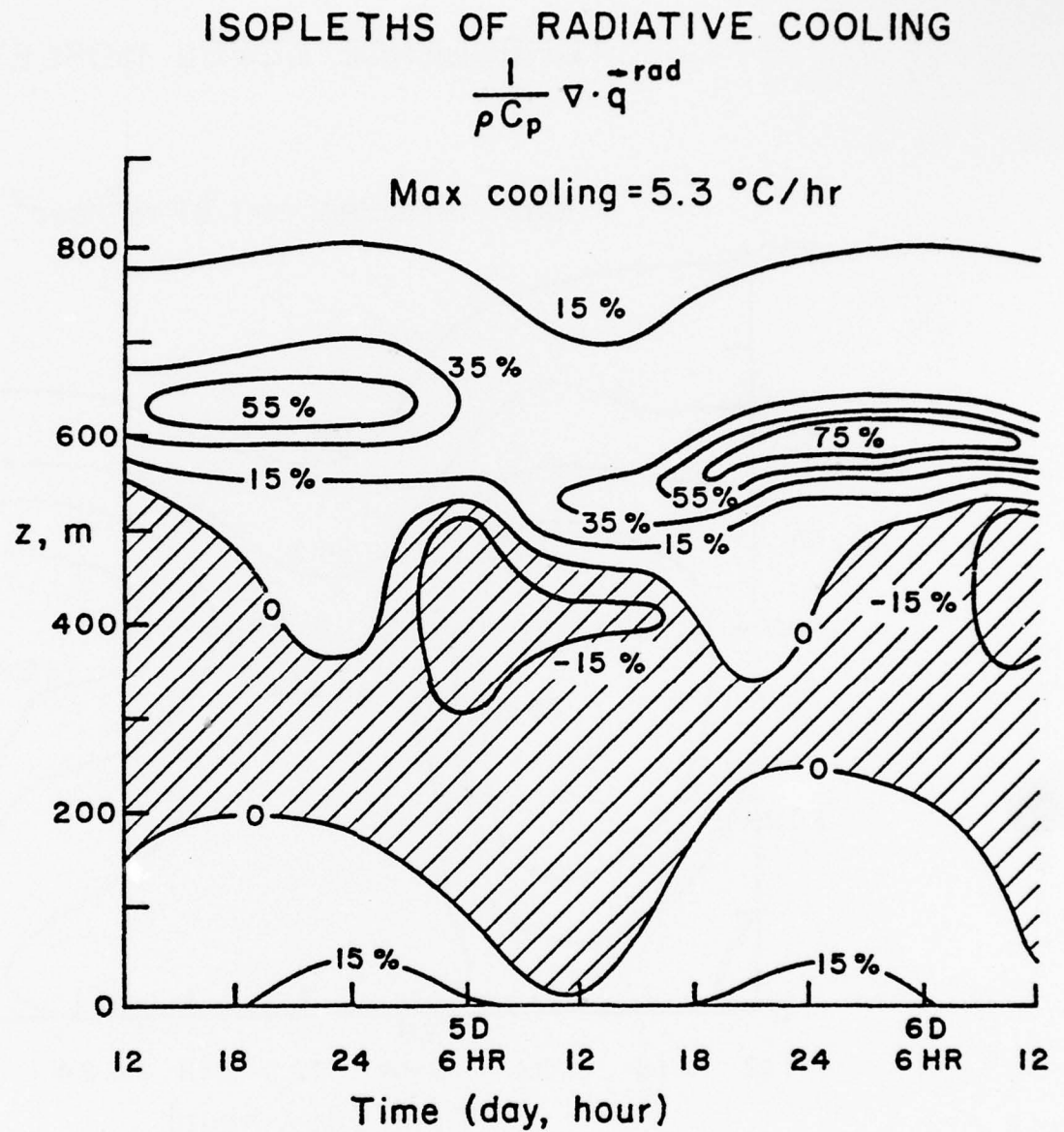


Figure 7. Distribution of radiative cooling/heating in stratus cloud. Note net heating occurs deep within the cloud interior.

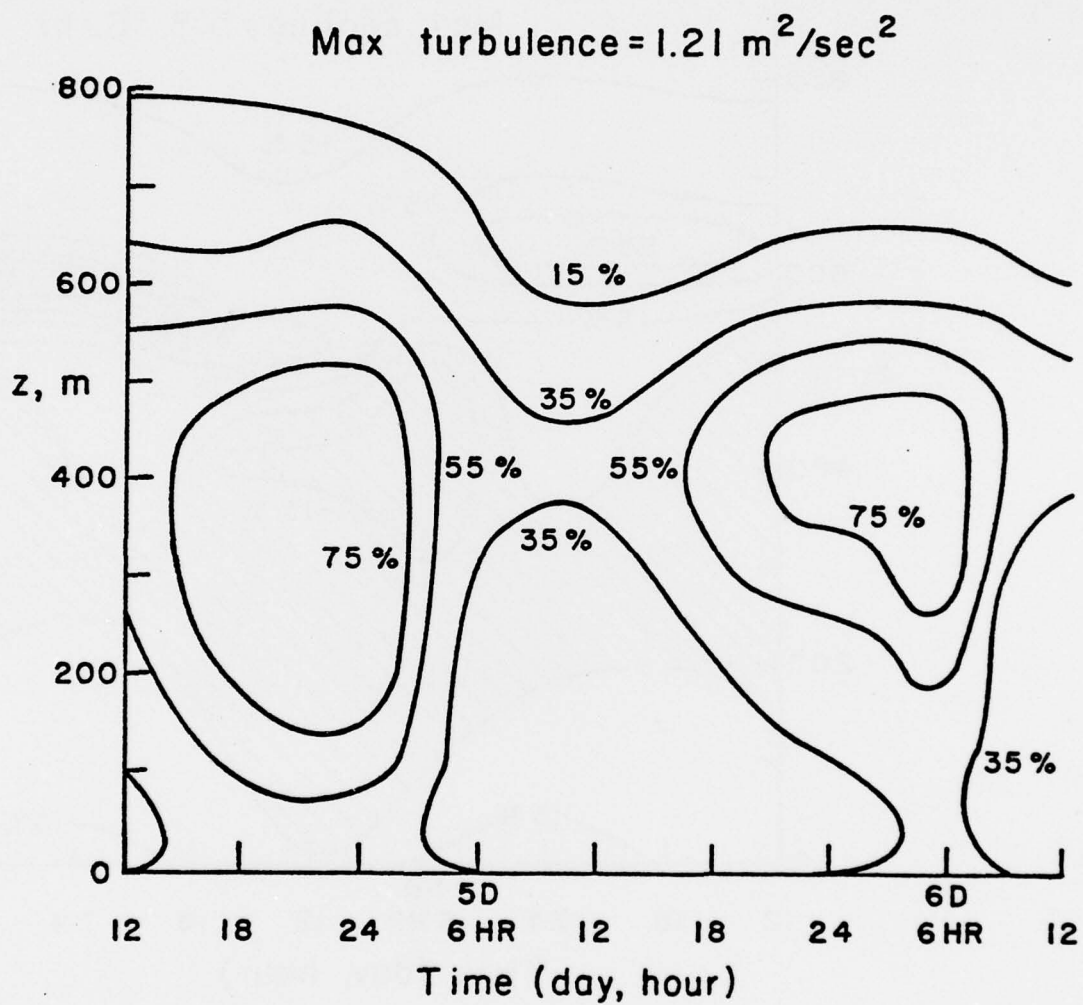
TURBULENCE LEVEL ISOPLETHS (q^2)

Figure 8. Distribution of turbulence in diurnally varying stratus cloud.

DIURNAL VARIATION OF CLOUD BASE AND TOP AND SURFACE FLUXES

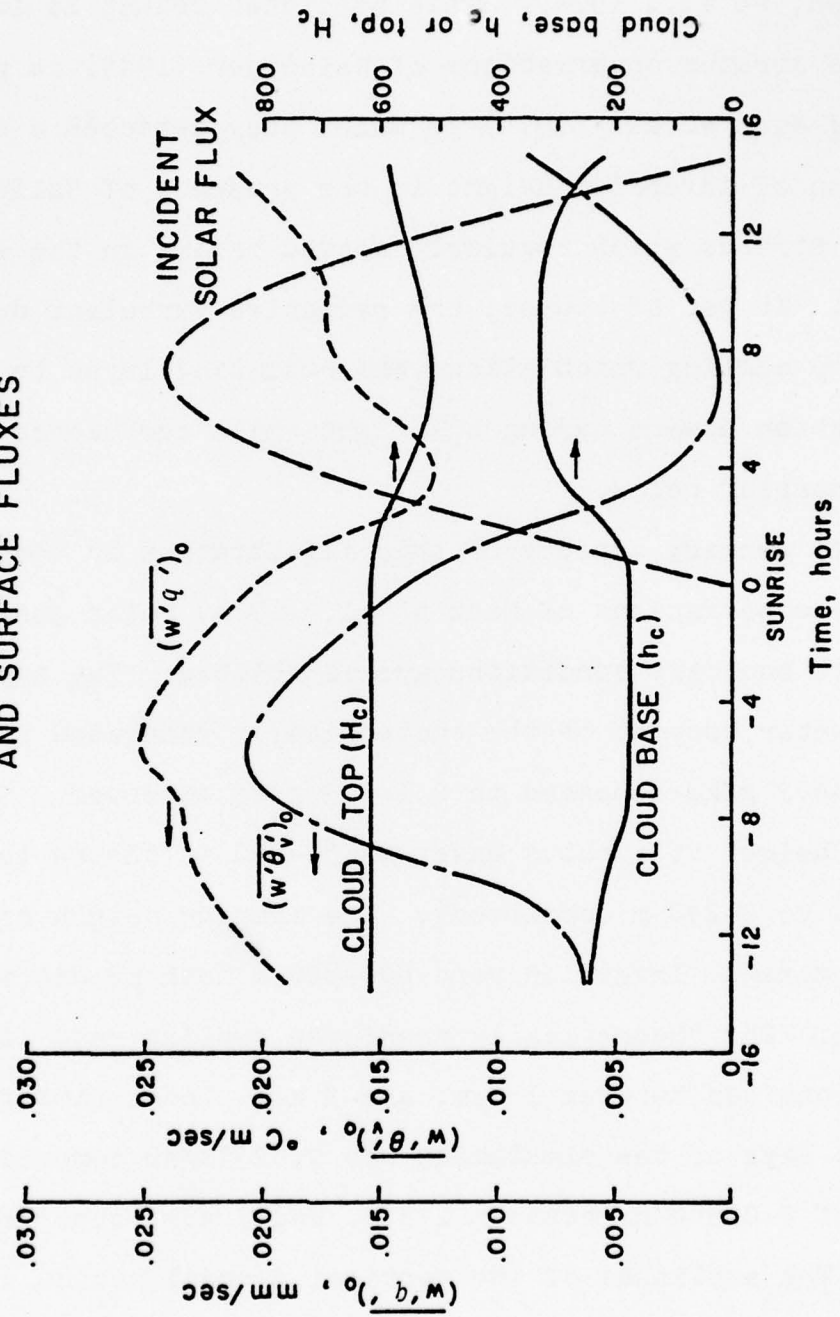


Figure 9. Diurnal variation of cloud base and top and heat and moisture fluxes at the surface.

result which is *opposite* to that for inversion height cycles driven by solar heating in the cloud-free boundary layer (Lewellen, et al., 1974). This predicted result is in accord with the stratus observations of Neiberger (1944) as well as those of Mack et al. (1974) in which they detected a diurnal variation of inversion height in the presence of California coastal stratus which regularly showed maxima in the early morning. It is, of course, the radiative-turbulent drive of cloud top cooling which allows the radiating layer to propagate condensation upward during the night while turbulence cools the cloud interior below.

Some summary aspects of this illustration in comparison with the observations of Mack et al. (1974) which guided the choice of boundary conditions are as follows. The typical liquid water content of the theoretically generated stratus was 0.1-0.2 g/kg compared to 0.1-0.3 g/kg observed. The average height of stratus base was 50-200 m (theoretical) compared to 0-200 m (observed). The average height of stratus tops at maximum inversion were 600-800 m both predicted and observed. The theoretically predicted cooling rate 100 m below cloud top between 1 a.m. and 3 a.m. local time for the last two days of the simulation was 0.023°C/hr compared to values of 0.025°C/hr between 1 a.m. and 5 a.m. observed by Mack, et al. The amplitude of the vertical diurnal motion of the cloud base was 100-150 m predicted compared to observations of 50-150 m .

7. Surface fog resulting from the lowering of stratus

We have seen that radiative-turbulent coupling of subsidence capped stratus layers propagates the base downward during nocturnal cooling. If the base is propagated completely to the ground, a fog is formed at the surface. This class of fog event is common in coastal California during periods of strong subsidence and has been described by Leipper (1948) and Mack, et al. (1974). Several atmospheric fluid mechanisms have been postulated to explain this class of fog event including vertical convection driven by the sea breeze-land breeze cycle (Neiberger, 1944), and radiative cooling of stratus during the night (Mack, et al., 1974). The single necessary condition all observers note for this class of fog is the existence of the late afternoon or early evening inversion height at about 400 m or lower. The typical clear summer afternoon temperature profile is as indicated in Fig. 10, as measured by Mack et al., (1974). A strong upper inversion exists above the inversion height z_1 with lapse rate Γ_u typically about $.04^\circ\text{C}/\text{m}$. A transition region of thickness $\Delta z = 40 \text{ m}$ exists above z_1 with a lapse rate of $.01^\circ\text{C}/\text{m}$ while below the inversion the lapse rate is $-.015^\circ\text{C}/\text{m}$. We begin our prediction with such an initial profile over a fixed sea surface state utilizing the model of Parts 1 and 2 in the vertical one-dimensional (z) unsteady version. Initial relative humidity is .97 in the region up to the inversion falling off to a value

STRATUS FORMATION AND LOWERING

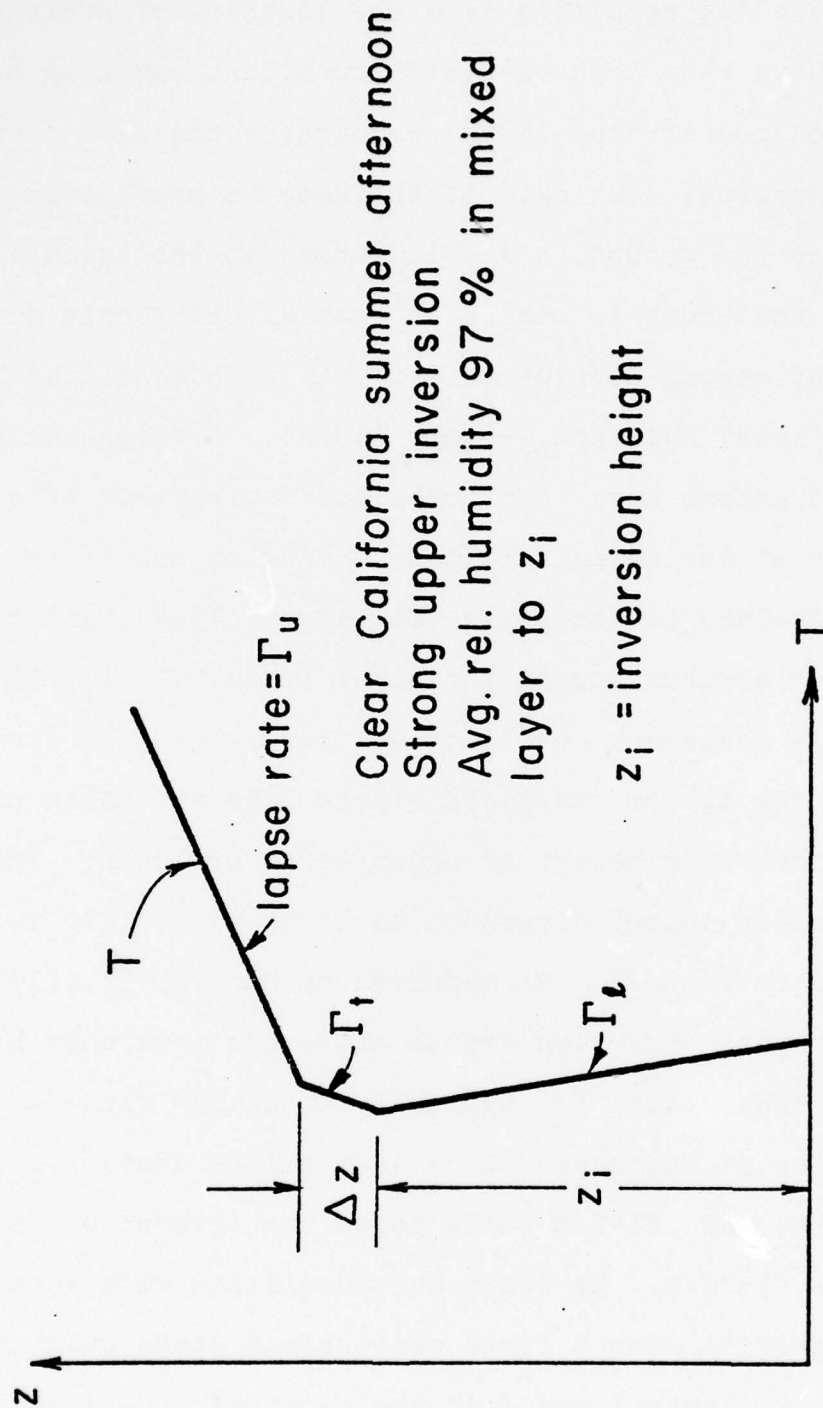


Figure 10. Typical late afternoon temperature profile measured by Mack et al. (1974).

corresponding to a mixing ratio of $q = .001$ over the region of the transition zone. The calculation is done for solar inclination at solstice and begun at 7 p.m. in the evening. Several calculations were carried out with the height z_1 as a parameter. For $z_1 = 300$ m, the atmosphere begins to cool after sunset through long wavelength radiation brought about by the water vapor in the air. At about 1 a.m. the following morning, stratus forms extending from 230 m to 300 m. After condensation begins the stratus grows both downward and upward. The cloud propagates downward to within about 140 m of the surface at which time (5 a.m.) the cloud top propagating upward exists at 450 m. From this time on, the cloud base continues to lift and both base and top propagate upward.

For $z_1 = 200$ m the same dynamic occurs. In this case, however, the downward propagating stratus reaches the surface by 5 a.m. and remains until 7 a.m. when the cloud base lifts off the surface (Fig. 11). It can be seen from Fig. 11 that there is an indication that surface fog forms just before the stratus base reaches the ground and propagates upward to reach the downward propagating base, the two coalescing together at about 10 m elevation. During this period the stratus top grows from 230 m to 350 m. Through the remainder of the day the cloud top moves upward and the cloud base lifts until by mid-afternoon the top exists at 400 m while the base exists at 225 m.

As can be seen in Fig. 12, the afternoon (3 p.m.) cloud has thinned (approximately 200 m deep) compared to the

STRATUS FORMATION AND LOWERING

LIQUID WATER ISOPLETHS

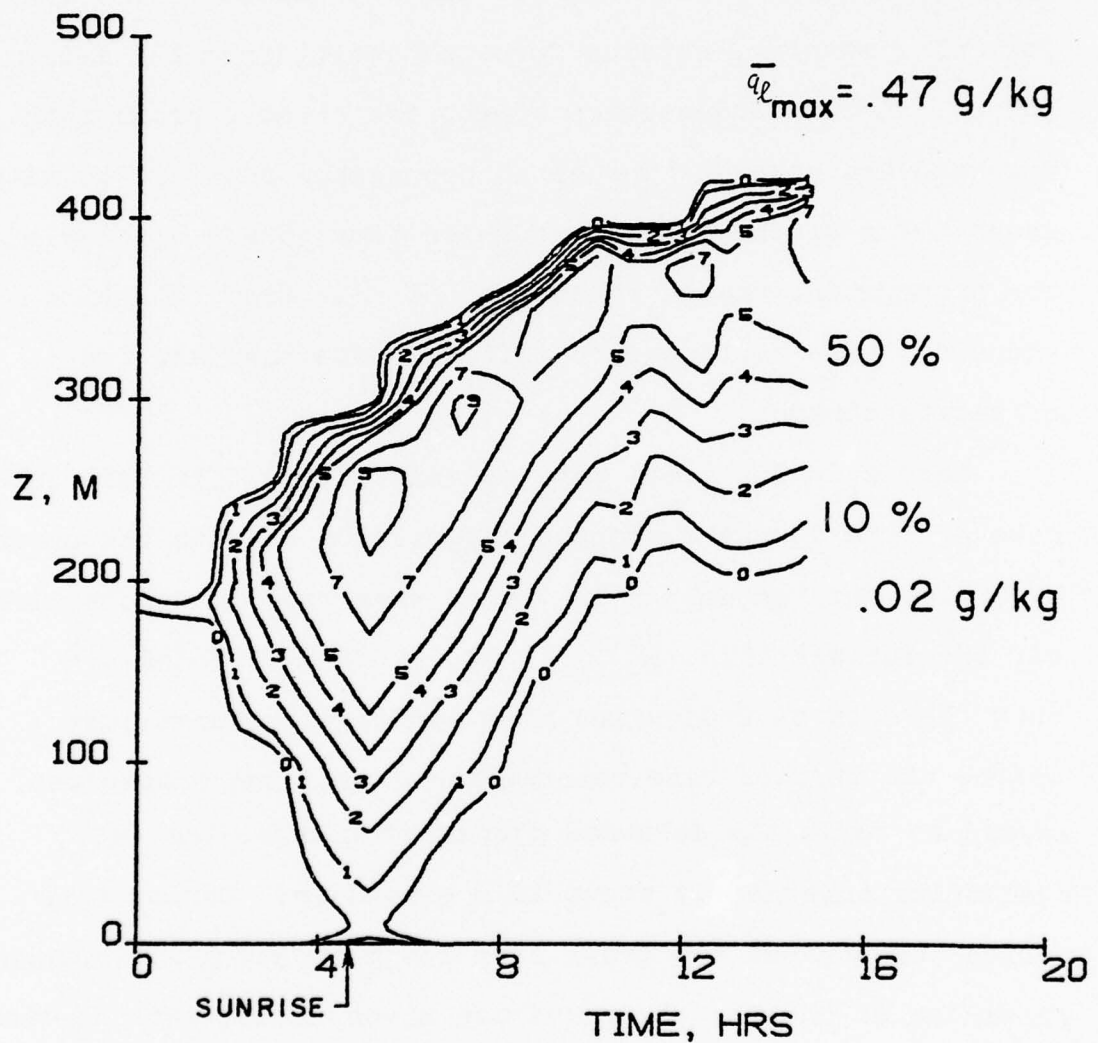


Figure 11. Evolution of fog resulting from the lowering of stratus. Fog shows some tendency to form at surface just before downward propagating stratus reaches the surface.

STRATUS LOWERING CASE

LIQUID CONTENT PROFILE

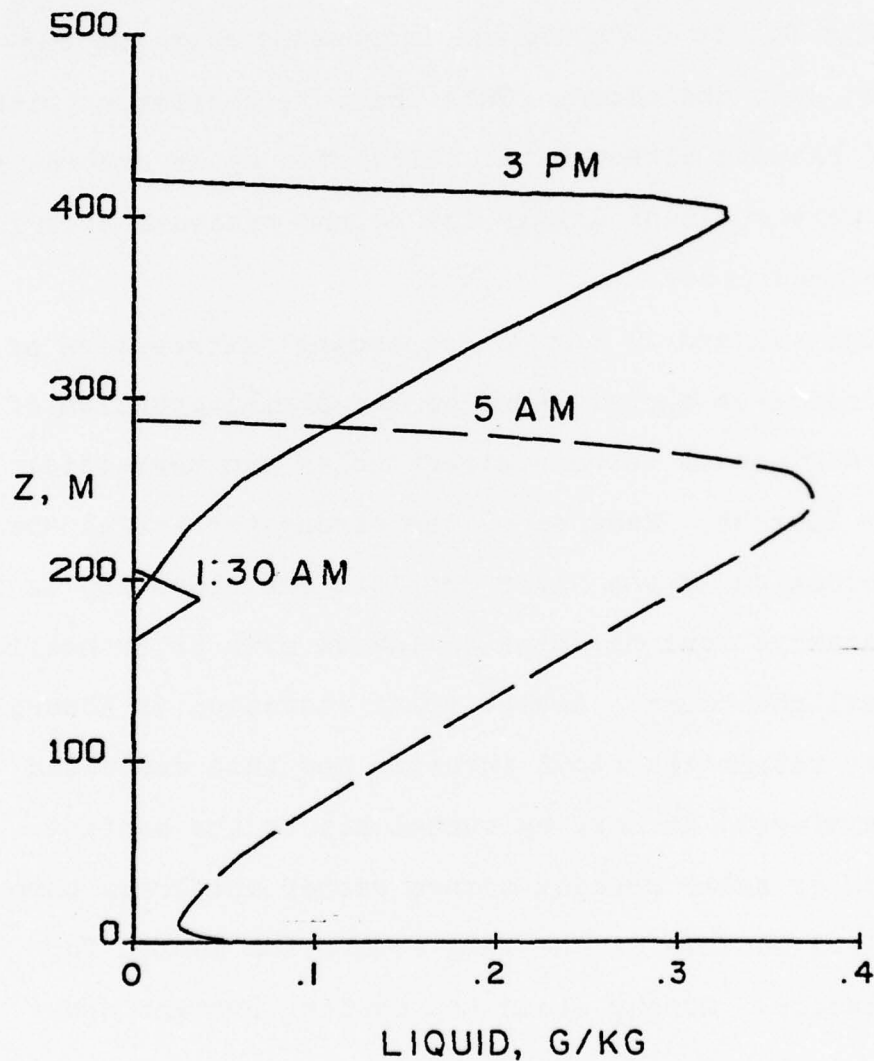


Figure 12. Variation of the liquid water profile in a stratus lowering fog. Stratus forms at about 1 am, is lowered to ground at 5 am, and lifted at 3 pm in the following afternoon.

early morning (5 a.m.) cloud (approximately 350 m thick) and the average liquid water content is reduced about 50 percent. This is due to evaporation brought about by direct solar radiation during the daytime.

The measurements of Mack et al., (1975) of liquid water content in stratus lowered to the surface and for conditions typical of the present calculation indicate liquid water content ranging from 0.1 to 0.2 g/kg and increasing from the surface upward into the cloud. This trend is consistent with the calculated results although the calculated water content is less than measured most likely due to the presence of drizzle in the measured case.

In Figs. 13 and 14 the corresponding distribution of radiant heating/cooling is shown. Here we see a manifestation of the large difference between direct solar and terrestrial absorption lengths. Because of the strong terrestrial absorption and emission of the water droplets the cloud top is in strong radiative cooling which dominates over solar heating even in daylight hours. Direct solar radiation is absorbed much deeper within the cloud interior and this deposited energy transferred as heat by turbulence to the surface. Evaporation by solar heating occurs rather uniformly throughout the cloud because of the long absorption length for solar radiation. Strong cloud top cooling brought about

STRATUS FORMATION AND LOWERING

ISOPLETHS OF RADIATIVE HEATING/COOLING

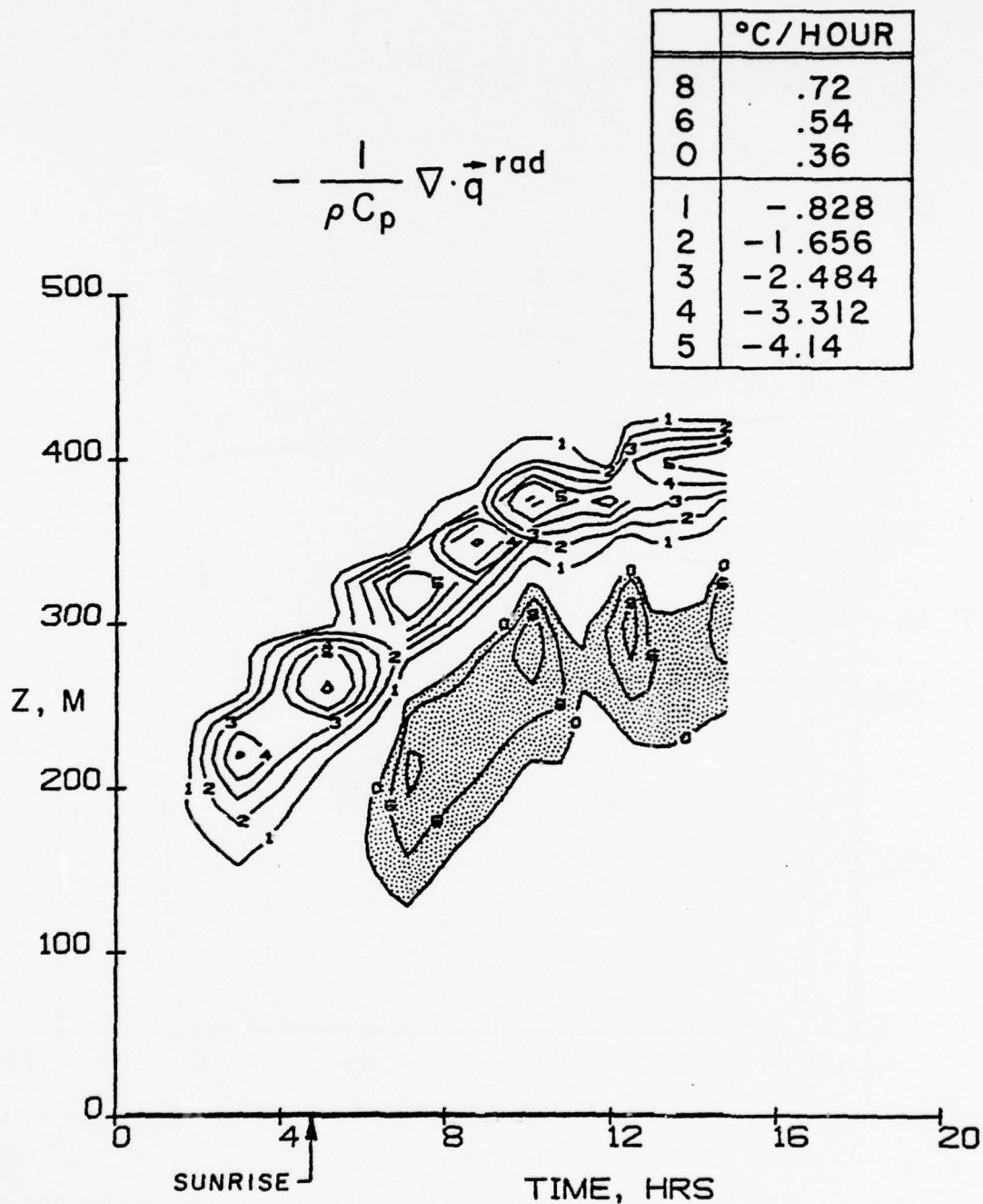


Figure 13. Radiative cooling/heating distribution in a stratus lowering fog. Maximum cooling is concentrated at cloud top. After sunrise, net heating occurs, but deep within the cloud.

STRATUS LOWERING CASE

RADIATIVE HEATING/COOLING PROFILES

$$Q_{RAD} = - \frac{1}{\rho C_p} \nabla \cdot \vec{q}^{rad}$$

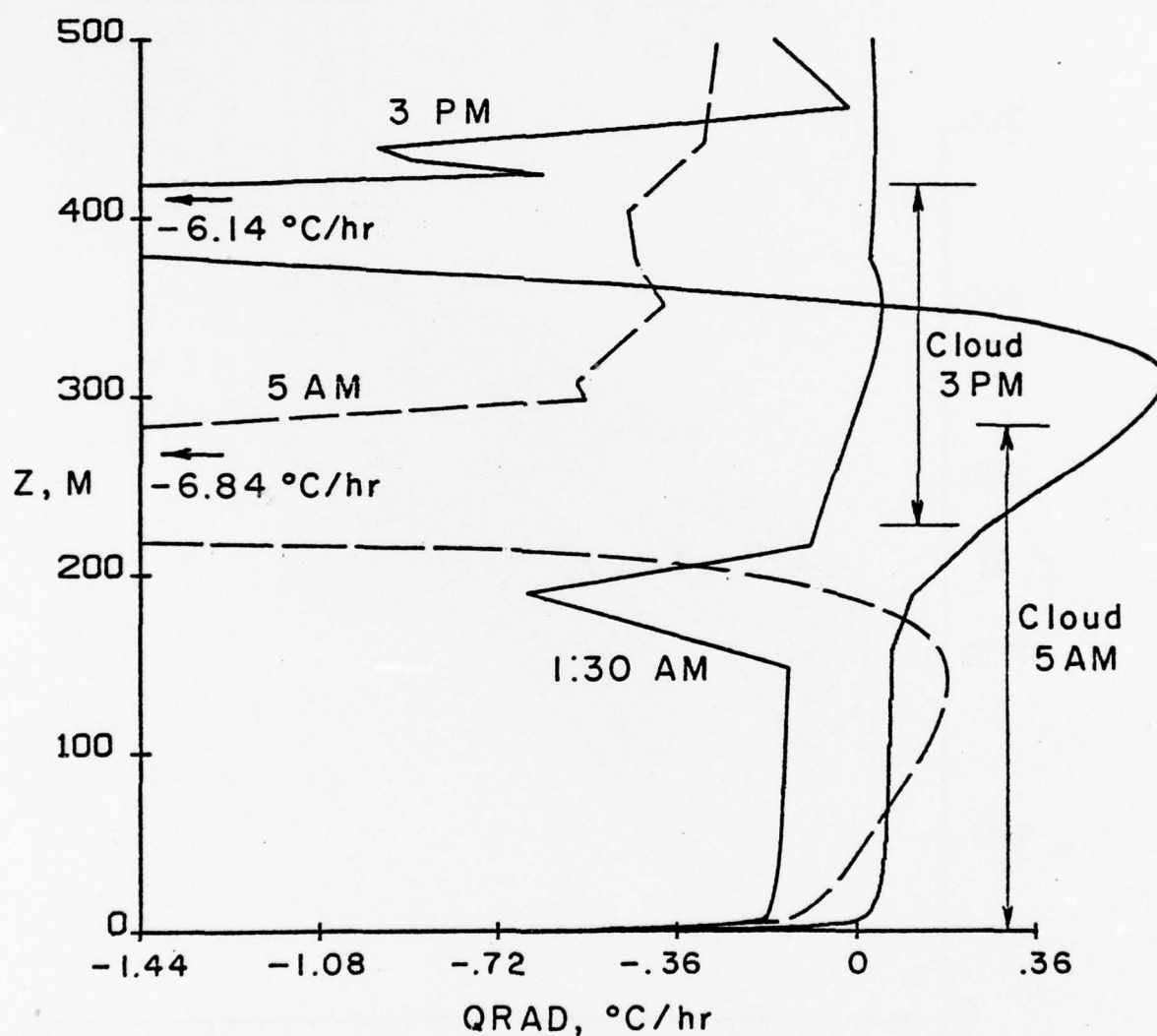


Figure 14. Profiles of radiative cooling/heating at 1:30 am (stratus just forming), 5 am (stratus on the surface), and 3 pm (stratus base lifted).

by the short terrestrial absorption length provides the instability and turbulence production machinery for the cloud to turbulently transport the heat deposited by the sun in its interior. The details of this turbulent transfer can be seen in Figure 15 where the turbulent heat flux is shown directed from cloud base to cloud top. It should also be noted that heat flows turbulently downward above the cloud top to the strong radiatively cooling surface. This heat flux is supported by the turbulence which has diffused a few tens of meters above the cloud top into the strongly stable region above the cloud.

It is noteworthy that the corresponding turbulent moisture flux shown in Figure 16 is always positive representing a continuous flow of water from the sea surface upward into the cloud. At no time (after stratus formation) during the course of lowering and raising was the water flux negative indicating a diffusion of water downward from the cloud to the region below the base. Hence, the relative downward flow of water from a radiatively cooling cloud could only take place by precipitation which is not included in the present calculation.

Precipitation transport of water down to the subcloud region will enhance the liquid water level in that region. The measured liquid water content shown in Fig. 12 is greater than predicted most likely because of the drizzle present in the measured case. The present theory does provide some insight as to the appropriateness of the entrainment hypotheses upon which simple cloud top mixing models are based (Lilly, 1968; Schubert,

STRATUS LOWERING CASE

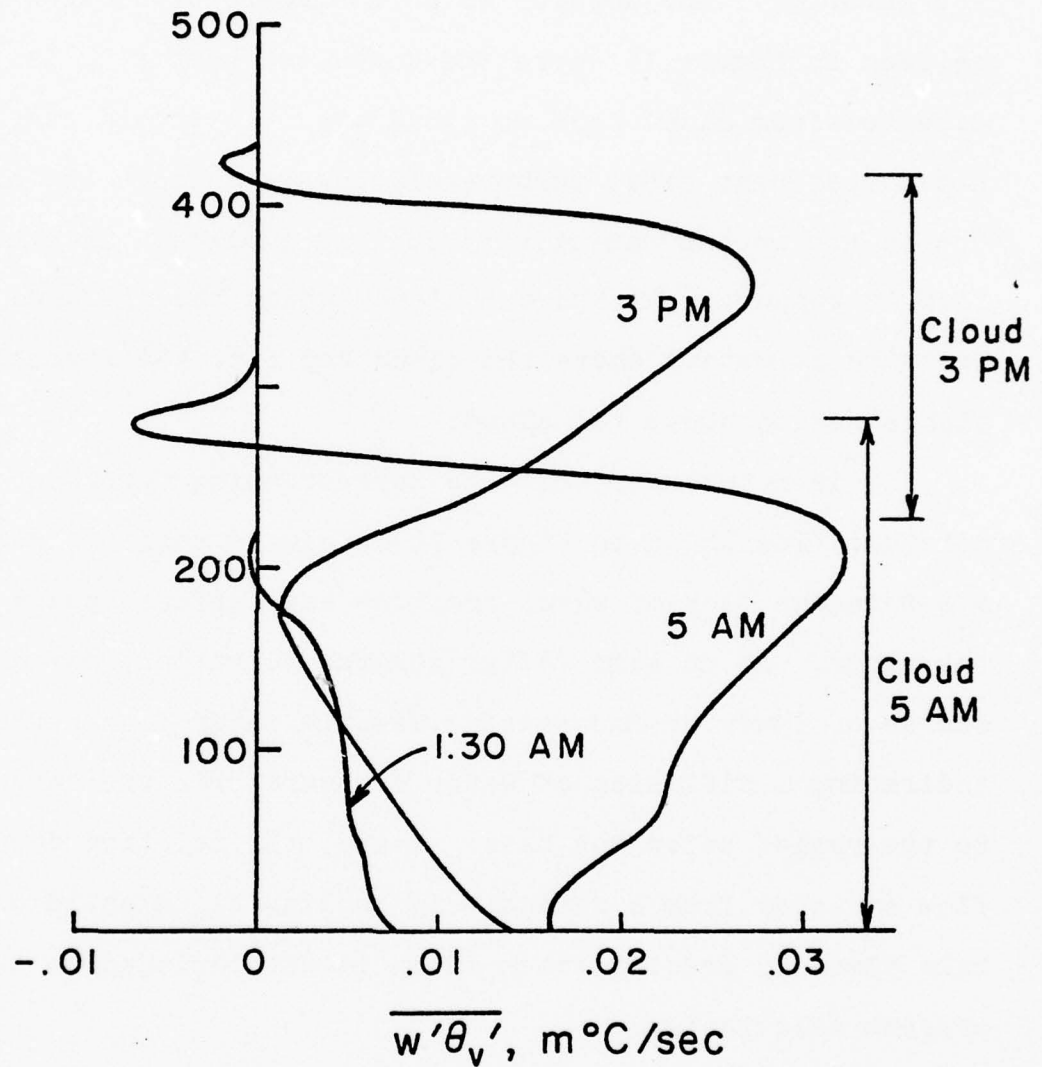


Figure 15. Turbulent virtual heat flux for a stratus lowering fog at time of stratus formation (1:30 am), lowering to surface (5 am), and lifted state (3 pm).

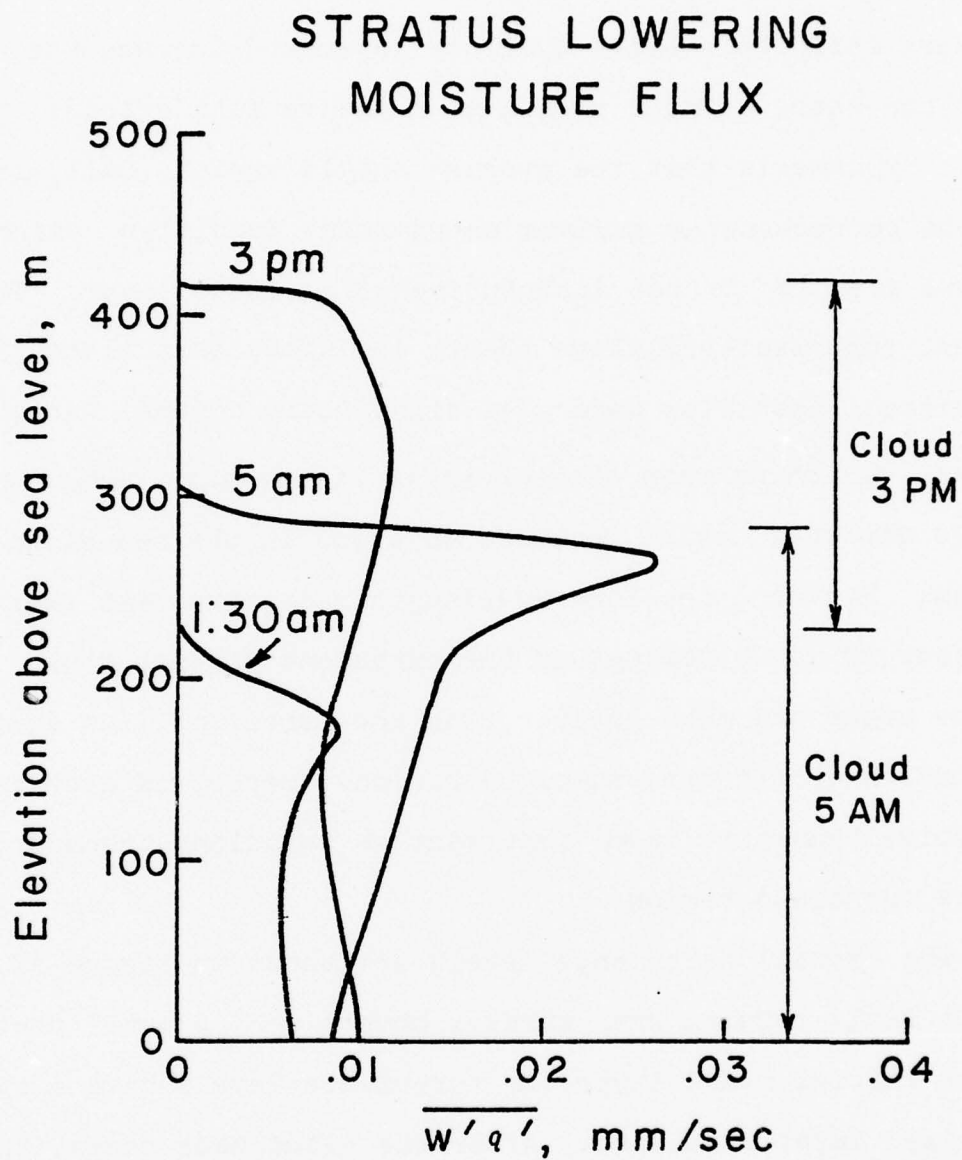


Figure 16. Turbulent moisture flux corresponding to the times and conditions of Fig. 15.

1976). In Figure 15 the distribution of the turbulent heat flux in diurnally varying stratus indicates that the virtual heat flux is positive throughout the mixed layer and has a positive definite average over the layer and through the cloud top where a small region of negative flux exists. Thus, Ball's hypothesis that the average should vanish (Ball, 1961) and the corresponding maximum entrainment condition which follows from it is not descriptive of a cloudy layer. The present turbulent-radiative theory indicates that although the virtual heat flux undergoes significant diurnal variation (nearly vanishing when the sun is at its maximum radiance), it is always directed upward from sea to cloud in the sub-cloud region. Further, the long wavelength radiative heat flux is about 10 to 20 percent of the turbulent virtual flux in the night and much greater than the turbulent flux during sunlight hours in the sub-cloud region. Hence, on average radiative transport is as important as turbulent transport in the sub-cloud region.

The overall turbulence levels are shown in Figure 17. In the early morning when stratus covers only a small portion of the initial mixed layer the turbulence levels have a typical dry mixed layer structure. After the cloud base rises, the confinement of radiative cooling to the cloud top and the presence of heating in the cloud interior skews the distribution to concentrate and locate the maximum turbulence levels near the cloud top.

The evolution of the temperature profiles shown in Figure 18 indicate a steadily intensifying cloud-top inver-

STRATUS LOWERING CASE TURBULENCE PROFILE

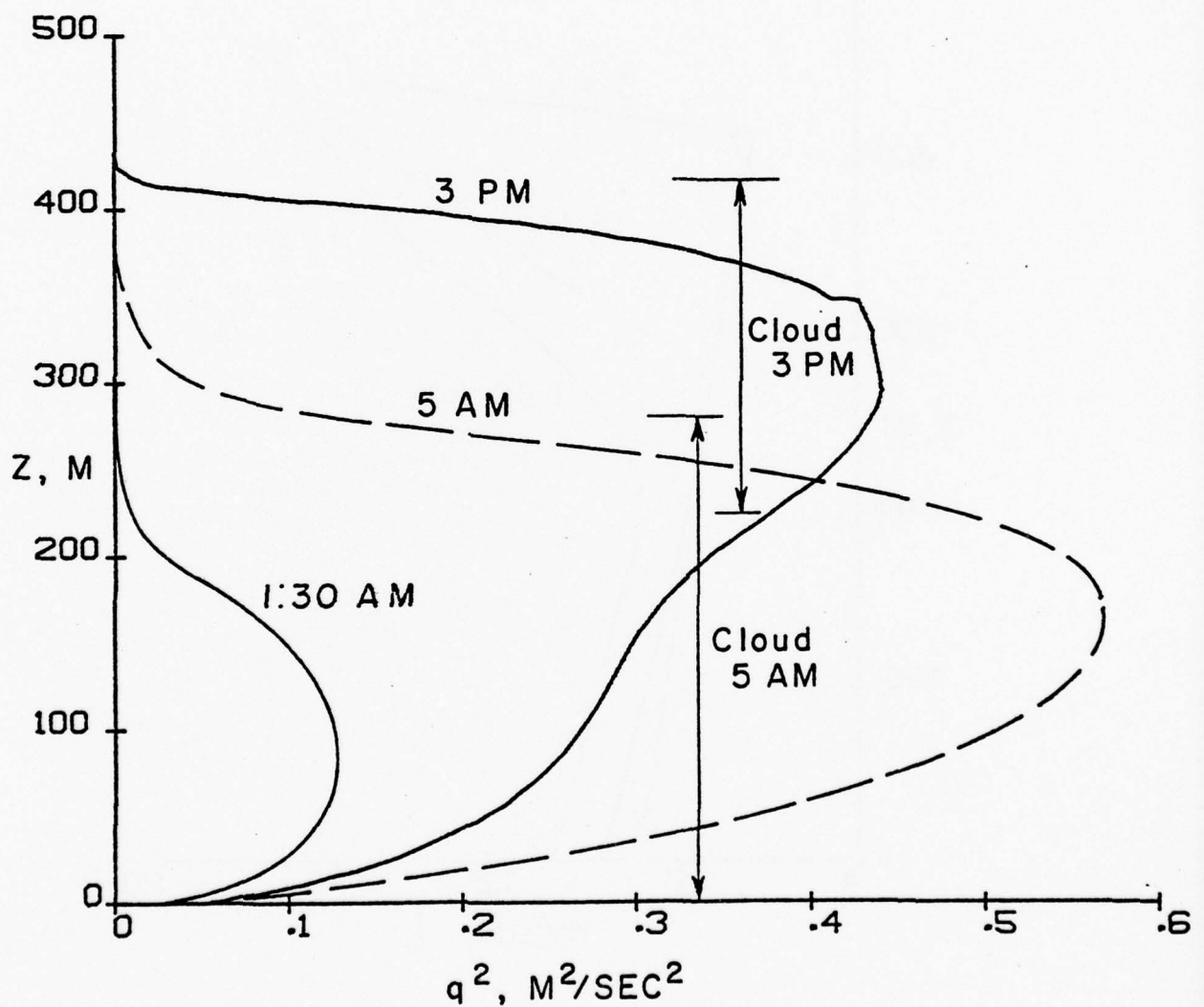


Figure 17. Turbulence levels in a stratus lowering fog.

STRATUS LOWERING CASE
TEMPERATURE PROFILE

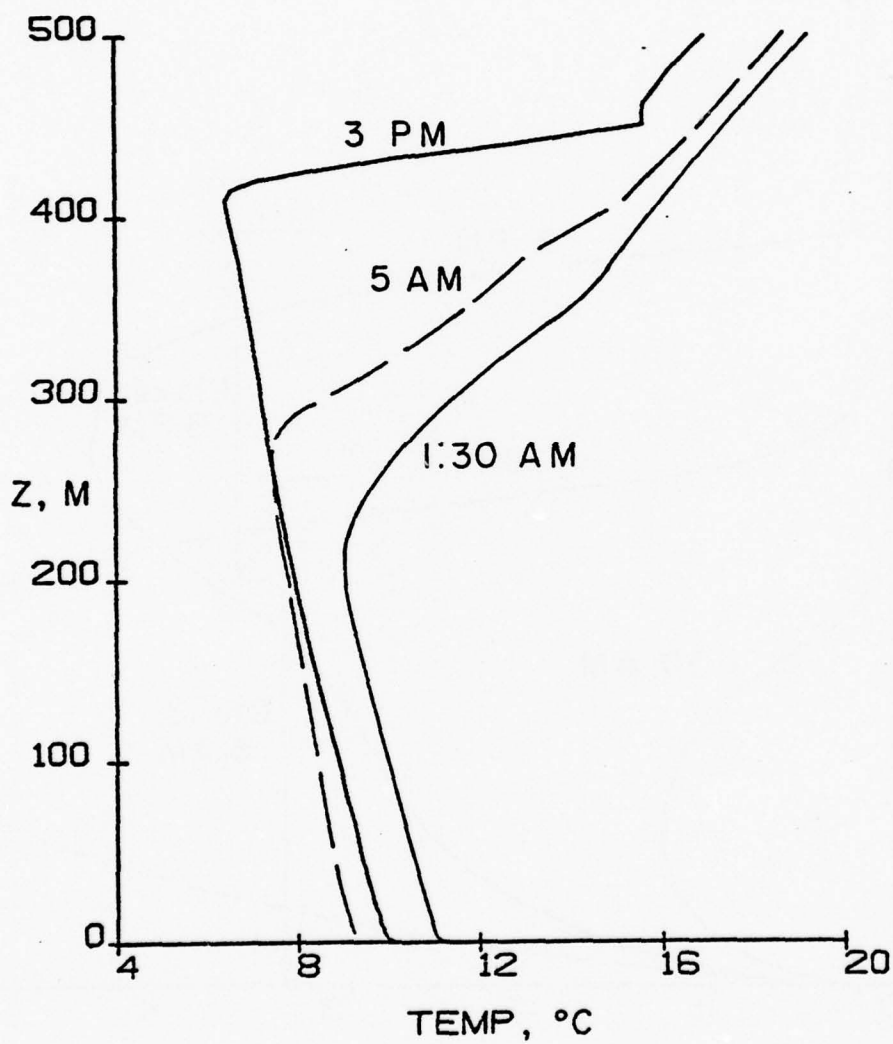


Figure 18. Temperature profile evolution in a stratus lowering fog.

sion compared to the weaker inversion characteristic of the clear sky initial state. An inversion of approximately $0.15^{\circ}\text{C}/\text{m}$ in the early morning before sunrise is consistent with the measurements of Mack et al. (1974).

It is of interest to follow the evolution of q_*/θ_{v*} for a stratus lowering fog as shown in Figure 19. Since the atmosphere cools over a fixed temperature surface, this fog falls into the warm surface class. It can be seen that the surface is initially far from critical. During the night, q_*/θ_{v*} falls rapidly towards the critical value but never quite reaches it; yet surface fog does exist. Turbulent existence criteria do not apply fully here because of the radiation cooling present. If we define an effective θ_{v*} as $(\theta_{v*})_{\text{eff.}}$ by

$$(\theta_{v*})_{\text{eff.}} = \theta_{v*} + \theta_*^{\text{rad}}$$

and calculate θ_*^{rad} over a region δ where the heat flux is approximately constant, we obtain a 15 percent effect of radiation in the surface layer which tends to elevate

$(q_*/\theta_{v*})_{\text{crit.}}$. This adjusted value is denoted $(q_*/\theta_{v*})_{\text{eff.}}$. It can be seen that such a radiative adjustment brings the actual q_*/θ_{v*} into the surface fog regime during most of the period for which the cloud base was at the surface.

This calculation indicates that radiation cooling, and the corresponding turbulence production it effects at a stratus top, cools the atmosphere and propagates the cloud top upward and cloud base downward. The effective region over

STRATUS LOWERING CASE

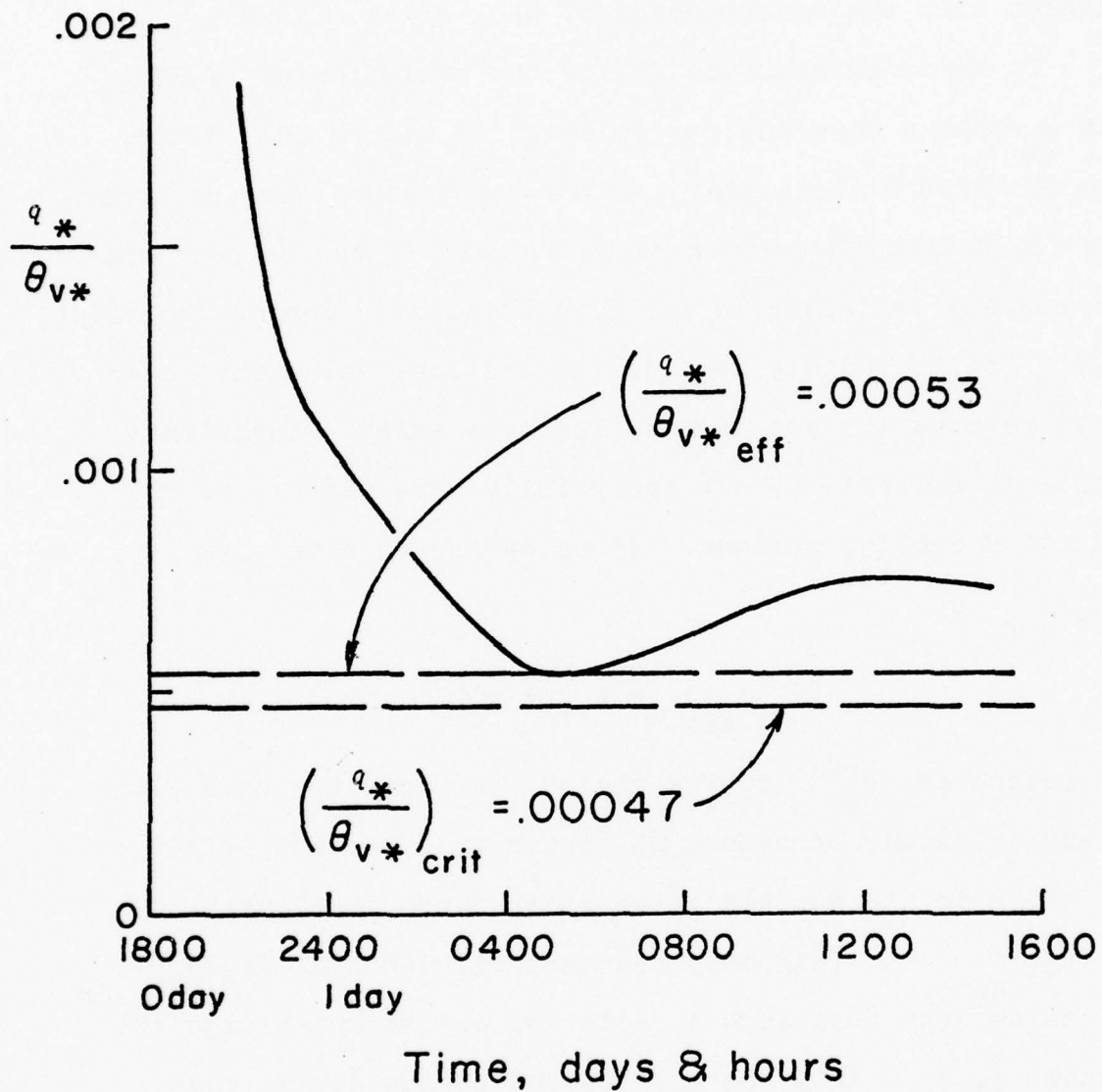


Figure 19. The evolution of q_*/θ_{v*} for a stratus lowering fog. Correction of (q_*/θ_{v*}) for radiation leads to $(q_*/\theta_{v*})_{\text{eff}}$ locating the lowered stratus in the warm-surface fog regime of Fig. 1.

which the cloud base may be propagated away from the top by turbulence production at the top during the nocturnal period is determined by the long wavelength radiation absorption length and by the turbulent scale length over which turbulence may be diffused downward from the top to the base. For these typical stratus conditions used as the basis of the calculation, we find the region to be 350 m (Figure 13). The empirical observation that the downward propagating stratus base can reach the ground during nocturnal cooling if the cloud top is at 400 m or lower is quite consistent with this result.

8. Concluding Remarks

The interaction between turbulent and radiative transport in the development of low level cloud and fog has been explored using a second-order closure model of turbulence. We find that existence criteria for turbulent dominated surface fog may be established on the basis of a critical turbulent humidity to heat flux ratio. Thermal radiation is shown to play a significant role in such atmospheric fog and stratus cloud events. Illustrations of the dynamics of a turbulent, radiatively coupled low level atmosphere for warm water fog and subsidence capped stratus show consistent quantitative features found in observations of such fog and cloud. Inversion heights with cloud in the boundary layer are predicted to have maxima in early morning and minima in late afternoon in contrast to the diurnal behavior of inversion heights in a dry boundary layer. Stratus is shown to propagate both downward and upward during nocturnal cooling periods under the influence of the radiant/turbulent driving mechanism located in the cloud top. If the late afternoon inversion height is low enough, the stratus is predicted to reach the surface.

The important effect of the large difference between solar and terrestrial radiative absorption coefficients for liquid drops on the turbulent behavior of cloud and fog is made manifest in these illustrations. That disparity in radiative interaction is one of those small but vital differences characteristic of the planet. It is somewhat akin to the

density maximum of water at 4°C which allows ice to float and thus has enormous implications for bodies of water on the earth's surface. If the solar and terrestrial radiation absorption lengths bore the opposite relationship to one another, cloud tops would be heated by the sun while the cloud interiors cooled to space leading to stabilization and the cessation of turbulence production by the cloud top cooling mechanism. Evaporation of the cloud interior down to the base would be delayed until radiative "burning away" of the stratus progressed downward devoid of the mixing influence of turbulent transport. Cloud structure and cloud dynamics would be significantly altered and, we imagine, so too would our atmosphere.

REFERENCES

- Ball, F.K., 1960: Control of inversion height by surface heating. *Quart. J. Roy. Meteor. Soc.*, 86, 483.
- Burk, S.D., 1977: The moist boundary layer with a higher order turbulence closure model. *J. Atmos. Sci.*, 34, 629-638.
- Charnock, H., 1974: Wind stress on a water surface. *Quart. J. Meteor. Soc.*, 81, 639-640.
- Donaldson, C.duP., 1973: Atmospheric turbulence and the dispersal of atmospheric pollutants. *AMS Workshop on Micro-meteorology*, Boston, 313-390, EPA-R4-73-016a.
- Feigel'son, E.M., 1964: *Light and Heat Radiation in Stratus Clouds*. Moscow, Nauka, 245 pp. (English translation by Israel Program for Scientific Translation, 1966.)
- Feigel'son, E.M., 1970: *Radiant Heat Transfer in a Cloudy Atmosphere*. Leningrad, Gidrometeor., 191 pp. (English translation by Israel Program for Scientific Translation, 1973.)
- Goody, R.M., 1964: *Atmosphere Radiation*. Clarendon Press, 436 pp.
- Leipper, D.F., 1948: Fog development at San Diego, California. *Sears. Found. Journ. Mar. Res.*, 337-346.
- Lewellen, W.S., 1977: Use of invariant modeling, *Handbook of Turbulence*. New York, Plenum Publishers, 237-290.
- Lewellen, W.S., and M.E. Teske, 1973: Prediction of the Monin-Obukhov similarity functions from an invariant model of turbulence. *J. Atmos. Sci.*, 30, 1340-1345.
- Lewellen, W.S., and M.E. Teske, 1975: Development of a low-level atmospheric turbulence model for marine environments. *A.R.A.P. Report No. 255*, Aeronautical Research Associates of Princeton, Inc.
- Lewellen, W.S., M.E. Teske, and C.duP. Donaldson, 1974: Turbulence model of diurnal variations in the planetary boundary layer. *Proc. 1974 Heat Trans. and Fluid Mech. Inst.*, Stanford, California, 301-319.
- Lilly, D.K., 1968: Models of cloud-topped mixed layers under a strong inversion. *Quart. J. Roy. Meteor. Soc.*, 94, 292-309.
- Lumley, J.L., and B. Khajeh-Nouri, 1974: Computational modeling of turbulent transport. *Advances in Geophysics*, 18A, New York, Academic Press.

- Mack, E.J., U. Katz, C. Rogers, and R. Piliè, 1974: The microstructure of California coastal stratus and fog at sea. Calspan Report CJ-5405-M-1, Calspan Corp., Buffalo, New York.
- Mack, E.J., R. Piliè, and W.C. Kockmond, 1973: An investigation of the microphysical and micrometeorological properties of sea fog. Calspan Report CJ-5237-M-1, Calspan Corp., Buffalo, New York.
- Manabe, S., and R.F. Strickler, 1964: On the thermal equilibrium of the atmosphere with a convective adjustment. *J. Atmos. Sci.*, 21, 361-385.
- Mellor, G.L., 1973: Analytic prediction of the properties of stratified planetary surface layers. *J. Atmos. Sci.*, 30, 1061-1069.
- Mellor, G.L., 1977: The Gaussian cloud model relations. *J. Atmos. Sci.*, 34, 356-358.
- Mellor, G.L., and T. Yamada, 1974: A hierarchy of turbulence closure models for planetary boundary layers. *J. Atmos. Sci.*, 31, 1791-1806.
- Neiburger, M., 1944: Temperature changes during formation and dissipation of West Coast stratus. *J. Meteor.*, 1, 29-41.
- Neiburger, M., D.S. Johnson, and C. Ehnien, 1961: Studies over the Eastern Pacific Ocean in summer, I, The inversion over the Eastern North Pacific Ocean. *Univ. Calif. Publ. in Meteor.*, 1.
- Randall, D., 1976: The interaction of the planetary boundary layer with large-scale circulations. Ph.D. thesis, U.S.L.A., Department of Atmospheric Sciences, Los Angeles, California.
- Schubert, W.H., 1976: Experiments with Lilly's cloud-topped mixed layer model. *J. Atmos. Sci.*, 33, 436-446.
- Sommeria, G., 1976: Three-dimensional simulation of turbulent processes in an undisturbed trade wind boundary layer. *J. Atmos. Sci.*, 33, 216-241.
- Sommeria, G., and J.W. Deardorff, 1977: Subgrid-scale condensation in models of nonprecipitating clouds. *J. Atmos. Sci.*, 34, 344-355.
- Taylor, G.I., 1917: The formation of fog and mist. *Quart. J. Roy. Meteor. Soc.*, 43, 241-268.
- Wu, J., 1969: Froude number scaling of wind-stress coefficients. *J. Atmos. Sci.*, 26, 408-413.
- Wyngaard, J.C., O.R. Coté, and K.S. Rao, 1974: Modeling the atmospheric boundary layer. *Advances in Geophysics*, 18A, New York, Academic Press.

APPENDIX B

COMPARISON OF THE A.R.A.P. SECOND-ORDER CLOSURE MODEL WITH MEASUREMENTS IN A MARINE BOUNDARY LAYER[†]

We now compare the predictions of the A.R.A.P. second-order closure model with measurements of the fluid dynamic behavior of a marine boundary layer. A carefully studied data case to be used as the basis of the comparison is that of Pennell and LeMone for the trade-wind boundary layer (Pennell and LeMone, 1974). These measurements were taken for the mean profiles of velocity, temperature and water mixing ratio and the corresponding turbulent stress, heat flux and moisture flux fields. A full comparison of the A.R.A.P. predictions of the dynamics and evolution of the boundary layer would require measurements of the fluid state at an initial time and at some subsequent time. Unfortunately such sequential measurements are not presently available. We are thus only able to provide a verification of the consistency of the A.R.A.P. model in the sense that the turbulence co-existing with the measured mean profiles is well-represented by the turbulence correlations predicted by the A.R.A.P. model and based upon the measured mean profiles. A more complete verification of the A.R.A.P. model must await the availability of turbulence and mean profile data taken over several different time levels.

In Figs. 1 to 3 we indicate the mean profiles of velocity, temperature, and total water mixing ratio taken from Pennell and LeMone (1974) and Sommeria-Klein and LeMone (1977) for the NCAR, Puerto Rico experiment. The data points were used as initial conditions for the A.R.A.P. predictions. The sea surface temperature was held fixed at 25.9°C. The reference time of 1200 hours denotes that the solar radiation input corresponds to starting the calculation at noon. The mean profiles evolve relatively slowly until significant cloudiness sets in after approximately four hours. The consistency of the model predictions can be checked by comparing the turbulent flux profiles during this slow evolution of the mean profiles with those measured concurrently with the mean profiles. Figure 4 shows the variation in the shear stress over a five hour simulation period. In the mixed layer the predictions agree quite well with the measurements. Note, in particular, that the model has no adjustable input at the surface. The effective surface roughness depends internally upon the predicted \overline{uw} . Thus the agreement of the surface value with the data is an important achievement for the model. There is some discrepancy between the observations and predictions at the top of the mixed layer where an undershoot is predicted but not observed. The undershoot intensifies when clouds develop.

In Fig. 5 we show the same shear stress profiles but also include a predicted result for this case based on the NCAR subgrid

[†]These comparisons were made by Owen Coté while on leave from Staff Meteorology, Air Force Systems Command, Hamscom AFB, Bedford, Mass.

turbulence model (Sommeria-Klein and LeMone, 1977). It can be seen that their model also predicts an undershoot which increases with cloud activity.

In Fig. 6 the vertical velocity variance is shown. There is general agreement between both model predictions and the data in the mixed layer below 600 m altitude. The character of the A.R.A.P. prediction and the NCAR prediction above the mixed layer is similar in that both show a strong increase in σ_w as clouds develop.

The virtual potential temperature flux is shown in Fig. 7. Again, there is quantitative agreement between both predictions and the data in the mixed layer and qualitative agreement between the two predictions above the mixed layer.

As discussed in Section 3.1 the biggest discrepancy between the NCAR model results and the A.R.A.P. results is the prediction of liquid water content after the clouds develop. There is from 1 to 2 orders of magnitude difference in the predicted value of average liquid water content. This difference remains to be resolved.

Similar calculations for comparison with data from GATE day September 15 (LeMone, 1977) have also been made. The results of this comparison were quite similar to the ones shown here for the Puerto Rico case but with somewhat more scatter in the data. We show the fluxes of momentum, temperature and water vapor in Figs. 8 and 9.

We reiterate that these comparisons can only be used to show a general consistency of the model. The comparisons cannot be used to make a careful assessment of the accuracy of the model. This will necessitate a more detailed specification of the experimentally-observed boundary conditions.

References

- LeMone, M.A. 1977. Private Communication.
- Pennel, W.T., and LeMone, M.A. 1974. "An experimental study of turbulence structure in the fair-weather trade wind boundary layer. *J. Atmos. Sci.* 31, 1308-1323.
- Sommeria-Klein, and LeMone, M.A. 1977. "Direct testing of a 3-D model of the planetary boundary layer against experimental data," Unpublished manuscript.

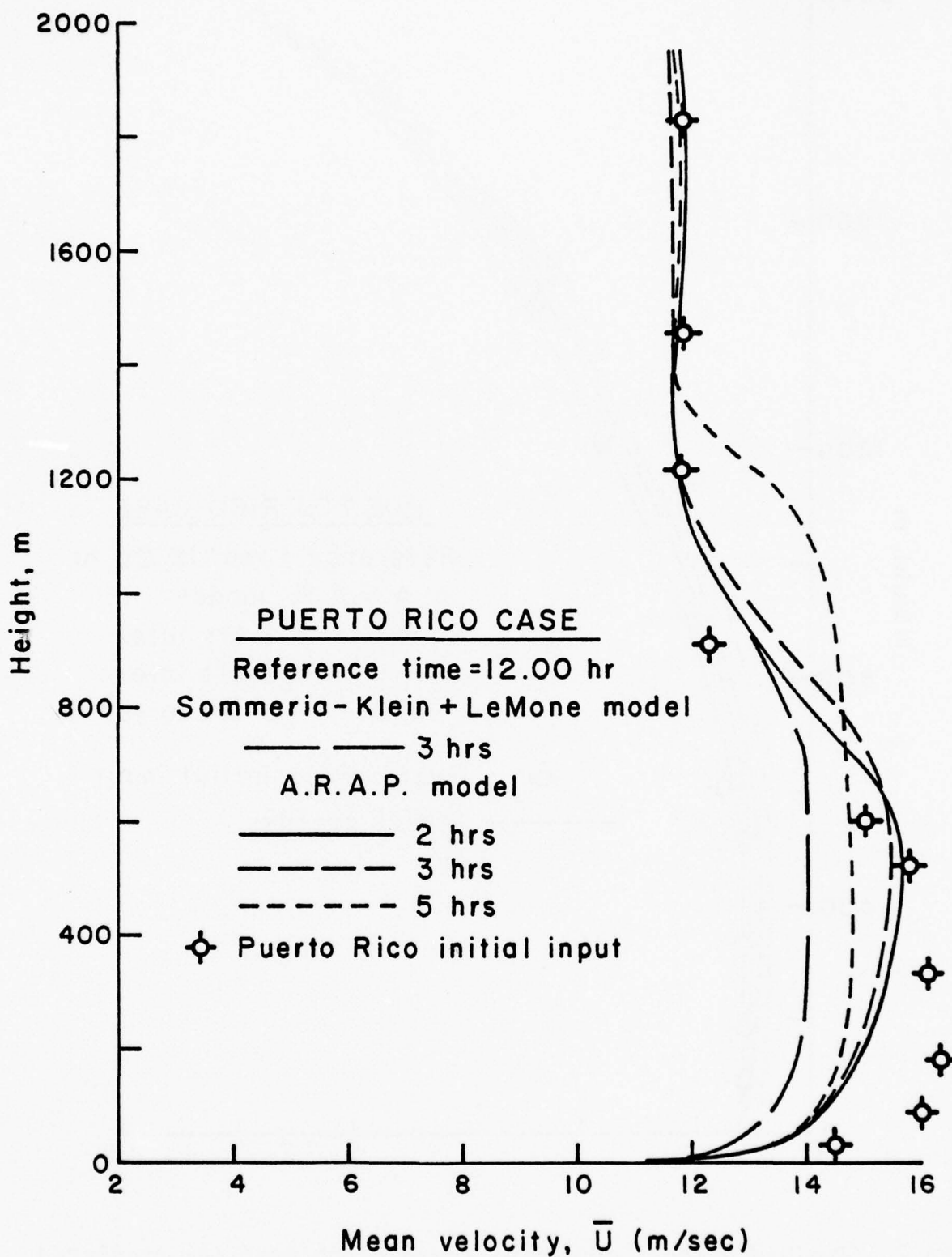


Figure 1. Evolved mean profiles of velocity according to the A.R.A.P. model and the model of Sommeria-Klein. Initialization of the models is for the mean velocity measurements shown as Puerto Rico initial input.

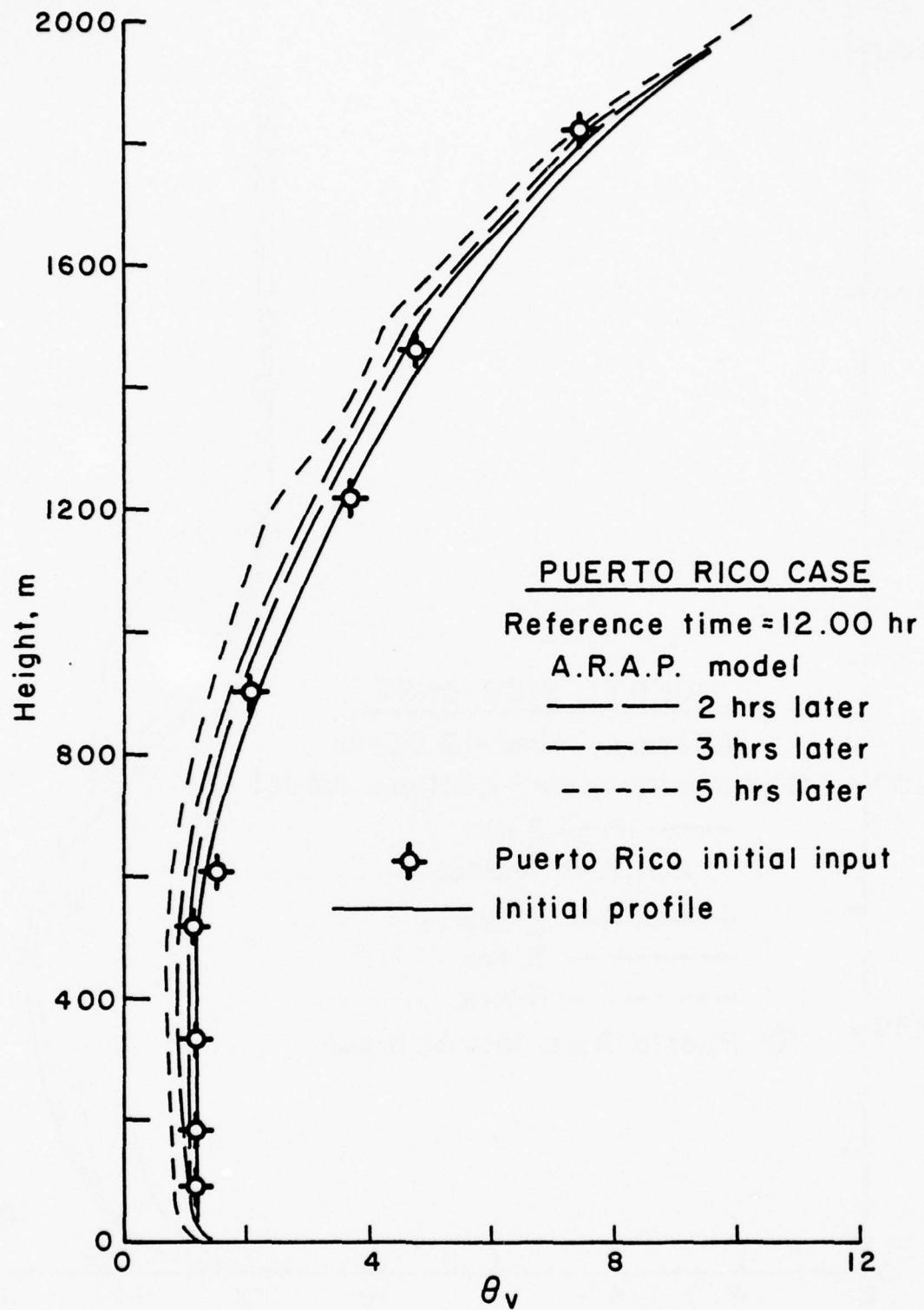


Figure 2. Evolved virtual potential temperature profiles predicted by the A.R.A.P. model for the conditions of Fig. 1.

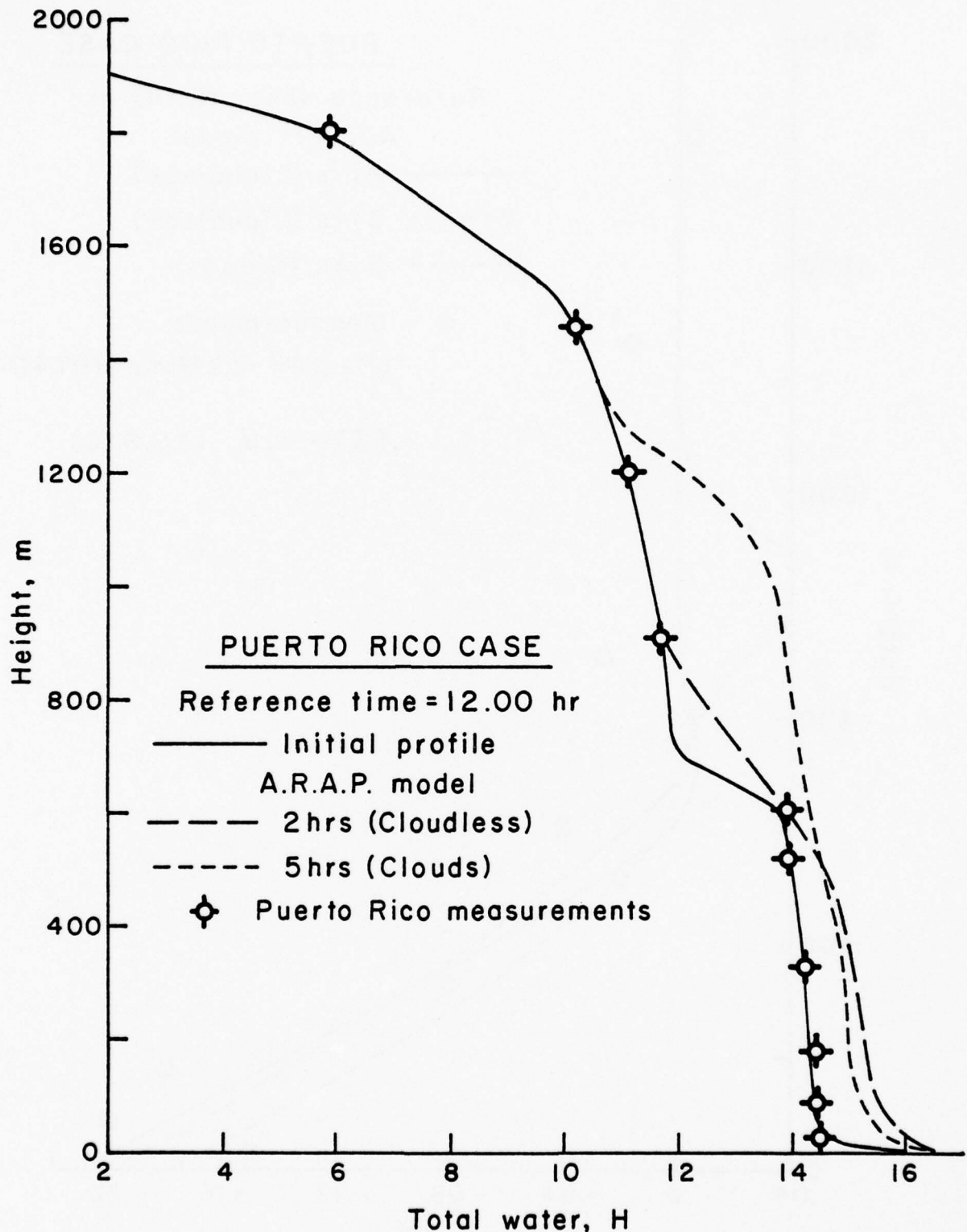


Figure 3. Typical mean profile (total water mixing ratio) taken from the measurements of Pennell and LeMone and used as an initial condition for the A.R.A.P. model (solid line). Subsequent evolution of the mean total water mixing ratio is shown at 2 hrs and 5 hrs after initialization as predicted by the A.R.A.P. model. After 5 hrs, clouds have appeared in the modeled boundary layer.

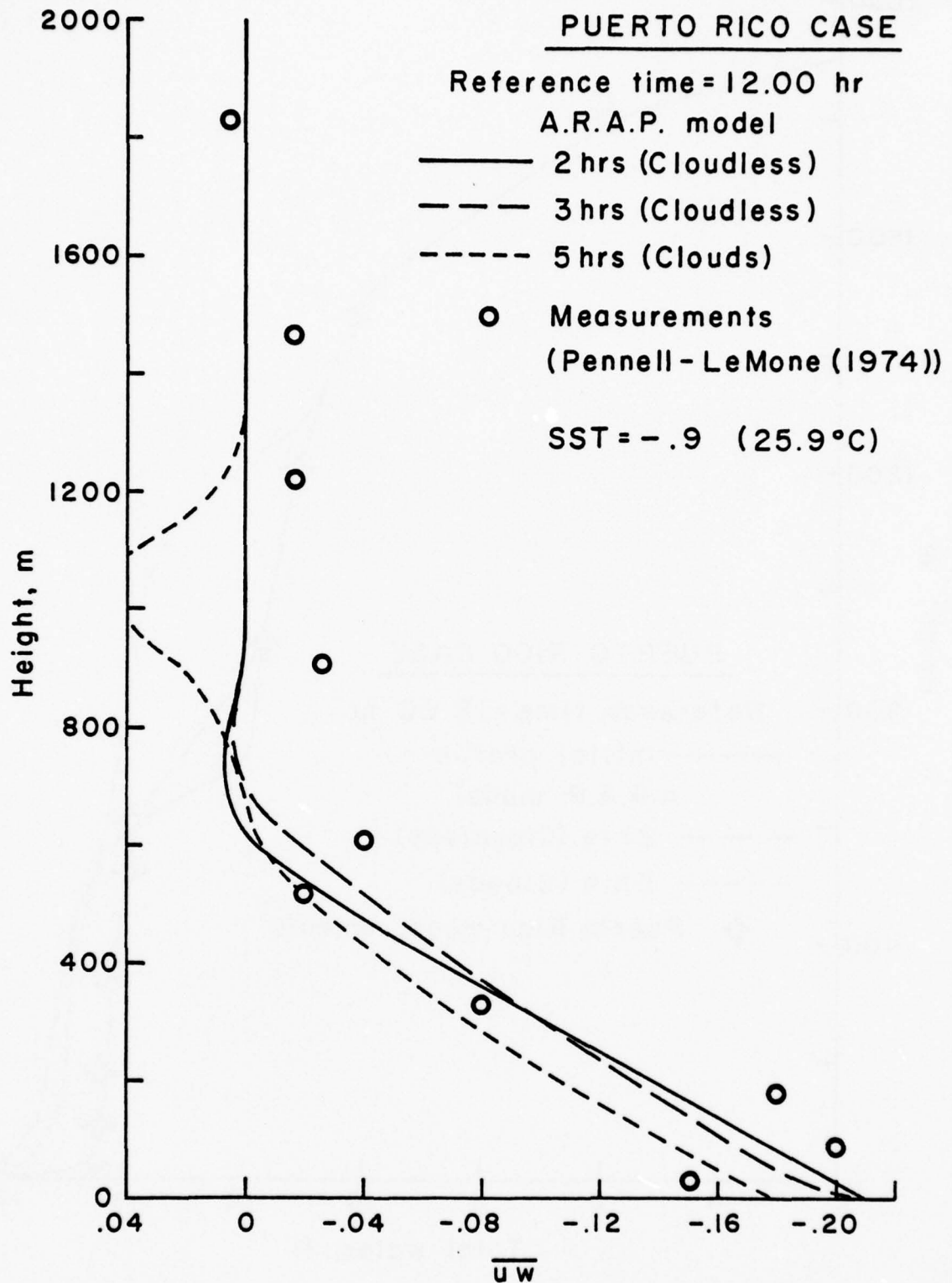


Figure 4. Predicted and measured longitudinal momentum flux. Measurements correspond to the initial conditions of the prediction. Note clear prediction of the slight undershoot cloud-free state and the strong undershoot with the cloud present after 5 hrs.

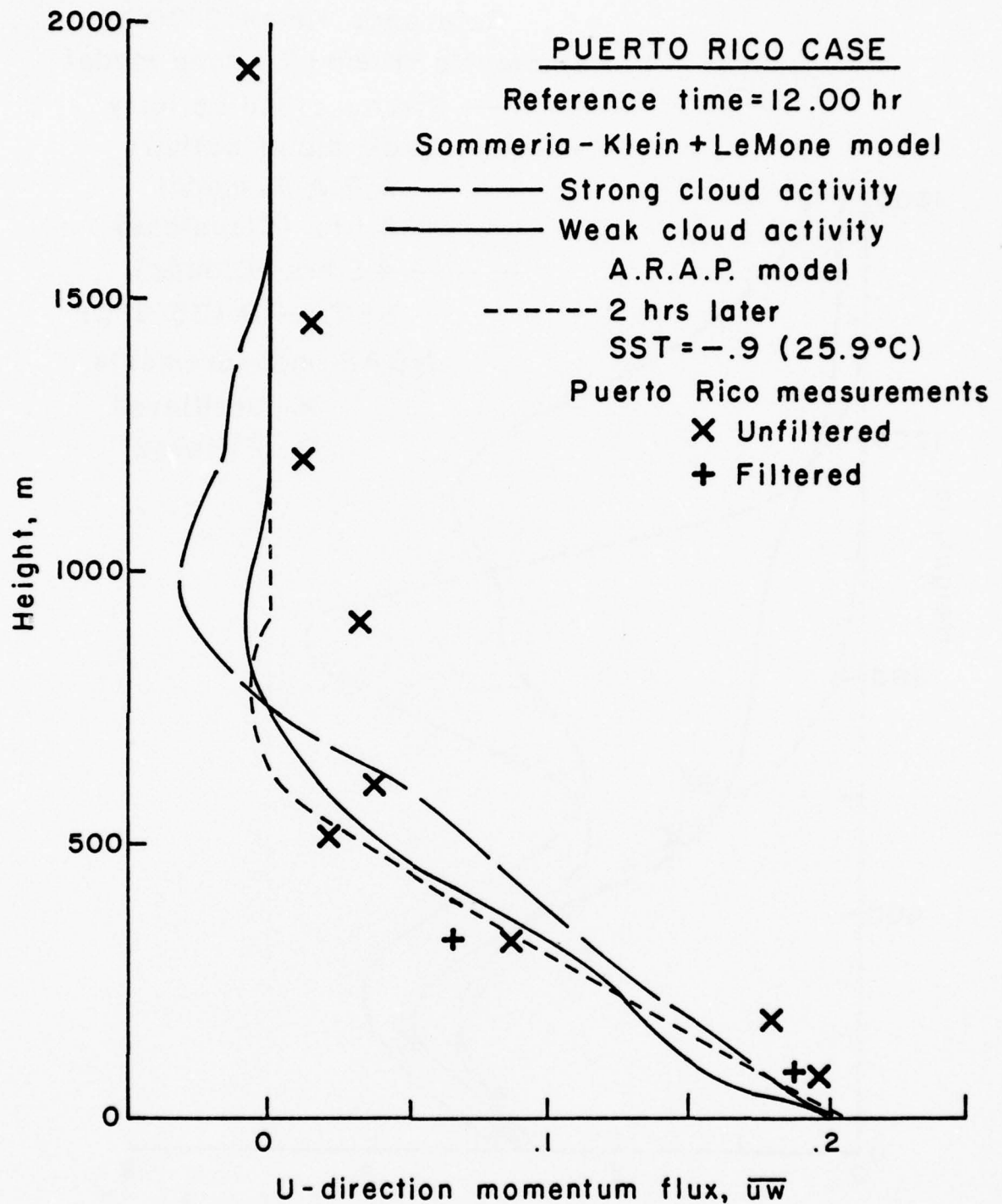


Figure 5. Comparison of measured longitudinal momentum flux with the A.R.A.P. model predictions and the subgrid turbulence model predictions of Sommeria-Klein and LeMone.

PUERTO RICO CASE

Reference time = 12.00 hr

Sommeria - Klein + LeMone model

— Strong cloud activity

— Weak cloud activity

A.R.A.P. model

----- 3 hrs (Cloudless)

- - - 4.5 hrs (Clouds)

SST = -.9 (25.9°C)

NCAR measurements

X Unfiltered

+ Filtered

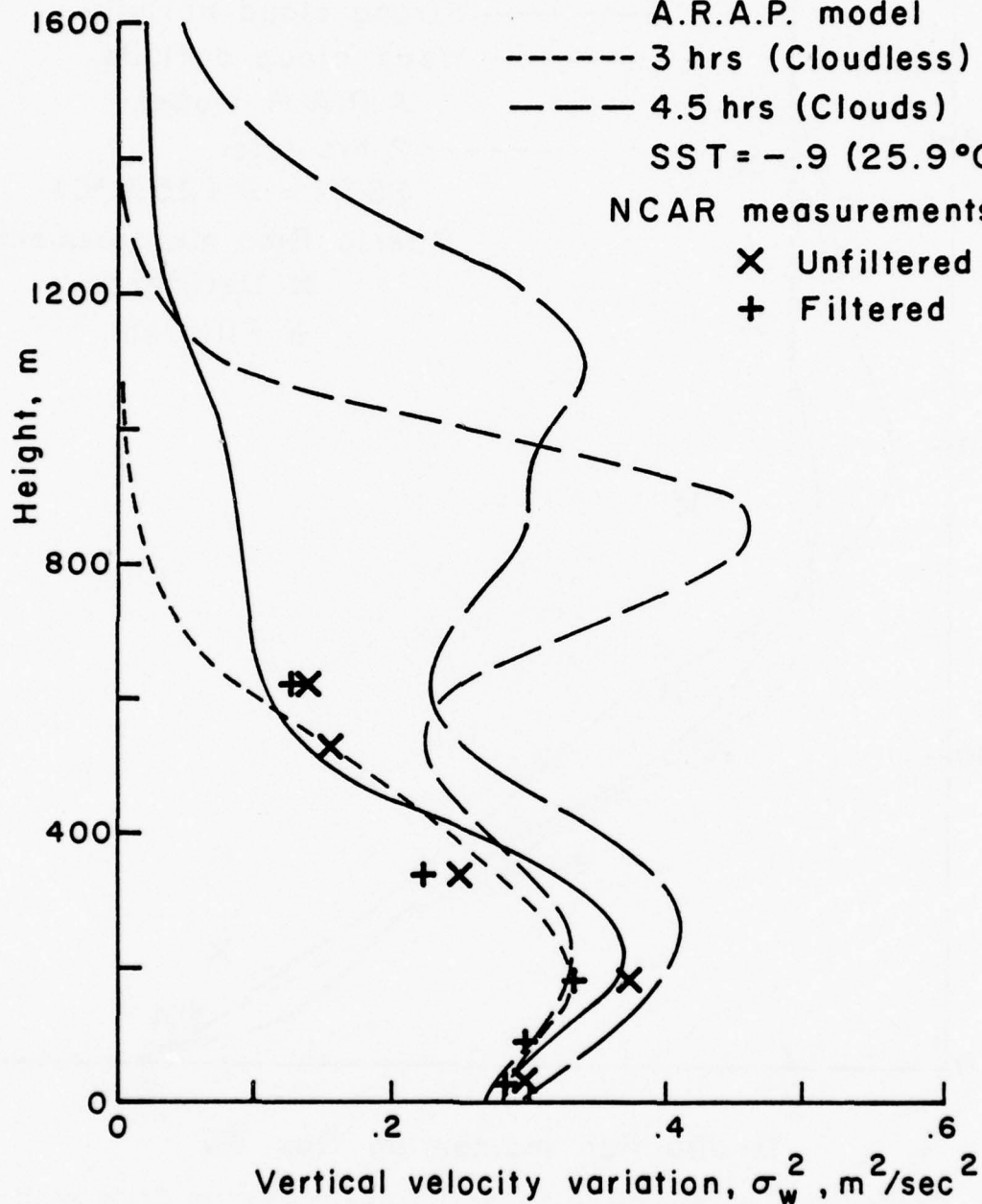


Figure 6. Vertical velocity variance predicted by the A.R.A.P. model, predicted by the model of Sommeria-Klein, and the NCAR 1972 Puerto Rico measurements.

PUERTO RICO CASE

Reference time=12.00 hr

Sommeria-Klein + LeMone model

—— Strong cloud activity

—— Weak cloud activity

A.R.A.P. model

----- 3 hrs later

- - - - 4.5 hrs later

SST= -0.9 (25.9°C)

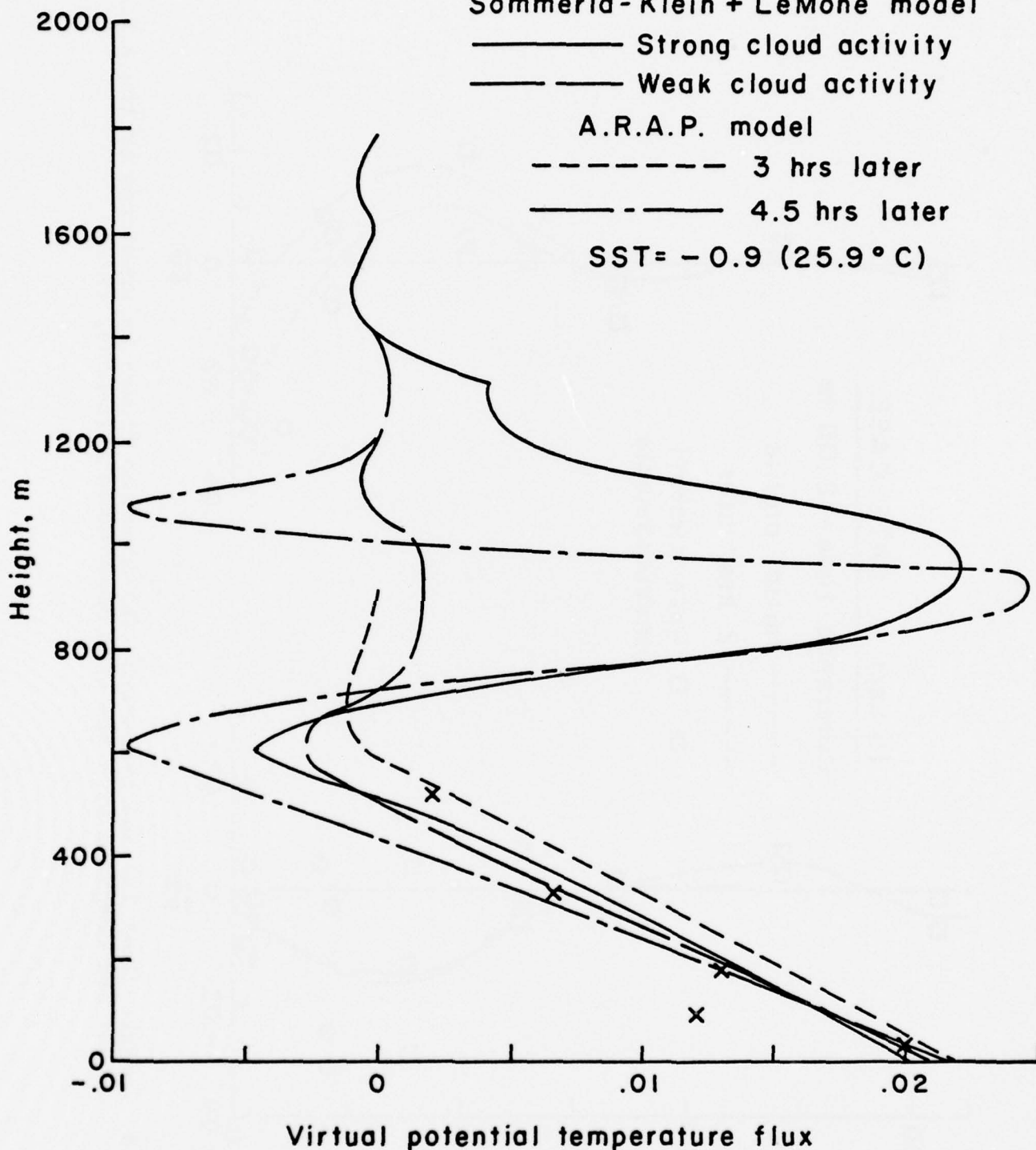


Figure 7. Virtual potential temperature-velocity correlations as predicted by the A.R.A.P. model, the model of Sommeria-Klein, and compared with the NCAR 1972 Puerto Rico measurements.

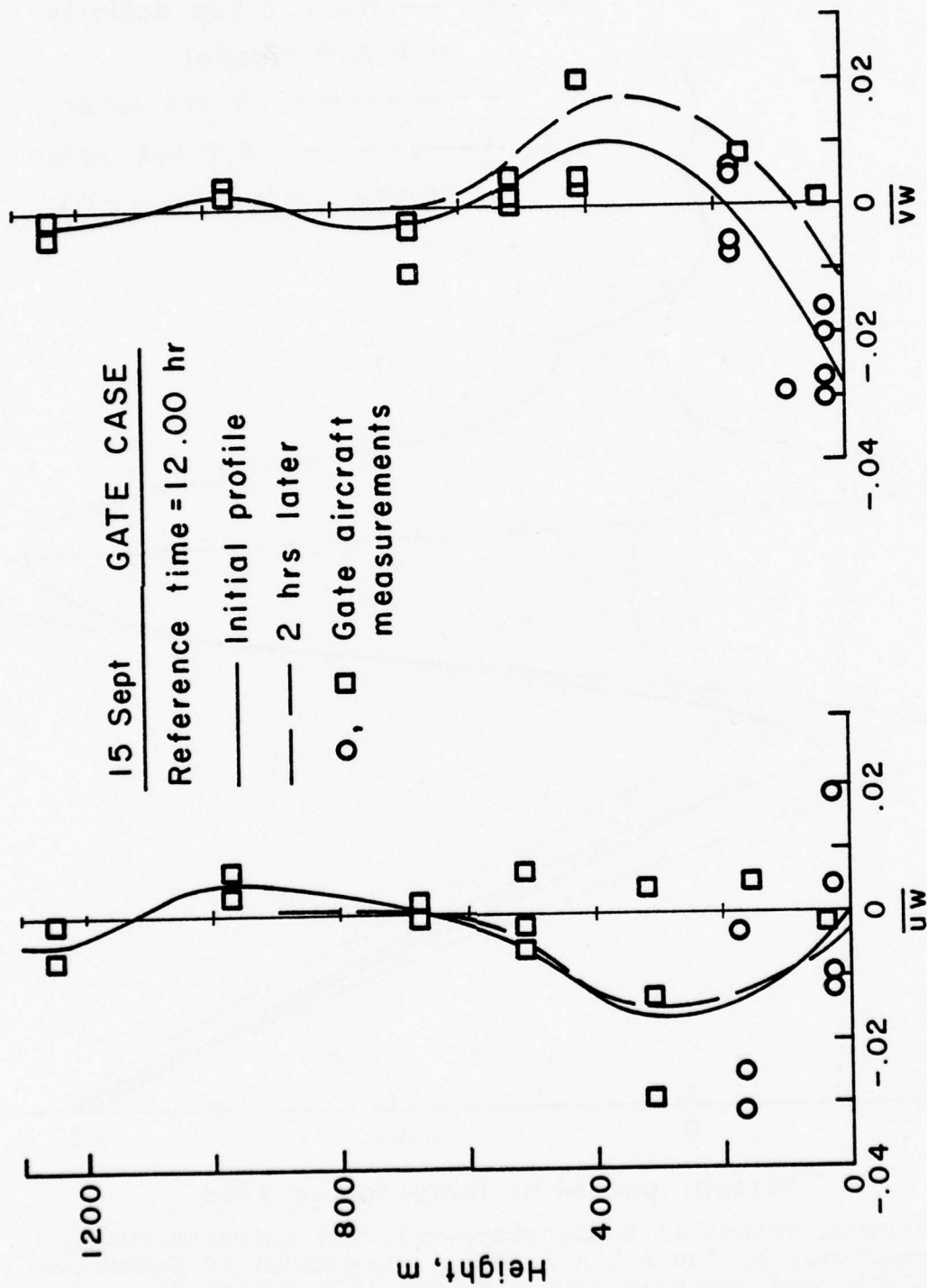
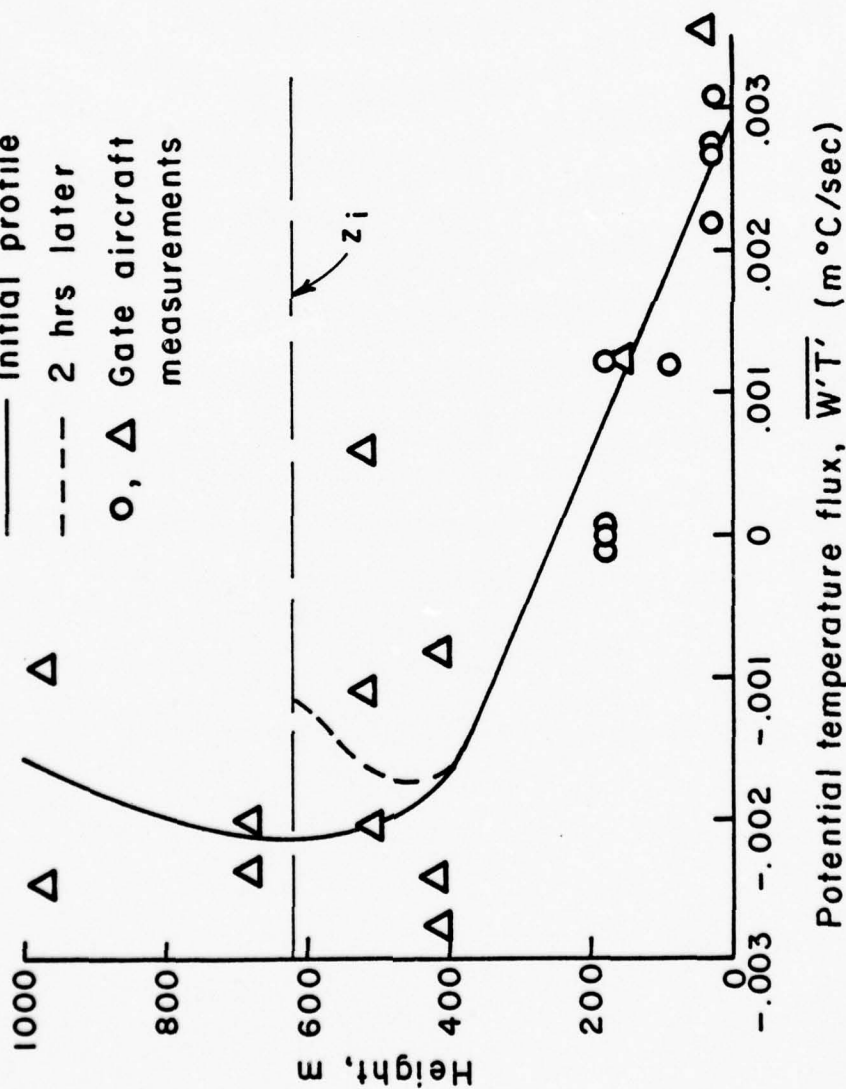


Figure 8. Longitudinal (a) and transverse (b) momentum fluxes as predicted by the A.R.A.P. model and compared with the GATE measurements (LeMone, 1977).

15 Sept GATE CASE
Reference time = 12.00 hr

— Initial profile
--- 2 hrs later
O, Δ Gate aircraft
measurements



B-11

Figure 9. Virtual potential temperature and humidity fluxes as predicted by the A.R.A.P. model and compared with the GATE measurements (LeMone, 1977).

APPENDIX C

ANALYSIS OF A FRONT MOVING IN THE PLANETARY BOUNDARY LAYER

by

H. Segur

The occurrence of atmospheric fronts in the mid-latitudes is a common meteorological event. These fronts, which carry with them relatively sharp temperature discontinuities, exist both on a synoptic scale (e.g., polar fronts) and on much smaller scales (e.g., thunderstorm gust fronts and sea breeze fronts). During the period of the present contract, we have begun to study the detailed local structure of an atmospheric front, using a combination of analytical and computational methods. In this section, we present some of our preliminary results.

On a cyclonic scale, the development of warm and cold fronts was studied numerically by Kasahara, Isaacson and Stoker (1965), using a two-layer model of an incompressible atmosphere on a rotating earth, with a β -plane approximation. Their model had two (horizontal) space dimensions, and they assumed hydrostatic pressure in the vertical direction. Further, they ignored the dynamics of the upper layer. The result was a credible description of the horizontal motion of these fronts, on a cyclonic scale. They did not discuss the local structure of the surface front, which requires a separate analysis. Some of the motivation for the present study is to provide a description of this local structure, to complement their description of the large-scale dynamics.

A numerical study of the fronts associated with a thunderstorm gust front (Teske and Lewellen, 1977) is described in Section 3.2 of this report. A major difference between these two kinds of fronts is that Coriolis forces, which have a dominant effect on the cyclonic scale, are relatively unimportant for this application. In either case, there is a need for a local description near the surface front.

A. A Simplified Analytical Model (without Coriolis forces)

We consider the two-dimensional motion of two layers of incompressible fluid, moving under gravity on a horizontal surface, as shown in Fig. 1. Here $h(y,t)$ is taken as the height of the front and $H(y,t)$ may be taken as the height of the tropopause. To make this first model as simple as possible, we neglect Coriolis forces. This creates no problems for the thunderstorm gust front, but does limit the range validity of the analysis when applied to a cold front. We return to this

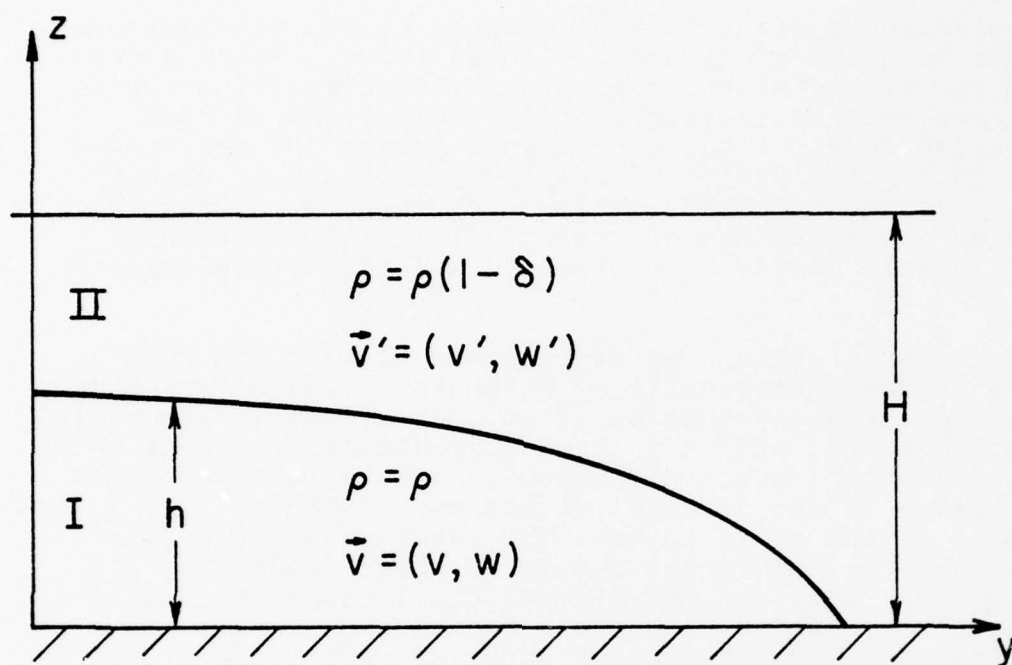


Figure 1. Coordinate system for a cold front.

point below, and discuss the circumstances in which these results may be applied to the motion of a cold front. The relevant equations of motion are (in Fluid I):

$$\frac{\partial v}{\partial y} + \frac{\partial w}{\partial z} = 0 \quad , \quad (1)$$

$$\frac{\partial v}{\partial t} + v \frac{\partial v}{\partial y} + w \frac{\partial v}{\partial z} + \frac{1}{\rho} \frac{\partial p}{\partial y} = \frac{\partial \tau_1}{\partial z} + \frac{\partial \tau_2}{\partial y} \quad (2)$$

(in Fluid II):

$$\frac{\partial v'}{\partial y} + \frac{\partial w'}{\partial z} = 0 \quad (3)$$

$$\frac{\partial v'}{\partial t} + v' \frac{\partial v'}{\partial y} + w' \frac{\partial v'}{\partial z} + \frac{1}{\rho(1-\delta)} \frac{\partial p'}{\partial y} = \frac{\partial \tau'_1}{\partial z} + \frac{\partial \tau'_2}{\partial y} \quad , \quad (4)$$

where τ_j refers to the shear stress, including both laminar and turbulent terms. A fundamental assumption of this analysis is that the pressure is purely hydrostatic. Thus, we assume the pressure is constant above $z = H(y, t)$; in fluid II,

$$p' = g\rho(1-\delta) (H(y, t) - z) + p_0 \quad ; \quad (5)$$

and in Fluid I,

$$p = g\rho(1-\delta) (H(y, t) - h(y, t)) + g\rho(h(y, t) - z) + p_0 \quad .(6)$$

The validity of this assumption is discussed at relevant points below.

The vertical velocity vanishes at the ground ($z = 0$). At the interface ($z = h$) and free surface ($z = H$) there are kinematic conditions,

$$\frac{\partial H}{\partial t} + v' \frac{\partial H}{\partial y} = w' \quad , \quad \text{on } z = H(y, t) \quad , \quad (7)$$

$$\left. \begin{aligned} \frac{\partial h}{\partial t} + v' \frac{\partial h}{\partial y} &= w' \\ \frac{\partial h}{\partial t} + v \frac{\partial h}{\partial y} &= w \end{aligned} \right\} \quad \text{on } z = h(y, t) \quad . \quad (8)$$

We anticipate that the shear stress will be negligible outside of this boundary layer along the ground and near the interface, and neglect (τ_2, τ'_2) . If we integrate Eqs. (1) and (2) in the z -direction, making use of the other equations, the final result may be written as

$$\left. \begin{aligned}
 & \frac{\partial h}{\partial t} + \frac{\partial}{\partial y} \int_0^h v dz = 0 \\
 & \frac{\partial}{\partial t} \int_0^h v dz + \frac{\partial}{\partial y} \int_0^h v^2 dz + gh \left[(1-\delta) \frac{\partial H}{\partial y} + \delta \frac{\partial h}{\partial y} \right] = \tau_i - \tau_g \\
 & \frac{\partial}{\partial t} (H-h) + \frac{\partial}{\partial y} \int_h^H v' dz = 0 \\
 & \frac{\partial}{\partial t} \int_h^H v' dz + \frac{\partial}{\partial y} \int_0^h (v')^2 dz + g(H-h) \frac{\partial H}{\partial y} = -\tau_i
 \end{aligned} \right\} (9)$$

where τ_i is the stress at the interface, and τ_g is that at the ground. The only approximations made to this point are the hydrostatic approximation and the neglect of $(\partial \tau / \partial y)$.

We consider first the case in which we may neglect shear stress altogether. Then the only force is the hydrostatic pressure, which introduces no z -variation in v (from (2), (4)). Thus, $\partial v / \partial z$ vanishes if it did initially. Equations (9) then reduce to

$$\left. \begin{aligned}
 & \frac{\partial h}{\partial t} + \frac{\partial}{\partial y} (vh) = 0 \\
 & \frac{\partial v}{\partial t} + v \frac{\partial v}{\partial y} + g(1-\delta) \frac{\partial H}{\partial y} + g\delta \frac{\partial h}{\partial y} = 0 \\
 & \frac{\partial (H-h)}{\partial t} + \frac{\partial}{\partial y} (v'(H-h)) = 0 \\
 & \frac{\partial v'}{\partial t} + \frac{\partial v'}{\partial y} + g \frac{\partial H}{\partial y} = 0
 \end{aligned} \right\} (10)$$

For atmospheric applications, δ is relatively small (typically less than about 0.07).

The steady-state version of this model was used by Yih and Guha (1955) in a theoretical-experimental study of internal hydraulic jumps. They found good agreement when δ was moderately large (~ 0.20). For $\delta = 0.05$, the jumps predicted were about 30 percent larger than those observed; no more than 10 percent of this discrepancy could be attributed to scatter in their experimental data. It appears that this discrepancy is a measure of the validity of the hydrostatic pressure approximation.

The system of Eqs. (10) is hyperbolic, having four real characteristics. Two of these correspond to motion in which the whole system responds like a homogeneous fluid. In an atmosphere without shear ($v = v'$), for small δ , these speeds are given by

$$\frac{dy}{dt} = v \pm \sqrt{gh} \quad (11)$$

Further, in these two modes, disturbances satisfy

$$\Delta(v' - v) = 0, \quad \Delta\left(h - \frac{h_0}{H_0} H\right) = 0 \quad (12)$$

so that the density discontinuity at $z = h$ has no effect to leading order in δ . If we take the height of the tropopause as 9 km, propagation speeds for this mode are on the order of 200 m/sec, much faster than observed speeds of atmospheric fronts.

The other two modes of the system (10) correspond to waves traveling along $z = h$, and these are of more interest in the present study. To leading order in δ (with $v = v'$), the characteristics are defined by

$$\frac{dy}{dt} = v \pm \sqrt{\frac{g\delta h(H-h)}{H}} \quad (13)$$

and disturbances in this mode satisfy

$$\Delta H = 0 \quad (14)$$

Thus, to leading order, the tropopause does not feel the motion of the front, and the upper fluid plays a relatively passive role. In a stationary atmosphere ($v = v' = 0$) with a relative density (or temperature) discontinuity of 0.05 at a height of 500 m, wave propagation speeds in this mode are on the order of 15 m/sec, which is in rough agreement with observed propagation speeds of fronts. Thus, our primary interest is on these internal modes.

The model of Kasahara, et al., 1965, is consistent with (10) except that they also included (and were primarily interested in) Coriolis effects. We will see below that (10) is

a valid approximation to their model for phenomena that occur over a few minutes (i.e., for times very much shorter than a rotation period of the earth). They also assumed that the dynamics of the upper fluid could be neglected. Some justification for this assumption can be inferred from the fact that the tropopause responds only weakly to motion of the front, according to (14). This additional assumption reduces (10) to

$$\left. \begin{aligned} \frac{\partial h}{\partial t} + \frac{\partial}{\partial y} (vh) &= 0, \\ \frac{\partial v}{\partial t} + v \frac{\partial v}{\partial y} + g\delta \frac{\partial h}{\partial y} &= 0, \end{aligned} \right\} \quad (15)$$

which can be solved by characteristics, and which corresponds exactly to the equations of nonlinear shallow water waves, with a reduced gravity ($g\delta$).

Moreover, in this simplified model, the motion of a cold front corresponds to the motion of a wave of water advancing on a dry bed after a dam-break (cf., Fig. 2). This problem has a simple solution, given by Ritter (1892); for $-\sqrt{g\delta h_0} < y/t < 2\sqrt{g\delta h_0}$,

$$\left. \begin{aligned} v &= 2/3(\sqrt{g\delta h_0} + y/t), \\ \sqrt{g\delta h} &= 1/3(2\sqrt{g\delta h_0} - y/t), \\ w &= -2/3 z/t \end{aligned} \right\} \quad (16)$$

Dressler (1952) noted that the velocity of the tip of the forward wave, $2\sqrt{g\delta h_0}$, exceeded the observed velocities by as much as 40 percent (in water-air experiments, where $\delta = 1$). He argued that even though shear stress is negligible outside a "thin" boundary layer, that layer engulfs the fluid region near the tip, where h vanishes. Thus, the shear stress at the ground, which was dropped after (9), must be retained to model the motion of the front accurately. Dressler (1952) and Whitham (1955) used

$$\tau_g = K v^2, \quad (17)$$

where K is an empirical constant, so that (15) is replaced by

$$\left. \begin{aligned} \frac{\partial h}{\partial t} + \frac{\partial}{\partial y} (vh) &= 0 \\ \frac{\partial v}{\partial t} + v \frac{\partial v}{\partial y} + g\delta \frac{\partial h}{\partial y} + \frac{Kv^2}{h} &= 0 \end{aligned} \right\} \quad (18)$$

For $K \ll 1$, this additional term has little effect except near the tip (i.e., the surface front) where it is dominant.

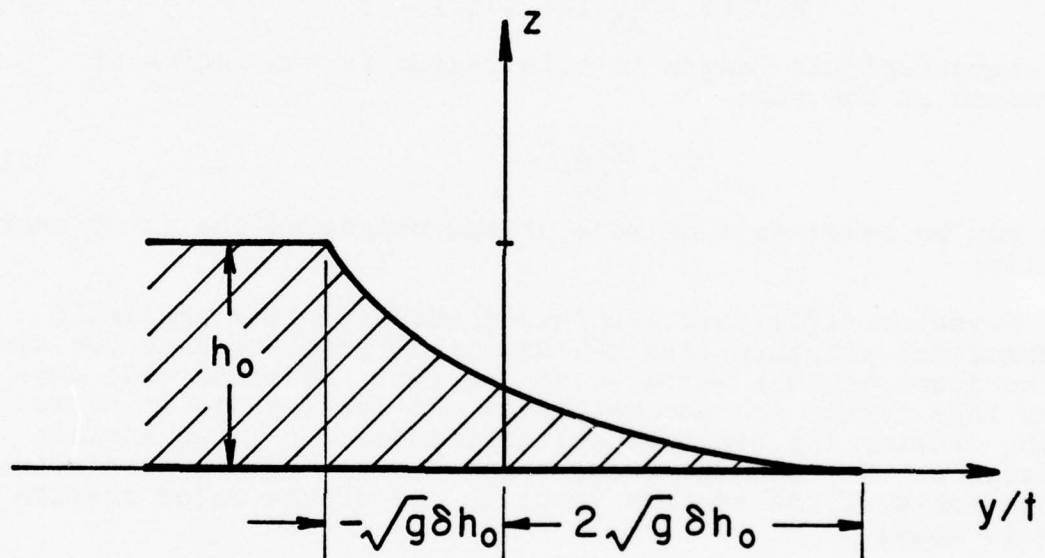
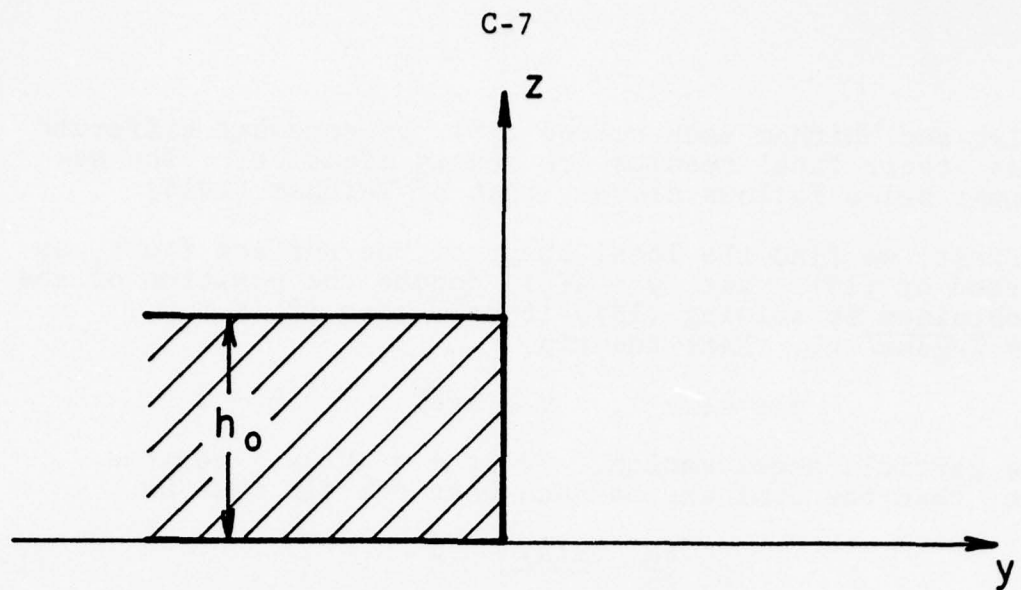


Figure 2. Idealized solution of the motion of a cold front after sudden release, without dissipation or Coriolis forces.

Dressler and Whitham each solved (18), by somewhat different methods; their final results are nearly identical. The development below follows closely that of Whitham (1955).

First, we find the local shape of the surface front, as predicted by (18). Let $y = a(t)$ denote the position of the tip obtained by solving (18); (recall that if $K = 0$, $a(t) = 2\sqrt{g\delta h_0} t$). Near the tip,

$$y \rightarrow a(t) \quad , \quad v \rightarrow \dot{a}(t) \quad , \quad h \rightarrow 0 \quad .$$

If the particle acceleration, $\partial v / \partial t + v \partial v / \partial y$, remains finite, then the dominant balance near the tip must be

$$g\delta \frac{\partial h}{\partial y} + \frac{K(\dot{a})^2}{h} \sim 0 \quad . \quad (19)$$

Thus, near $y = a(t)$,

$$h(y, t) \sim \frac{2K}{g\delta} (\dot{a})^2 (a(t) - y)^{1/2} \quad (20)$$

The characteristic length in this region is the radius of curvature at the tip:

$$\bar{h} = \frac{K(\dot{a})^2}{g\delta} \quad (21)$$

This may be taken as a measure of the height of the front near the tip.

Dressler (1952) had previously observed from available experimental evidence (for the dam-break problem) that the slope of the front becomes vertical at the tip. Equation (20) confirms this result and parameterizes the local shape in terms of the density (or temperature) difference, δ , the surface resistance, K , and the front speed, $\dot{a}(t)$. This prediction of the shape of the surface front is one of the major results of this model.

It might be appropriate to remind the reader at this point that (18), as well as whatever results may be derived from (18), are based on a hydrostatic pressure approximation, and that the results of Yih and Guha (1955) suggest that this approximation loses its validity as $\delta \rightarrow 0$. It follows that the current model should be more reliable when the temperature jump is stronger (provided that the Coriolis effects can still be neglected).

Even for strong fronts, however, vertical accelerations must be important wherever the slope of the front becomes vertical, as predicted at the tip by (20). Thus, the hydrostatic pressure approximation (obtained by neglecting vertical accelerations) must break down near the tip of the front, for

any δ . However, this objection applies with equal validity to the dam-break problem ($\delta = 1$). The success of the theory in that application suggests that the effect of this breakdown may not be too severe.

Next, we need to determine the tip velocity, $\dot{a}(t)$. Whitham (1955) argued that (16) applies except in a region near the tip, where h is too small to neglect the resistance term in (18), (cf., Fig. 3). Within this dissipative region, ($\xi(t) < y < a(t)$), the velocity is assumed to be constant (in y). The mass flux into this region is

$$\dot{M} = \frac{dM}{dt} = \rho h_1 (V - \dot{\xi}) \quad ; \quad (22)$$

where $h_1(t)$ is the height of the front at $y = \xi(t)$, where we will match to (16). From (16),

$$\left. \begin{aligned} \frac{\xi}{t} &= \frac{3}{2} V(t) - \sqrt{g\delta h_0} \quad , \\ \dot{\xi} &= \frac{3}{2} V - \sqrt{g\delta h_0} + \frac{3}{2} \dot{V}t \\ h_1(t) &= h_0 \left(1 - \frac{V}{2\sqrt{g\delta h_0}} \right)^2 \end{aligned} \right\} \quad (23)$$

After substituting (23) into (22) and integrating, one obtains the total mass in the dissipative region:

$$M(t) = h_0 \sqrt{g\delta h_0} \left(1 - \frac{V(t)}{2\sqrt{g\delta h_0}} \right)^3 t \quad . \quad (24)$$

The momentum flux across $y = \xi(t)$ being $\rho V h_1 (V - \dot{\xi})$, the rate of change of momentum in this region is given by

$$\frac{dP}{dt} = \rho V h_1 (V - \dot{\xi}) + \text{forces} \quad . \quad (25)$$

a) Since we are neglecting the dynamics of the warm air mass, the net horizontal pressure gradient acting on this region is

$$\left[g \frac{\rho h_1^2}{2} - g \frac{\rho (1-\delta) h_1^2}{2} \right] \quad .$$

(The caveats noted above about the hydrostatic pressure approximation apply here as well.)

b) The drag force along the ground is

$$\rho K \int_{\xi}^a v^2 dy = \rho K V^2 (a - \xi) \quad .$$

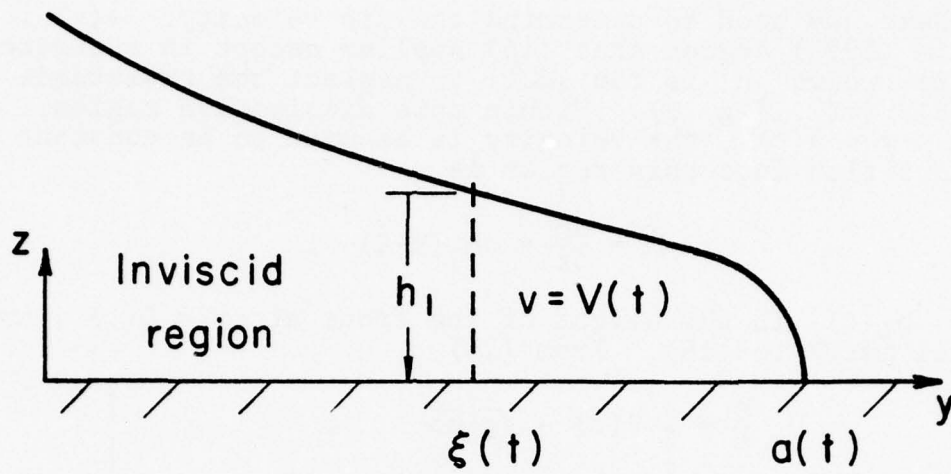


Figure 3. Coordinate system for the local analysis of the surface front.

c) We have

$$\frac{dP}{dt} = \frac{d}{dt} (MV) = V\dot{M} + M\dot{V}$$

d) At the tip, $V = \dot{a}$, and this must apply throughout this region. Substituting all of these into (25) and rearranging yields

$$\begin{aligned} \left(1 - \frac{\dot{a}}{2\sqrt{g\delta h_0}}\right)^3 t \frac{\ddot{a}}{\sqrt{g\delta h_0}} &= \frac{1}{2} \left(1 - \frac{\dot{a}}{2\sqrt{g\delta h_0}}\right)^4 \\ &- \frac{K\sqrt{g\delta h_0}}{h_0} \left(\frac{\dot{a}}{\sqrt{g\delta h_0}}\right)^2 \left[\frac{a}{\sqrt{g\delta h_0}} - t \left(\frac{3}{2} \frac{\dot{a}}{\sqrt{g\delta h_0}} - 1 \right) \right] \end{aligned} \quad (26)$$

We note that the inviscid solution,

$$a(t) = 2\sqrt{g\delta h_0} t$$

satisfies (26) if $K = 0$. For $K \neq 0$, it determines how the motion of the surface front is modified by shear stress at the ground. The equation may be put in dimensionless form by defining a dimensionless time,

$$\tau = \frac{\sqrt{g\delta h_0} K}{h_0} t, \quad (27)$$

and a dimensionless lag of the tip behind its inviscid position,

$$\alpha = \frac{(2\sqrt{g\delta h_0} t - a)K}{h_0}. \quad (28)$$

Then (26) becomes

$$4(\dot{\alpha})^3 \tau \ddot{\alpha} + \dot{\alpha}^4 = 16(2 - \dot{\alpha})^2 (3\dot{\alpha}\tau - 2\alpha), \quad (29)$$

and the position of the tip is given by

$$a = 2\sqrt{g\delta h_0} t - \frac{h_0}{K} \alpha(\tau). \quad (30)$$

We are primarily interested in the solution of (29) for relatively short times (on the τ -scale). Whitham (1955) showed that

$$\alpha(\tau) = 2.58916 \tau^{4/3} \left[1 + 0.81917 \tau^{1/3} + o(\tau^{2/3}) \right]. \quad (31)$$

In terms of our original variables, the position and velocity of the surface front are given by

$$a(t) = 2\sqrt{g\delta h_0} t - 2.5816 (g\delta h_0)^{2/3} \left(\frac{K}{h_0}\right)^{1/3} t^{3/4} * \\ \left[1 + 0.81917 \left(\sqrt{\frac{g\delta}{h_0}} K t\right)^{1/3} + \dots \right] \quad (32)$$

$$\dot{a}(t) = 2\sqrt{g\delta h_0} \left[1 - 1.72611 \left(\sqrt{\frac{g\delta}{h_0}} K t\right)^{1/3} \right. \\ \left. - 1.76747 \left(\sqrt{\frac{g\delta}{h_0}} K t\right)^{2/3} + \dots \right] \quad (33)$$

while the position of the rear of the dissipative region is given by

$$\xi(t) = \sqrt{g\delta h_0} t \left[2 - 5.1783 \left(\sqrt{\frac{g\delta}{h_0}} K t\right)^{1/3} \right. \\ \left. - 5.3024 \left(\sqrt{\frac{g\delta}{h_0}} K t\right)^{2/3} + \dots \right] \quad (34)$$

These trajectories are plotted in Fig. 4 for a set of typical parameter values.

This completes the development of this (simplest) model. Next, we consider some of its consequences. First, we note that, according to this simple theory, the motion of a cold front moving under a stationary warm air mass in the absence of Coriolis forces is essentially unsteady. As shown in Fig. 4, the surface front continually decelerates from its initial velocity. Whitham (1955) noted that

$$a \sim t^{1/2}, \quad \dot{a} \sim t^{-1/2} \quad \text{as } t \rightarrow \infty \quad (35)$$

so that the front neither comes to rest nor attains a steady velocity. Apparently the dynamic effects of the warm air mass (including Coriolis effects) are required to obtain a stationary front (or a warm front), as we show below.

Second, let us consider the effects of Coriolis forces, which we have neglected to this point. If we still retain $\partial/\partial x = 0$, which is legitimate near the center of a cold or warm front, (18) should be replaced by

$$\left. \begin{aligned} \frac{\partial h}{\partial t} + \frac{\partial}{\partial y} (vh) &= 0, \\ \frac{\partial v}{\partial t} + v \frac{\partial v}{\partial y} + g\delta \frac{\partial h}{\partial y} + \frac{Kv^2}{h} &= -fu, \end{aligned} \right\} \quad (36)$$

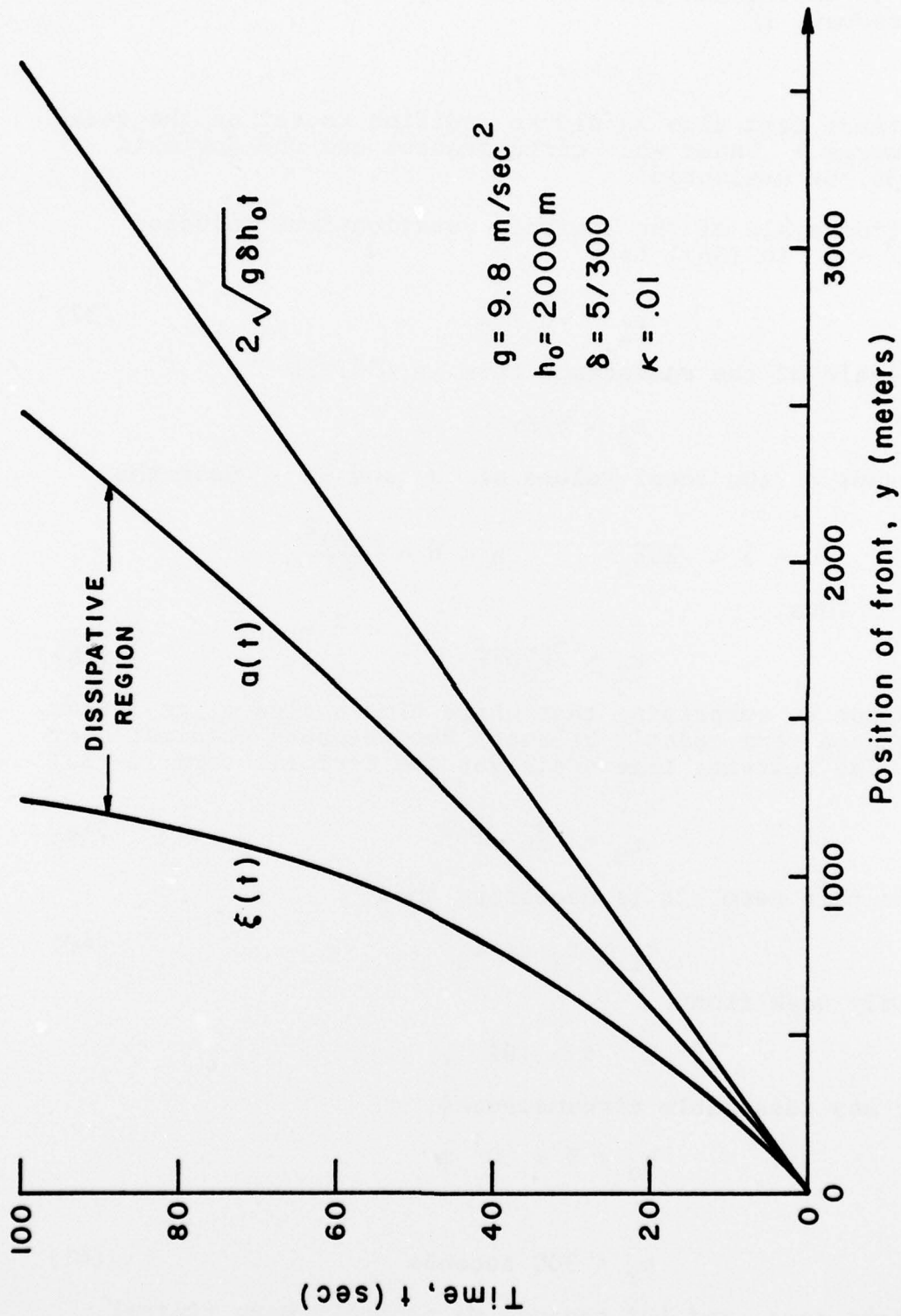


Figure 4. Trajectories of surface front without dissipation ($2\sqrt{g\delta h_0 t}$), surface front with dissipation ($a(t)$), and rear of dissipative region ($\xi(t)$). The front is a cold front in the absence of Coriolis effects.

where u is the velocity component parallel to the front. (There is an additional equation for $\partial u / \partial t$, which we omit here. Moreover, if

$$u \gg v ,$$

the resistance term also should be modified to act on the total kinetic energy.) Under what circumstances can the Coriolis term in (36) be neglected?

The time-scale of the inviscid rotation-free solution ($K = 0$, $f = 0$ in (36)) is

$$t_1 \sim \sqrt{h_0 / g\delta} \quad (37)$$

The time-scale of the resistance term in (36) is

$$t_2 \sim h / Kv ,$$

which depends on the local values of v and h . Near the tip,

$$v = \dot{a} \sim \sqrt{g\delta h_0} , \quad h \sim \bar{h} = \frac{K(\dot{a})^2}{g\delta} ,$$

from (21). Thus,

$$t_2 \sim \sqrt{h_0 / g\delta} \quad (38)$$

It should not be surprising that these time-scales align, since the resistance term exactly balances the pressure gradient near the tip. The relevant time-scale for the Coriolis term in (36) is

$$t_3 \sim |fu/v|^{-1} \quad (39)$$

To neglect this term, it is necessary that

$$t_1 \sim t_2 \ll t_3 . \quad (40)$$

For a fairly weak front,

$$\delta \sim .01 ,$$

and under any reasonable circumstances,

$$h_0 < 9 \times 10^3 \text{ m} .$$

Thus,

$$t_2 < 300 \text{ seconds} \quad (41)$$

in the worst case, and 100 seconds is probably more typical. Taking

$$1/f \sim 10^4 \text{ seconds} ,$$

we see that (40) requires that

$$|u/v| \ll 30 . \quad (42)$$

The numerical results of Kasahara, et al. certainly satisfy (42), and it appears that (42) may be satisfied by many cold fronts.

These estimates should not be interpreted to mean that the current model can be applied directly to cold fronts generated by Coriolis forces. Rather, they suggest that the dynamics predicted by this model near the tip typically occur much faster than the time-scale on which Coriolis forces act. Thus, the behavior near the tip should be relatively insensitive to Coriolis effects, provided hydrostatic forces dominate Coriolis forces away from the tip.

B. Stationary Fronts

We noted above that our simplest model (without Coriolis forces) produced only cold fronts, in which the cold air continually advanced beneath the warm air. Moreover, the surface front was always blunt-nosed, as shown in Fig. 5. If Coriolis forces are included, warm fronts, cold fronts and stationary fronts are all possible, as demonstrated by Kasahara, et al. (1965). In this section, we analyze the structure at the surface of a stationary front, for comparison with that in a cold front. We will see that the blunt-nosed shape that occurred above cannot occur in a stationary front, but that the surface front may either be needle-nosed or have a finite slope.

If we include Coriolis forces (with a β -plane approximation), Eqs. (10) become

$$\frac{\partial v}{\partial t} + u \frac{\partial v}{\partial x} + v \frac{\partial v}{\partial y} + g(1-\delta) \frac{\partial H}{\partial y} + g\delta \frac{\partial h}{\partial y} + fu = 0 ,$$

$$\frac{\partial u}{\partial t} + u \frac{\partial u}{\partial x} + v \frac{\partial u}{\partial y} + g(1-\delta) \frac{\partial H}{\partial x} + g\delta \frac{\partial h}{\partial x} - fv = 0 ,$$

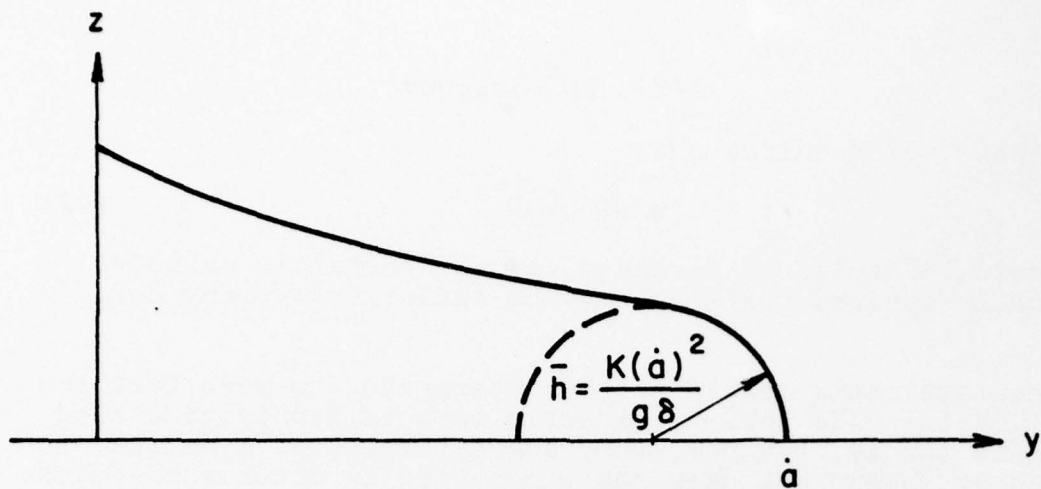
$$\frac{\partial h}{\partial t} + \frac{\partial}{\partial x} (uh) + \frac{\partial}{\partial y} (vh) = 0 ,$$

(43)

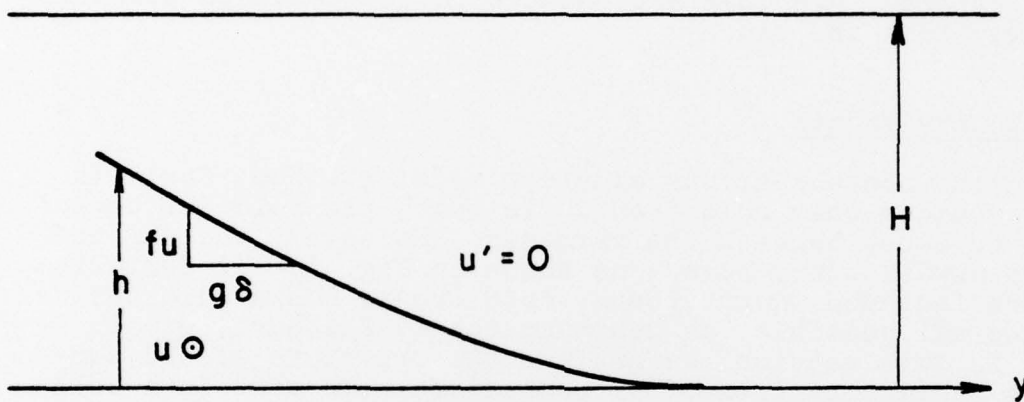
$$\frac{\partial v'}{\partial t} + u' \frac{\partial v'}{\partial x} + v' \frac{\partial v'}{\partial y} + g \frac{\partial H}{\partial y} + fu' = 0 ,$$

$$\frac{\partial u'}{\partial t} + u' \frac{\partial u'}{\partial x} + v' \frac{\partial u'}{\partial y} + g \frac{\partial H}{\partial x} - fv' = 0 ,$$

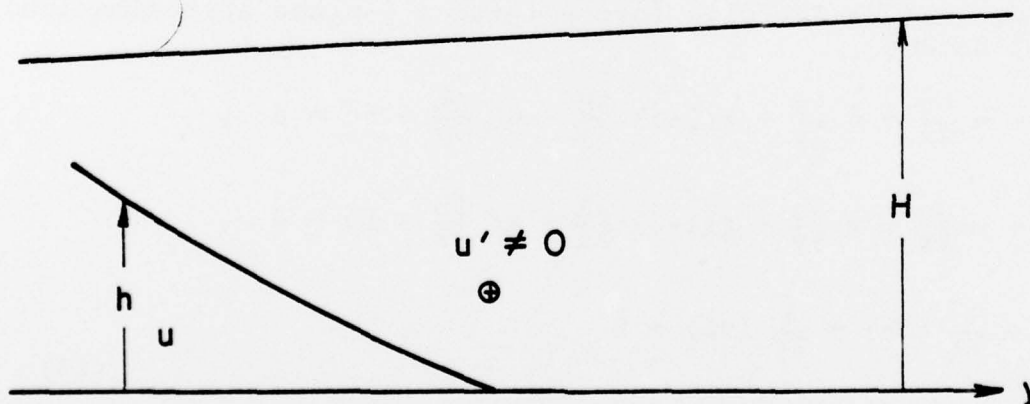
$$\frac{\partial}{\partial t} (H-h) + \frac{\partial}{\partial x} (u' (H-h)) + \frac{\partial}{\partial y} (v' (H-h)) = 0$$



(a) Moving cold front without Coriolis forces



(b) Stationary front with Coriolis forces. Warm air at rest



(c) Stationary front with Coriolis forces. Warm air in motion

Figure 5. Possible shapes of surface fronts.

where $f = 2 \omega \sin \phi$ is the (constant) Coriolis parameter. These equations have an exact solution:

$$\begin{aligned}
 v &= v' = 0 \quad , \\
 u' &= \text{const.} \quad , \\
 u &= \text{const.} \quad , \\
 \frac{\partial H}{\partial y} &= - \frac{fu'}{g} \quad , \\
 \frac{\partial h}{\partial y} &= - \frac{f}{g\delta} [u - (1-\delta)u'] \quad ,
 \end{aligned}
 \tag{44}$$

If x is in the east-west direction, this solution represents a stationary polar front. [It is known to be unstable to cyclonic perturbations, which grow on a time-scale of hours. However, our primary interest is with the structure of the surface front; we have seen that the relevant time-scale there is on the order of a few minutes. Therefore, we may ignore phenomena that take much longer to occur.]

The solution, (44), is subject to the same criticism that applied to (16): near the surface front, where $h \rightarrow 0$, the stress at the ground must affect the dynamics significantly. Thus, the first two equations should be replaced by

$$\begin{aligned}
 \frac{\partial v}{\partial t} + u \frac{\partial v}{\partial x} + v \frac{\partial v}{\partial y} + g(1-\delta) \frac{\partial H}{\partial y} + g\delta \frac{\partial h}{\partial y} + fu &= \frac{\tau_{yz,i}}{h} - \frac{\tau_{yz,g}}{h} \\
 \frac{\partial u}{\partial t} + u \frac{\partial u}{\partial x} + v \frac{\partial u}{\partial y} + g(1-\delta) \frac{\partial H}{\partial x} + g\delta \frac{\partial h}{\partial x} - fv &= \frac{\tau_{xz,i}}{h} - \frac{\tau_{xz,g}}{h}
 \end{aligned}
 \tag{45}$$

Our objective here is to find a suitable modification of (44) which approximately satisfies (45), even as $h \rightarrow 0$.

An immediate generalization of (44) is obtained by letting (u, u') depend on y . Thus, there is a family of solutions of (43), defined by

$$\begin{aligned}
 v &= v' = 0 \quad , \\
 u' &= u'(y) \quad , \\
 u &= u(y) \quad , \\
 \frac{\partial H}{\partial y} &= - \frac{fu'}{g} \quad , \\
 \frac{\partial h}{\partial y} &= - \frac{f}{g\delta} [u - (1-\delta)u'] \quad .
 \end{aligned}
 \tag{46}$$

The previous solution, (44), is a member of this family. We want to choose $u(y)$ and $u'(y)$ so that (46) remains a valid approximate solution of (45), even as $h \rightarrow 0$.

Because $v' = v \equiv 0$ in (46), we must have

$$\tau_{yz} = 0 \quad (47)$$

For consistency with (17), we define

$$\tau_{xz,g} = K_g |u|u, \quad \tau_{xz,i} = -K_i |u+u'| (u-u') \quad (48)$$

Ordinarily, $K_g > K_i$.

We consider first the case in which the warm fluid is at rest:

$$u'(y) = 0, \quad \frac{\partial H}{\partial y} = 0 \quad (49)$$

In order for the stress terms on the right side of (45b) to remain bounded as h vanishes, we require that as $h \rightarrow 0$,

$$u \sim \alpha h^p, \quad p \geq 1/2 \quad (50)$$

Substituting this into (46) yields

$$\frac{dh}{dy} \sim -\frac{f\alpha}{g\delta} h^p$$

We obtain a valid solution only if

$$1/2 \leq p < 1$$

$$h \sim C(y-y_0)^{\frac{1}{1-p}}, \quad H = \text{const.}, \quad (51)$$

$$u \sim D(y-y_0)^{\frac{p}{1-p}}, \quad u' = 0$$

In this case, the slope of the surface front is balanced by the (vanishing) velocity difference across the front.

To this order of approximation, the exponent p is restricted only to a finite range. For any p in this range, however, the surface front has an elongated "needle-nose," as shown in Fig. 5. This shape contrasts sharply with the blunt-nosed shape obtained above when Coriolis forces were neglected (also shown in Fig. 5).

Next, suppose that, in the vicinity (in y) of the surface front,

$$u'(y) \sim \bar{u}' \neq 0 \quad (52)$$

Now the stress terms in (45b) are bounded only if

$$u \sim \bar{u}' \left(\frac{K_i}{K_i + K_g} \right)^{1/2} \quad \text{as } h \rightarrow 0. \quad (53)$$

Here the local solution is

$$\frac{\partial H}{\partial y} = - \frac{f}{g} \bar{u}', \quad \frac{\partial h}{\partial y} = \frac{f}{g\delta} = \frac{f}{g\delta} \left[(1-\delta) - \left(\frac{K_i}{K_i + K_g} \right)^{1/2} \right] \bar{u}' \quad (54)$$

This configuration is shown in Fig. 5, as well. Again, the slope of the surface front is balanced by the velocity difference across the jump. In this case, the velocity difference does not vanish near the surface front, and the slope of the front remains finite. The slope away from the surface front can be either larger or smaller than that given by (54), depending on the local velocity difference. For sufficiently small δ , the slope of the surface front is opposed to and much larger than the slope of the tropopause above it. This feature seems to be frequently observed in atmospheric fronts.

We may summarize our results about the possible shapes of surface fronts as follows:

(a) Fronts accompanying events whose duration is significantly less than an hour or so can be analyzed without considering Coriolis effects. These fronts are always cold fronts. The shape of the surface front is blunt-nosed, as determined by a balance between the hydrostatic pressure gradient and the resistance of the ground to the motion of the front itself.

(b) For events which last for several hours, Coriolis forces can play an important role. Warm fronts, cold fronts and stationary fronts are all possible.

(c) The slope of a stationary front at the surface is balanced by the local velocity difference across the front, subject to the constraint that there be no unbalanced shear stress from motion parallel to the front. The slope of the front at the surface is proportional to the vertically-averaged velocity in the warm air. This is also true at the tropopause. If the velocity parallel to the front in the warm air does not vanish, the slope of the surface front is opposed to and usually larger than that of the tropopause above it. If it does vanish, so that the warm air is at rest, the slope of the surface front vanishes, yielding a needle-nosed shape. The surface front cannot be blunt-nosed, because there is no shear stress normal to the front.

C. Comparison with Observations

In light of the preliminary and somewhat restricted nature of these results, an exhaustive comparison of the predictions of these models with the observed behavior of surface fronts is thought to be premature at this time. Nevertheless, it may be worthwhile to show that some of the qualitative features predicted by these models are observed, even when our somewhat restrictive assumptions (either no Coriolis forces or stationary fronts) are not satisfied. This qualitative agreement, in circumstances beyond the range of the present model, suggests that the models can be generalized to a wider class of problems without affecting the qualitative features discussed above.

Figure 6 shows three vertical cross-sections of the atmosphere over the United States, taken from an analysis of Hurricane Hazel by Palmén (1958). These figures each were taken at a fixed latitude (either 40°N or 45°N), with east to the right of the figure. The vertical scale is given on the figure but the horizontal scale is not; consequently it is difficult to measure frontal slopes for any quantitative comparisons. As noted in the captions, the heavy solid lines denote fronts or tropopause, and these are our main concern. In Figs. 6a and 6b, the cold air mass is in the center of the figure, with warm air on either side; in Fig. 6c, the cold air is to the left. Temperature differences across the front were on the order of $5^{\circ}\text{C} - 10^{\circ}\text{C}$ ($\delta \sim .02 - .03$). Five surface fronts are seen in these figures; each is moving to the east (as inferred from the wind indicators). Thus, none of the fronts are actually stationary; moreover, Coriolis forces are important in determining the overall motion shown. Thus, neither of the models developed above can be expected to apply precisely. Even so, some of the qualitative features of the fronts are predicted by the models, as we now show.

Because the fronts are all moving eastward (i.e., to the right), the fronts to the right in Figs. 6a and 6b are cold fronts, while those to the left are warm fronts. The front in Fig. 6c is a cold front. It is easily seen that the cold front in Fig. 6a is blunt-nosed, and that neither of the warm fronts in Figs. 6a and b are. (In the figures, all of the cold fronts are drawn blunt-nosed very close to the ground. However, the data is available only along the vertical lines shown, and it is not clear that the shapes of the cold fronts at the ground, as shown in Figs. 6b and 6c, actually were observed.) In our model, this shape is a consequence of the shear stress at the ground, which slows the motion of the cold front. The cold front in Fig. 6b is almost stationary so that this shear stress is relatively small, and its blunt nose should be expected to be small as well. Similarly, the speed of the cold front in Fig. 6a is larger, and its blunt nose ought to be larger as well. Thus, there is some evidence that the observed shapes of the cold fronts at the surface (blunt-nosed) are

C-21

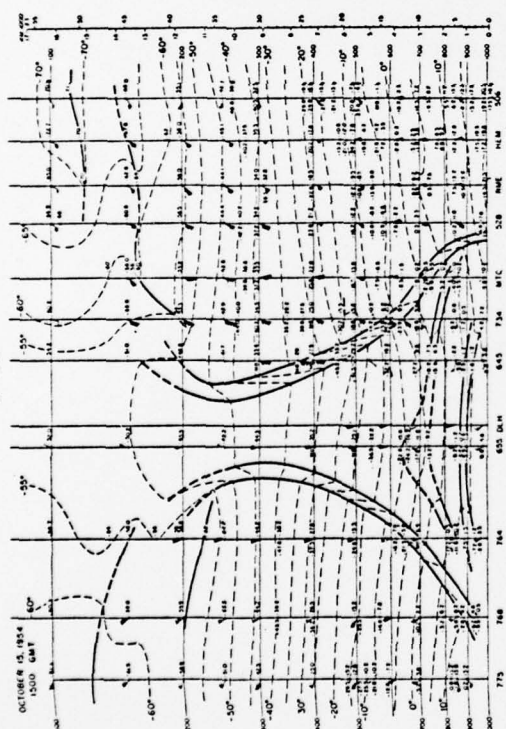


Fig. 16. Vertical cross-section, October 15, 1500 GCT, approximately 45°N. Thin dashed lines are isotherms, and heavy lines frontal boundaries or tropopause. Temperature, dewpoint and wind are indicated at standard levels and significant points.

6a

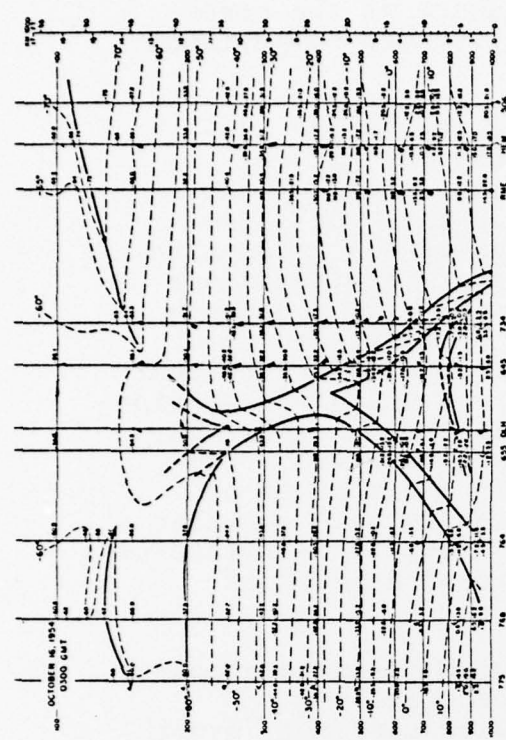


Fig. 17. Vertical cross-section, October 16, 0900 GCT, approximately 45°N. Symbols as in Fig. 16.

6b

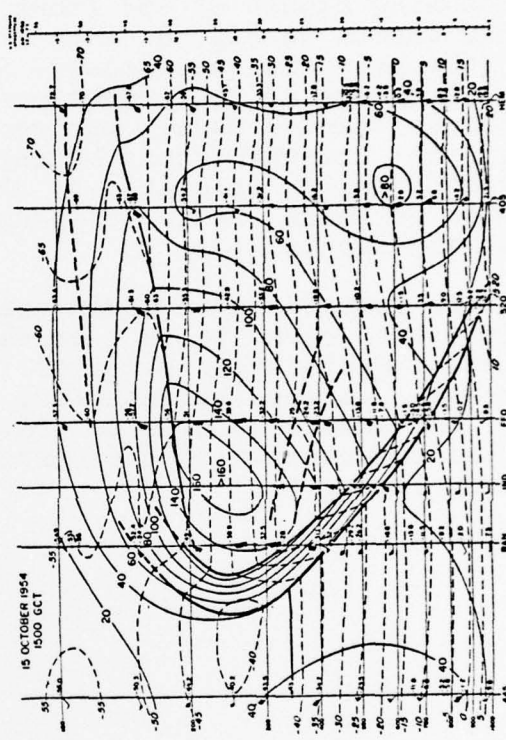


Fig. 19. Vertical cross-section, October 15, 1500 GCT, approximately 40°N. Thin dashed lines are isotherms, and heavy lines frontal boundaries or tropopause. The thin solid lines mark isobars at intervals of 20 kt of observed wind, without regard to direction.

6c

Figure 6. Observed vertical cross-sections of atmosphere (from Palmén, 1958).

consistent with the model, as is the dependence of the nose size with front speed. No attempt at quantitative comparisons is made here.

The model predicts that the slope of a stationary surface front, the slope of the tropopause above it, and the vertically-averaged velocity (parallel to the front) of the warm air between are all related. In particular, the slope of the surface front is opposed to the slope of the tropopause, and typically larger than it. If the slope of the tropopause vanishes, the slope of the (stationary) surface front beneath it also vanishes, giving the surface front an elongated nose. The opposing slopes of the front and the tropopause are evident for the fronts in Fig. 6, even though the fronts are not stationary; (the point is questionable for the cold front in Fig. 6a, where the slope of the tropopause is changing rapidly). The tropopause becomes nearly horizontal west of the warm front in Fig. 6b; the warm front beneath it is seen to have a rather elongated tip, as predicted by the model. Thus, the qualitative behavior of these fronts is in agreement with the model of stationary fronts.

This comparison of model predictions with observed atmospheric fronts seems to be favorable, at least in terms of predicting qualitative behavior. Certainly it does not "prove" the model. It does suggest that the model has some predictive power, and should be able to provide some guidance to the detailed computation of the structure of fronts in the planetary boundary layer.

REFERENCES

- Dressler, R.F. 1952. "Hydraulic resistance effect upon the dam-break functions," J. Res. Nat. Bureau of Standards. 49, 217-225.
- Kasahara, A., Isaacson, E., and Stoker, J.J. 1965. "Numerical studies of frontal motion in the atmosphere - I," Tellus. 17, 261-276.
- Palmén, E. (1958) "Vertical circulation and release of kinetic energy during the development of Hurrican Hazel into an extra-tropical storm," Tellus. 10, 1-23.
- Ritter, A. (1892) "Die Fortpflanzung der Wasserwellen," Z. Ver. deut. Ing. 36.
- Teske, M.E., and Lewellen, W.S. 1977. "Turbulent transport model of a thunderstorm gust front," 10th Conf. on Severe Local Storms, Oct. 18-21, 1977, Omaha, Neb.
- Whitham, G.B. 1955. "The effects of hydraulic resistance in the dam-break problem," Proc. Roy. Soc. A 227, 399-407.
- Yih, C.S., and Guha, C.R. 1955. "Hydraulic jump in a fluid system of two layers," Tellus. 7, 358.

REPORT DOCUMENTATION PAGE		READ INSTRUCTIONS BEFORE COMPLETING FORM
1. REPORT NUMBER 6	2. GOVT ACCESSION NO.	3. RECIPIENT'S CATALOG NUMBER 9
4. TITLE (and Subtitle) 1977 STATUS REPORT ON LOW-LEVEL, ATMOSPHERIC TURBULENCE MODEL FOR MARINE ENVIRONMENTS		5. TYPE OF REPORT & PERIOD COVERED Final <i>7 rept.</i> 15 Nov 1976 - 15 Nov 1977
7. AUTHOR(s) 10 W.S. Lewellen, D.A. Oliver, M.E. Teske, H. Segur and O. Cote		6. PERFORMING ORG. REPORT NUMBER A.R.A.P. Report No. 320
9. PERFORMING ORGANIZATION NAME AND ADDRESS Aeronautical Research Associates of Princeton, Inc. 50 Washington Road, P.O. Box 2229 Princeton, NJ 08540		8. CONTRACT OR GRANT NUMBER(s) 15 N00019-77-C-0131 <i>new</i>
11. CONTROLLING OFFICE NAME AND ADDRESS Department of the Navy Naval Air Systems Command Washington, DC 20361		10. PROGRAM ELEMENT, PROJECT, TASK AREA & WORK UNIT NUMBERS
12. REPORT DATE 11 November 1977		13. NUMBER OF PAGES
14. MONITORING AGENCY NAME & ADDRESS (if different from Controlling Office) 14 ARAP-320 12 160p.		15. SECURITY CLASS. (of this report) UNCLASSIFIED
16. DISTRIBUTION STATEMENT (of this Report) Prepared for public release; distribution unlimited. APPROVED FOR PUBLIC RELEASE: DISTRIBUTION UNLIMITED		
17. DISTRIBUTION STATEMENT (of the abstract entered in Block 20, if different from Report)		
18. SUPPLEMENTARY NOTES		
19. KEY WORDS (Continue on reverse side if necessary and identify by block number) marine atmospheric boundary layer turbulent aerosol transport fog dynamics terrain influence on boundary layer low-level cloudiness flow radiation interaction with turbulence boundary-layer structure of sharp gust front dynamics weather fronts		
20. ABSTRACT (Continue on reverse side if necessary and identify by block number) —> This report details the last year's developments to A.R.A.P.'s program for computing the detailed low-level atmospheric distributions of velocity, temperature, moisture, refractive index, and the turbulent variances of these quantities for marine environments. Effort has been divided between extending the model, and in exercising the existing model to both exemplify expected phenomena and to compare with available observations. The model has been extended: to remove the hydrostatic approximation; to incorporate condensation and radiation into the two-dimensional, unsteady model; to incorporate terrain variation into the		

surface boundary conditions; and to determine the influence of particle size on the turbulent transport of aerosols. Sample calculations include fog episodes, diurnal variation of stratus over the ocean, the general structure of the trade-wind boundary layer, and an evaporatively cooled gust front. Although verification tests have not been adequate to provide a detailed assessment of accuracy, the model results are generally quite consistent with available observations. ←

APPROVED FOR PUBLIC RELEASE
DISTRIBUTION UNLIMITED